Modeling morphogenesis on epithelial tissues : from forces to geometry and back

Diego Contreras

PSL UNIVERSITÉ PARIS

THÈSE DE DOCTORAT
DE L'UNIVERSITÉ PSL

Préparée à École Normale Supérieure

Modeling morphogenesis on epithelial tissues: From forces to geometry and back

Soutenue par
Diego CONTRERAS
Le 16 Decembre 2019

École doctorale n°564
Physique de Île-de-France

Spécialité
Physique

Composition du jury :

Sylvie HÉNON Université Paris Diderot	*Présidente*
Alice NICOLAS Laboratoire des Technologies de la Microelectronique	*Rapporteuse*
Romain LEVAYER Institut Pasteur	*Rapporteur*
François PAYRE Université Paul Sabatier Toulouse III	*Examinateur*
Vincent HAKIM École Normale Supérieure	*Directeur de thèse*
Francis CORSON École Normale Supérieure	*Co-directeur*

ENS | PSL

ABSTRACT

Epithelial tissues are ubiquitous in animal life, covering surfaces and separating body compartments in diverse organs and species. Epithelium is the first tissue to form, playing a key role in structuring the intricate steps of an organism's development. In such a complex system, the interplay between cell division, chemical signaling, and mechanical forces permits the emergence of different tissues with specific functions.

To uncover the mechanisms at play in epithelial tissue mechanics, a useful tool is provided by vertex models, in which cells are idealized as juxtaposed polygons. Numerical simulations of cell division in vertex models yield geometrically irregular cells, similar to empirical observations in epithelia, even when cell mechanical properties are homogeneous. Nevertheless, existing theoretical analyses are mostly confined to the mechanics of regular hexagonal lattices.

Here, we develop an analytical description of geometrically disordered vertex models. We first quantify, in numerical simulations, geometric and mechanical cell properties in the presence of diverse sources of disorder, including various division rules or relaxation in the presence of noise. We then develop a simple mean-field description able to account for these properties. This description is expanded to address the interaction of isolated and clustered cells with mechanical properties differing from the surrounding tissue relevant in a wide range of biological contexts. This allows us to bridge the gap between theory and experiments, quantitatively predicting how variation in forces may affect geometry and topology as well as fitting mechanistic model parameters to the observed geometry of cell membranes in a tissue.

Finally, in a collaborative work with the Payre's lab (U. de Toulouse), we apply our analysis to account for the statistics of cell geometry and division dynamics in experiments performed on epidermis differentiation in the fly. We particularly focus on characterizing the mechanical properties of clustered clonal cells with distinct proliferation rates from their environment.

RESUMÉ

Les tissus épithéliaux sont ubiquitaires dans les organismes vivants, couvrant des surfaces et séparant différents compartiments dans divers organes et espèces. L'épithélium est le premier tissu qui apparaît au cours du développement et il joue un rôle central pour en structurer les étapes. Dans ce processus complexe, les interactions entre les divisions cellulaires, la signalisation chimique et les forces mécaniques permettent l'émergence de différents tissus avec des fonctions diverses.

Dans l'élucidation des mécanismes en jeu dans la mécanique des tissusépithéliaux, un outil utile est constitué par les modèles de vertex, dans lesquels les cellules sont représentées de façon simplifiée par des polygones. La simulation de la division cellulaire dans ces modèles, produit des tissus avec des cellules géométriquement irrégulières, semblablesà celles observées dans lesépithéliums naturels, même quand les propriétés mécaniques des différentes cellules sont identiques. Les analyses théoriques existantes sont cependant, pour la plupart, confinées aux réseaux réguliers hexagonaux.

Dans ce travail, nous proposons une analyse théorique d'un modèle de vertex géométriquement désordonné. Nous commençons par quantifier à l'aide de simulations numériques, les propriétés géométriques et mécaniques des cellules, dans des tissus désordonnés produits par différentes règles de division cellulaires ou simplement par la relaxation en présence de bruit. Nous développons ensuite une analyse simple de type "champ moyen" pour décrire ces propriétés. Cette description est étendue au cas d'une cellule ou d'un clone de cellules interagissant avec le tissu environnant aux propriétés mécaniques différentes, une situation qui se retrouve dans différents contextes biologiques. Cela nous permet de jeter un pont entre la théorie et l'expérience et de prédire quantitativement comment cette variation mécanique affecte la géométrie et la topologie et d'ajuster un modèle mécanique aux observations empiriques de la géométrie des membranes cellulaires dans un tissu.

Finalement, en collaboration avec le groupe de F. Payre (Université de Toulouse), nous appliquons cette analyse pour décrire la géométrie et la dynamique des divisions cellulaire au cours de la différenciation de l'epiderme de la mouche. Nous nous attachons particulièrement à caractériser les propriétés mécaniques d'un clone de cellules qui prolifère différemment du tissu environnant.

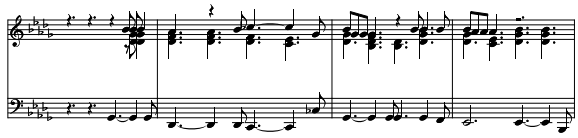

Part I

INTRODUCTION

1

MODELLING COMPLEX AND BIOLOGICAL SYSTEMS

La biologie occupe parmi les sciences une place à la fois marginale et centrale. Marginale en ce que le monde vivant ne constitue qu'une infime et très "spéciale" partie de l'univers connu, de sorte que l'étude des êtres vivants ne semble pas devoir jamais révéler des lois générales, applicables hors de la biosphère. Mais si l'ambition ultime de la science entière est bien, comme je le crois, d'élucider la relation de l'homme à l'univers, alors il faut reconnaître à la biologie une place centrale puisqu'elle est, de toutes les disciplines, celle qui tente d'aller le plus directement au coeur des problèmes qu'il faut avoir résolus avant de pouvoir seulement poser celui de la "nature humaine" en termes de métaphysique.

Le hasard et la nécessité, 1970.

Jacques Monod .

As our understanding of biological system develops, so does our fascination for the wealth of subtle mechanisms underlying life. Indeed, biological systems are more than the sum of their parts: while no particular part is sufficient in isolation, unveiling complex interactions between parts is the key to understanding how life emerges.

In the past, physicists once were reckless enough to affirm *"[...] the future truths of physical science are to be looked for in the sixth place of decimals"*(Albert A. Michelson, 1896), even though Michelson himself was to shed light upon one of the two Kelvin's "clouds". A century has passed, and that perspective has long fallen apart. On the contrary, fundamental physics is far from being complete. Complex system encourage physicists to research more sophisticated tools to understand emergent properties. As the power of the mathematical laws to explain the nature around us was once overestimated, it is worth to ask again what the limits of current models are.

Models are limited by their assumptions: a usual strategy in physics would be to assume the simplest model. Indeed, *spherical cows* have successfully explained a wide variety of phenomena in physics. As well, diverse biological systems have been successfully explained by simple models [Doyle, 2001]. Notorious examples range from the Vicsek model to describe flocks of birds, as a group of simple random particles with a tendency to follow their neighbors [Vicsek et al., 1995,Giardina, 2008]; to the Kuramoto model to describe large-scale neural networks and cognitive function [Breakspear et al., 2010].

In the context of developmental biology, a beautiful example of how simple physical models can provide insight into the mechanisms and processes underlying animal development is provided by the Turing patterns [Turing, 1990].Turing equation can explain pattern formation in seashells [Meinhardt, 2009], coat patterns in mammals like zebras [Bard, 1981], and even the formation of our very own fingers [Raspopovic et al., 2014], among other patterns [Schweisguth and Corson, 2019].

However, a simple Turing pattern cannot scale with the variable size found in different individuals of the same species, as it is associated with characteristic determined length at

the molecular level [Gregor et al., 2007]. Nevertheless, Nature had time to explore a wider variety of ways. For instance, the patterning in drosophila—and other insects—embryos, where the gradient of diverse transcription factors signals the relative position to each cell, and defines its fate with an astonishing precision of 1% at the level of individual cells [Tkačik et al., 2015,Petkova et al., 2019]. It is not easy task to find general mechanisms, which makes modeling complex biological systems with reductionist mathematical models an adventure in muddy waters, but multiple success stories prove it is a path that can expand our understanding of such complex systems.

1.1 PHYSICS OF MODELING EPITHELIAL TISSUES

In the case of the epithelium, things do not get easier. As one of the four basic animal tissues, the study of epithelium is crucial to understanding animal development. Formed by one or more layers of cells, it is the first tissue to form during development. Among other functions, epithelia cover the free surfaces of an organism, constitute the inner covering of the cavities, hollow organs, ducts of the body as well as form mucous membranes and the inside of glands, protecting from mechanical damage, the entry of micro-organism. They physically separate body compartments, allowing the coexistence of distinct biochemical and mechanical micro-environments, controlling, such as water evaporation in the skin epidermis. They also liberate substances in glands, or absorb them in the guts.

The epithelium is the playground where mechanical forces and chemical signals enact the tissue towards specific functions and behavior. While one should not loose sight of genetic and chemical processes occurring in parallel, mechanics has been shown to account for many empirical observations in epithelia. Indeed, several models have captured the mechanical ingredients that give rise to the morphology and dynamics observed in epithelial cells. A simple Vicsek-like model can explain the self-organized patterns that emerge in epithelial cell migration [Sepúlveda et al., 2013]. Potts models have been applied to model epithelium, where a spin-like hamiltonian determines the domain of each cell to address cell sorting problems [Graner and Glazier, 1992]. Nowadays, a popular choice to model epithelium is the vertex model, where cells are idealized as juxtaposed polygons tesselating the space, leaving no free space. Forces are a function of cell perimeter and area. The model has been intensively used to shape wound healing [Nagai and Honda, 2006,Staddon et al., 2018], applied to unveil cancer propagation and the conditions tumoral cells migrate into healthy tissue [Osborne et al., 2010,Tsuboi et al., 2018]. Some other variants of the model went further, adding complexity, such as to account for the cell tridimensionality cues that an epithelial cell use to know when has achieved its correct final size [Hufnagel et al., 2007].

This model, even in its relative simplicity, exhibits a wide range of behaviors and captures the mechanical complexity found in biological epithelial tissues *in-vivo*. If other factors are at play, the model can be generalized to integrate additional parameters. If something is observed in the model, we may have good reasons to expect to also find it in nature. In this thesis, we will explore how proliferation and cell forces, especially in

cases when different cells interact, give rise to different geometries. Alternatively, the way back: what the observed experimental data tells us about the forces that created it.

CONTENTS

Papers in preparation:

- "Geometry and mechanics of a clonal inclusion in a model epithelium with irregular cells" Contreras, D.-A., Hakim, V., and Corson, F. (2020). In preparation
- "Of the importance of temporally segregating cell proliferation and differentiation during development" Soulard, M., Pélissier-Monier, A., Contreras, D.-A., Hakim, V., Corson, F., Mangeat, T., Ronsin, B., Marques, S., and Payre, F. (2020). In preparation

2

BACKGROUND

2.1 D*drosophila* A MODEL ORGANISM

Nowadays, *Drosophila melanogaster* [1] is a model of choice in the study of animal development. A comparatively simple organism with a low maintenance cost, small, with a short life cycle (15-21 days). These advantages have made that no other animal of similar or greater complexity is better understood in their development [Wolpert et al., 2011]. Not only that, *Drosophila* development is analogous in many aspects with the development of other animals, including vertebrates and humans [Wolpert et al., 2011]. This discovery was a revolution in biology for more than a century, it was assumed that different types of animals had completely divengent genetics since they differ in their morphology, pointed to a very diverse development [Carroll, 2005]. Ernst Mayr, one of the 20th century's leading evolutionary biologists, once said: *Much that has been learned about gene physiology makes it evident that the search for homologous genes is quite futile except in very close relatives* [Mayr, 1970]. To the astonishment of most of the biologists of his time, Mayr was deeply mistaken in this matter. Improving our understanding of *Drosophila* development, very likely, will directly expand our knowledge of animal development in general.

2.2 MECHANICAL FEATURES OF EPITHELIAL TISSUES

Epithelial cells have a cytoskeleton formed by actin filaments that provide the cells with structural resistance. These cells are polarized along their apical-basal axis: In the basal side, cells directly attached to the extracellular matrix by a basal membrane that separates it from the connective tissue. In the apical side, cells are attached to each other.

Four main types of specialized cell-cell junctions are found in between epithelial cells, namely: tight junctions, gap junctions, desmosomes, and adherents junctions. Tight junctions seal the paracellular space, gap junctions allow ions and small water-soluble molecules to transit between cells. Desmosomes have proteins that link together with the basal domain of cells.

However, and for the fortune of our models, it is in the apical domain where the adherent junctions are found and which dominates several of the mechanical properties of the tissues. Here, actomyosin filaments are concentrated in the form of an inherently contractile ring in the interior of the cell membrane. It contains the protein actin, as well as molecular motors (myosin) and adherent molecules (cadherins). Cells are subjected to forces such as osmotic pressure and passive forces derived from the structure of their

1 *Drosophilidae* is a diverse family of flies, but often in the literature the *Drosophila melanogaster* is just referred as *Drosophila*.

cytoskeleton and membrane. Nevertheless, cellular force generation typically is the result of the myosin activity, responsible for actively contracting actin fibers. These forces are transmitted to neighboring cells by cadherins [Heisenberg and Bellaïche, 2013].

Mechanically, in general, animal tissue is dominantly viscoelastic, exhibiting an elastic solid-like behavior at short time scales, and fluid-like behavior at long time scales (above one second) [Hoffman et al., 2006, Lu et al., 2006, Park et al., 2005].

2.3 CELL DIVISION

Cell proliferation is essential in tissue development. The development of a multicellular organism from a single egg cell requires several cycles of cell divisions, each of them precisely regulated in time and according to the body plan of the organism [Edgar and O'Farrell, 1989, Edgar and O'Farrell, 1990]. Though some morphogenetic events occur with a basically constant number of cells, for instance, in the early stages of gastrulation [Martin et al., 2010], correct modeling of tissue involves in several cases the consideration of cell division.

2.3.1 *Hertwig's rule*

Introduced by Oscar Hertwig in 1884 while studying frog eggs [Hertwig, 1884], Hertwig's rule states that a mitotic cell divides along its long axis. It is easy to visualize that this must be true in a very elongated cell. Nevertheless, this has been tested to be a rule that is followed to a surprising extent, experimentally. Observing cell division during development in the *Drosophila* wing [Bosveld et al., 2016b], in particular, those cells compute the main axis according to the orientation of the tricellular junctions (TCJ). More precisely, one can define the TCJ bipolarity matrix as,

$$V = \sum_{i=1}^{n_v} \hat{u}_i \otimes \hat{u}_i, \tag{2.1}$$

where $\hat{u}_i$ are the unitary vectors that go from the barycentre of the cell to each vertex. Given the eigenvalues $\lambda_1 > \lambda_2$ and eigenvectors $\hat{e}_1 \perp \hat{e}_2$ of V, e_1 will be the direction of the division, and the anisotropy is defined by

$$\eta_{TCJ} = 1 - \frac{\lambda_2}{\lambda_1} \tag{2.2}$$

In the simulations performed in this work, cells divide according to an internal clock, not depending on their area or another measure, as the apical shape weakly correlates with the actual size of the cell [Aegerter-Wilmsen et al., 2010]. Details on the way the biological cycle of division is modeled can be found in section 4.1.

Nonetheless, Hertwig's rule is followed under conditions of mechanical homogeneity and anisotropy, and it has been shown how it is over-written in the presence of mechanical constrains [Mao et al., 2013], or in the presence of a tension, cable [Scarpa et al., 2018]. This effect can play a crucial role, and one example of it will be explored in chapter 7.

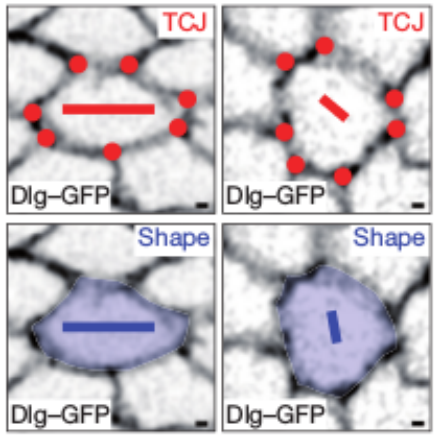

Figure 2.1: Comparison between two choices of the axis of division obtained for two cells. **Top:** using the TCJ matrix. **Bottom:** using the main axis from the second moment of area. In many cases, these two directions will be similar (as in the cells are on the left), but they differ significantly in cells with an asymmetric distribution of TCJ along their boundaries (right). Image reproduced from ref. [Bosveld et al., 2016b].

That division is not a cell-autonomous process is not surprising, since at a microscopic level, cell division in an epithelium does involve not only the mitotic cell but also its immediate neighbors. They respond to the imminent cell division with a local reduction in cadherin at the ingressing junction and self-organized actomyosin flows, leading to accumulation of myosin [Pinheiro et al., 2017].

2.4 CELLS AS POLYGONS: THE VERTEX MODEL

Introduced initially to describe foam [Weaire and Rivier, 1984], the vertex model has been widely used to describe epithelia. The tissue is represented as a planar graph of polygons tessellating the space, where each polygon represents the shape of the cell membrane. An example is shown in figure 2.2.

2.4.1 *Energy function*

To describe dynamical and equilibrium states of the network, the following energy function is introduced [Farhadifar et al., 2007],

$$E = \sum_{edges} \Lambda l_e + \sum_{cells} \frac{1}{2}\Gamma p_c^2 + \sum_{cells} \frac{1}{2} K \left(A_c - A_0\right)^2 \tag{2.3}$$

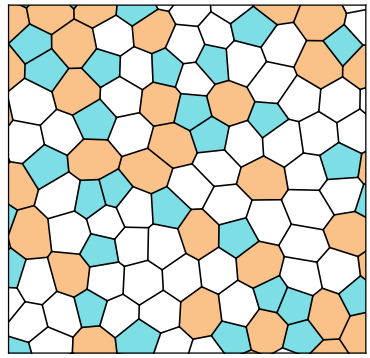

Figure 2.2: Example of a vertex model network. Six-sided cells are the most common. In the image, cells with fewer or more than 6 neighbors are filled with a cyan-orange respectively.

The sums run over the cell apical areas A_c, perimeters p_c, and individual edge length l_e. The first term describes the line tension Λ along edges, and the second term models the contractility of the apical ring with the parameter Γ, and creates a force proportional to the perimeter p_c of the cell c. The last term describes the area elasticity with the elastic coefficient K, A_0 is the preferred area of the cells. The vertex coordinates are used as dynamical variables moving following the gradient of the energy function (2.3) (details in appendix A).

As it is a phenomenological model, the parameters cannot be explicitly related to microscopic quantities. The area term is based on the presupposition that cells tend to have a preferred apical area. The main contributor to the value of Γ is expected to be the contractility of the actual actin-myosin ring. The value Λ could be decomposed in a part that increases with the actin-myosin contractility, and another part that decreases with the increase of cell-cell adhesion. Thus, it makes biological sense to have $\Gamma > 0$ and $K > 0$. The line tension Λ can have negative values if cell-cell adhesion is strong enough. In that case, it may be useful to present the energy function as,

$$E = \sum_{cells} \frac{1}{2} K(A_c - A_0)^2 + \sum_{cells} \frac{1}{2} \Gamma (p_c - p_0)^2. \tag{2.4}$$

This model differs by a constant from (2.3) and it is related to it by the change of variable $p_0 = -\Lambda/2\Gamma$, with p_0 represented by a preferred perimeter.

Eventually, the parameters of the model can vary from cell to cell, as well as from edge to edge. The case where one or a group of cells has different mechanical properties from the surrounding tissue will be an important topic in this thesis. Otherwise specified, we will use uniform values.

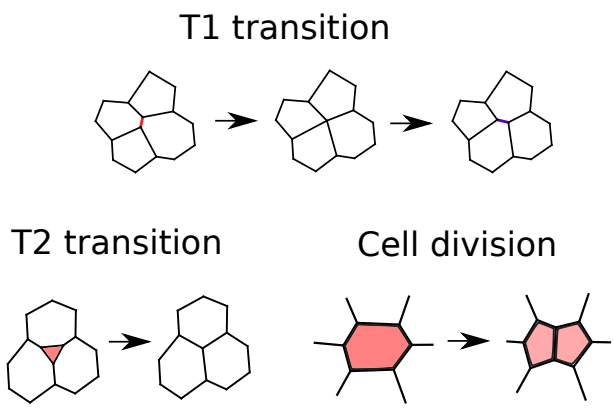

Figure 2.3: In addition to cells changing their shape under mechanical forces, cells can exchange neighbors (so called T1 transitions), undergo apoptosis (so called T2 transition), and, cells can undergo cell division modifying the topology of the network.

2.4.2 *T1 transitions*

In addition to the relaxation of the energy by the displacement of the vertices, the evolution of the tissue involves the exchange of cell neighbors, the so-called T1 transitions. Two cells in contact lose their common edge, and a new edge is formed to connect the two common neighbors, as shown in figure 2.3. Without this process, the tissue would be frozen into a solid-state, where each cell keeps its neighbors.

Experimentally, it has been shown that the occurrence of T1 events is controlled by the tumor suppressor PTEN, which prevents the lengthening of newly formed junctions, as well as cell rearrangements [Bardet et al., 2013]. This shows that T1 transitions are actively controlled in tissue.

2.4.3 *Line tension and intrinsic noise*

Noise is not only unavoidable, given the microscopic scale of cells, but also a feature that allows rearrangements in tissues. *In-silico* in the vertex model, T1 transitions have an energetic barrier [Bi et al., 2014]. In general, noise is needed to allow cells to rearrange [Bi et al., 2015], and only in energetically very unfavorable configurations, a noiseless cell group will exchange neighbors.

In our model, noise will be included by promoting the line tension to a stochastic function of time, independent in each edge $\Lambda \to \Lambda(t)$. For details, see appendix A.

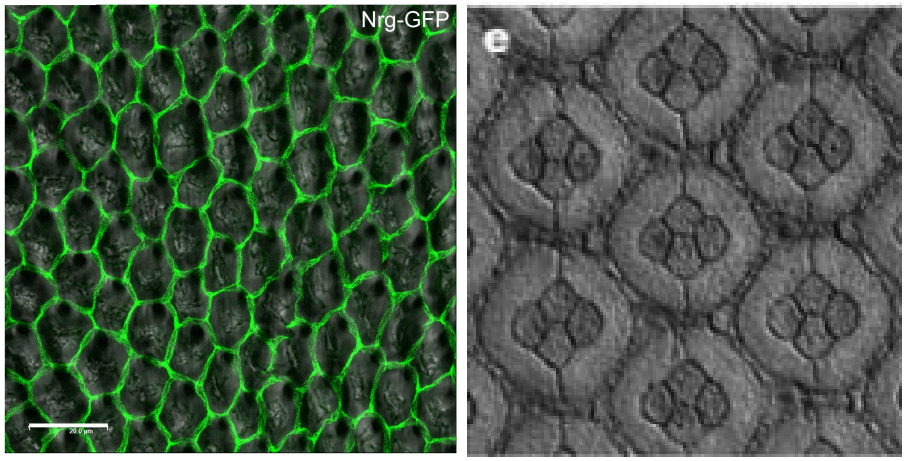

Figure 2.4: Two examples of epithelial tissues showing different packings. Cellular arrangement in the new wing blade [Iyengar, 2012]. Array of ommatidium from *Drosophila* retina [Hayashi and Carthew, 2004].

2.5 CELL PACKING

The way that cells are packed in epithelia is strongly linked to their function. Therefore, it varies among different regions and stages of development. In *Drosophila*, the wing epithelium starts as an irregular packed tissue then becomes hexagonally packed during pupal development. The number of defects diminishes until the tissue becomes almost honeycomb-like [Classen et al., 2005] (see figure 2.4). In the notum, the epithelium is also organized in hexagonal arrays, except for the inclusion of sensory organ precursors (SOP) that appear in patterns in the tissue [Corson et al., 2017].

Other interesting examples can be found in the different epithelia forming the eye: cells in the eye lens are arranged in a precise honeycomb structure of almost identical cells to optimize the lens transparency [Tardieu and Delaye, 1988]. In contrast, the retina consists of a hexagonal array of ommatidia, groups of twenty cells arranged with four cone cells at their centers, shaped to optimize the contact between them [Hayashi and Carthew, 2004].

The packing of cells is also affected by the shape of the tissue, and it cannot necessarily be fully characterized by its two-dimensional representation. Epithelium forming a curved surface will adopt a scutoid morphology, where cells will have different neighbors in the apical and basal domain [Nelson, 2018].

To the greatest extent, an epithelium is mostly composed of six-sided cells of similar size [Classen et al., 2005, Gibson et al., 2006, Farhadifar et al., 2007, Narimatsu et al., 2009]. This kind of packing will be the subject of the following subsections. Some

properties arise from fundamental geometry, others are a consequence of processes like cell proliferation, and others are the result of the interplay of mechanical forces.

2.5.1 *Euler characteristic in planar cell arrangements*

A constraint in the geometry of tessellations of convex polygons follows from Euler's theorem. The number of cells N_c, edges N_e and vertices N_v are related by the following expression [Springer Verlag GmbH, European Mathematical Society,]

$$N_v + N_c - N_e = \chi, \tag{2.5}$$

where χ is called the Euler characteristic of the tessellated surface, for a torus, or cells under periodic boundary condition, $\chi = 0$. For a sphere $\chi = 2$. Since rosettes are rarely observed in many tissues, i.e. vertex, where more than three cells converge [Bardet et al., 2013] (although, there exist cases where more than three cells converge in a vertex [Blankenship et al., 2006]), each vertex is supposed to connect only three edges, and the edges connect two vertices. Then it follows $3N_v = 2N_e$. Therefore, $N_c = N_e/3 + \chi$. Moreover, given that each edge is the side of two cells, we have that the number of sides is $s = 2N_e$, implying $N_c = s/6 + \chi$; the number of neighbors per each cell tends to six as the number of cells tends to infinity. This happens in simulations with periodic boundary conditions, where $\chi = 0$, the average number of neighbors is exactly six.

2.5.2 *Geometric order in proliferating tissue*

Euler's theorem constrains the average number of cell sides, but not the distribution of cell sides among cells. *In-vivo*, it has been observed that the most frequent number of neighbors is six, even more, when the tissue reaches equilibrium. Cell proliferation is a key element in explaining the frequency of six-sided cells in the tissue and reproducing a simple calculation found in ref. [Gibson et al., 2006], we can write a Markov process to describe how the distribution evolves, counting the probability of creating a cell of a different number after a division, writing the matrix schematized in figure 2.5. From this model, a robust quantitative prediction arises; a proliferative tissue approach exponentially a stable equilibrium distribution of polygons, regardless of the initial distribution, and without referring directly to any assumption in cell mechanics.

First, the edges of the mother cells will be distributed among the two daughter cells. The transition matrix P has the elements P_{ij} which represent the probability that a i-sided cell divides to produce a j-sided cell. To build this matrix, let us consider at generation $t-1$ one cell which has s_{t-1} sides, and define the random variable K_t that represents the number of edges distributed to one daughter cell, leaving $s_{t-1} - K_t$ to the other. Right after the mitosis of one cell, each daughter cell must receive at least two sides from their parent, as no 3-sided cells are observed experimentally, leaving $s_{t-1} - K_t$ junctions to be distributed. If each edge can be picked with the same probability, $P_{ij} = Pr[K_t + 2 = \mathrm{Comb}(i-4, j-4)/2^{i-4}]$, where $textComb(a, b)$ is the number of ways

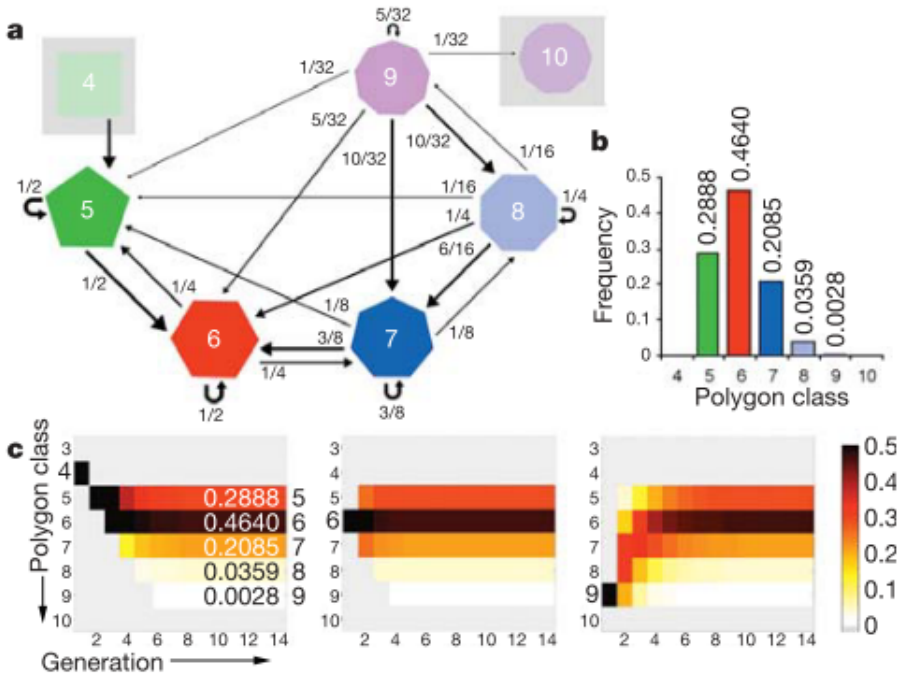

Figure 2.5: **Top:** Diagram of possible transitions and their probabilities as result of the n-sided cell division, defining a Markov chain that produces the distribution shown in b. **bottom** The convergence to this distribution is exponential, regarless of the initial condition. Image reproduced from ref. [Gibson et al., 2006].

to choose b objects from a group of a objects. Before normalization, the elements of the matrix P are given by the coefficients of a Pascal's triangle.

Now we can derive the "shift matrix" S, where the elements S_{ij} account for the effect on a i-sided cell of a neighbor cell dividing to become a j-sided. Each mitosis adds one side in two neigboring cells. If there are N_c cells, $2N_c$ sides are created after a division cycle. Having then $2N_c$ cells, in average each cell gains one side. Therefore, the entries in S are $S_{ij} = \delta_{j,i+1} = 1$ if $j = i + 1$ otherwise 0.

Recapitulating the matrices are,

	post-mitotic class				
P	4	5	6	7	8
4	1				
5	1	1			
6	1	2	1		
7	1	3	3	1	
8	1	4	6	4	1
9					...

	after neighbor divisions				
S	4	5	6	7	8
4	0	1			
5		0	1		
6			0	1	
7				0	1
8					0
9					...

Given a distribution of polygonal class $\mathbf{p^{t-1}}$ at time $t-1$, where $\mathbf{p^{t-1}}$ is a column vector with elements $\mathbf{p^{t-1}} = [p_4, p_5, p_6, p_7, p_8, \dots]$, the distribution after a cycle of division will be given by the following Markov chain,

$$\mathbf{p^t} = \mathbf{p^{t-1}} PS \tag{2.6}$$

The distribution of polygonal classes converges regardless of the initial distribution, as shown in figure 2.5.

2.5.3 *Lewis' and Aboav-Weaire's law*

In a disordered tissue, individual cells exhibit a wide variety of shapes. The simplest way is to classify different cells by their number of neighbors and sides. For each cell, this number defines its polygonal class. With this categorization, a first observation found in biological tissues is that cells with more neighbors are usually bigger than cells with fewer. This can be written approximately as a linear relation.

$$\frac{\langle A_n \rangle}{\langle A \rangle} = 1 + \lambda(n-6), \tag{2.7}$$

where $\langle A_n \rangle$ is the average area of a n-sided cell,$\langle A \rangle$ the average cell area, and λ a parameter that depends on the tissue. This relation is known as Lewis' law [Chiu, 1995]. Section 2.5.4 presents a discussion of the mechanical origin of this effect.

Furthermore, in random tessellations, as epithelia or Dirichlet domains, Lewis observed that a cell adjacent to a cell with a large area has a bigger probability of having a small area and having fewer neighbors. Aboav–Weaire's Law states that n-cells will have

neighbors with m_n sides on average, with a decreasing m as n increases and vice-versa. Aboav-Weaire's law [Chiu, 1995] in one (but not the only one) of its approximation reads,

$$m_n = 5 + \frac{6 + \sigma_n}{n} \tag{2.8}$$

Here σ_n is the dispersion in the number of sides for the cells in a particular tissue. More precise expressions (but not altogether rigorous) can be found in ref. [Chiu, 1995].

2.5.4 *Ground states of the vertex model*

The ground-states in the variational vertex model (2.3) depend on two normalized parameters from the model: the normalized line tension $\bar{\Lambda} = \Lambda / K A_0^{\frac{3}{2}}$ and the normalized perimeter contractility $\bar{\Gamma} = \Gamma / K A_0$. The bars will be omitted in the following. The normalized new parameters measure strength compared to that of area elasticity. On the one hand, as the normalized perimeter contractility increases, cells minimize their perimeter, by shrinking their area and also by increasing their roundness. On the other hand, an increase in the normalized line tensions will induce a decrease in the cell area, eventually leading to its collapse. A decrease in the line tension will make cells with a larger perimeter with respect to their areas more energetically favorable.

The interplay of these two forces will give rise to two regions of ground-states. If the Γ is large enough, cells have a strong preference for rounder shapes, and the ground state will be a regular hexagonal network. As Λ becomes more negative, related to an increase in cell-cell adhesion, the system will tend towards cells with bigger perimeters, and the coexistence of multiple ground states in a soft network, as shown in figure 2.6.

In the case of irregular tissues, the geometry of force-balanced states will vary continuously with the parameters. As the contractility Γ increases, compression will affect more cells with large perimeter with respect to their area, increasing the dispersion of cell areas. The key point is that more sides allow rounder shapes, and the compression force over the cells will be weak compared to the area elasticity. This effect can be used to constrain the set of parameters to model a particular biological tissue, measuring the Lewis' law effect, the average size of cells with a given number of neighbors, as depicted in figure 2.7.

However, if the slope of the Lewis' law depends on the relation between the line tension and contractility, once fixed the value of, for instance, Γ, we can tune a value for Λ to match a given slope. An additional measure is needed to select a particular set. Ref. [Farhadifar et al., 2007] used the response of the tissue to ablation. They conclude that the parameters of case I ($\Lambda = 0.12$ and $\Gamma = 0.04$) reproduce well the geometry of epithelium in the wing disc of *Drosophila*.

Ref. [Farhadifar et al., 2007] defined, apart from case I, four other sets of parameters highlighted in figure 2.7 to represent different types of geometries that can be obtained by relaxing irregular tissues. This work will use the set of parameters of case I as default, and the other cases eventually for comparison.

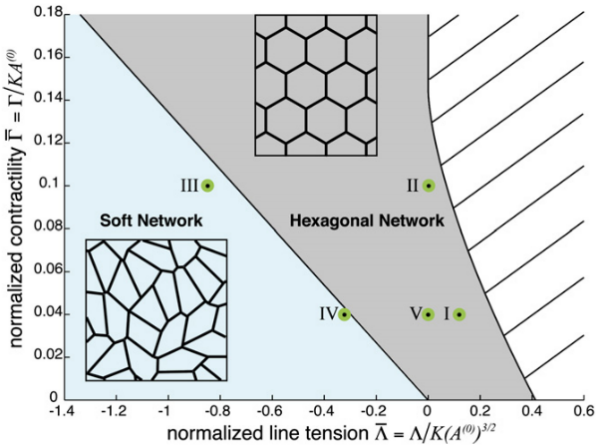

Figure 2.6: Ground-State diagram of the Vertex Model, as a function of the normalized line tension Λ and contractility Γ. The Gray Region, honeycomb networks are the most stable configuration. In the soft blue region, many configurations coexist. The striped region cells, the line tension is large, and the cells collapse. Green dots indicate parameter values of five different cases (case I: Λ =0.12, Γ =0.04; case II: Λ =0, Γ =0.1; case III: Λ =-0.85, Γ =0.1; case IV: Λ =-0.32, Γ =0.04; and case V: Λ =0, Γ =0.04).reproduced from ref. [Farhadifar et al., 2007].

2.5.5 *Rigidity transition in the vertex model*

The description of ground states does not address dynamical aspects of the vertex model. In particular, a relevant question arises on cell migration, and how it occurs in tightly packed networks. In a random tessellation, after initial re-arrangements, the tissue stays in a solid-state where each cell keeps its neighbors indefinitely. A small level of noise does not change this scenario. Nonetheless, as the level of noise increases, this amorphous solid will approach a rigidity transition, that is, the diffusion coefficient for the movement of particles does not vanish, and the system passes from a solid-like behavior with cells *caged* in their position to a fluid-like stage [Angelini et al., 2011, Bi et al., 2015].

Usually, the control parameter of the liquid-to-solid transition is the density [Berthier and Kurchan, 2013, Henkes et al., 2011]. Interestingly, random tessellations are built without extra-cellular gaps, and therefore, the density is constant. [Bi et al., 2015] shows that the vertex model, presents a different rigidity transition, where the order parameter corresponds to the single-cell mechanical parameter; they observed how the energetic barrier decreases with the increase of the target perimeter p_0 in equation (2.4). A small value of p_0 created stronger activation energy for neighbors exchange.

This is not only expected for cells in the epithelium, and has been observed in three-dimensional embryonic tissue [Schoetz et al., 2013].

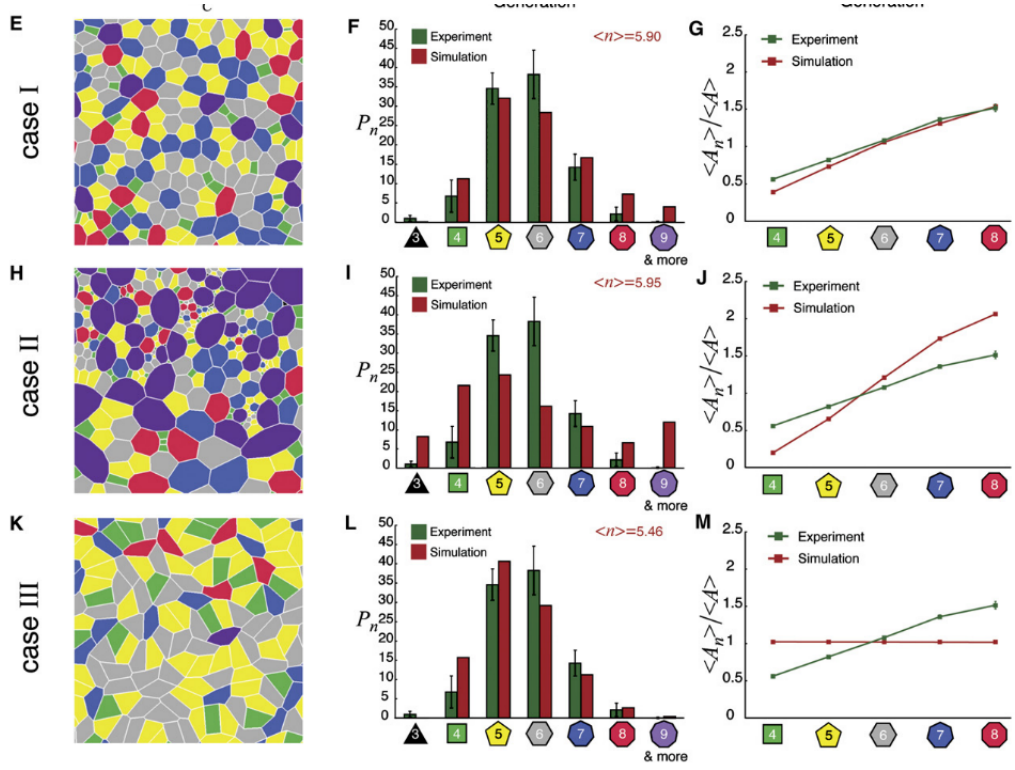

Figure 2.7: Vertex model simulation results for three sets of parameters, here referred as case I $\Lambda = 0.12$, $\Gamma = 0.04$; case II $\Lambda = 0$, $\Gamma = 0.1$; and case III $\Lambda = -0.85$, $\Gamma = 0.1$, respectively ordered from top to bottom.**Left:** Examples of equilibrated tissues under different sets of parameters, exhibiting some examples of cell packing that can arise from the vertex model. Each cell is colored by its number of neighbors.**Center:** Distributions P_n of polygonal classes in each of the cases, where the green bars in each panel indicate the same experimentally determined distribution of neighbor numbers in the third instar wing imaginal disc, for comparison.**Right:** Average areas of different polygon classes normalized to the average area of cells in the network, for different parameters, compared to the experimentally determined values for the third instar wing disc. Image reproduced from ref. [Farhadifar et al., 2007].

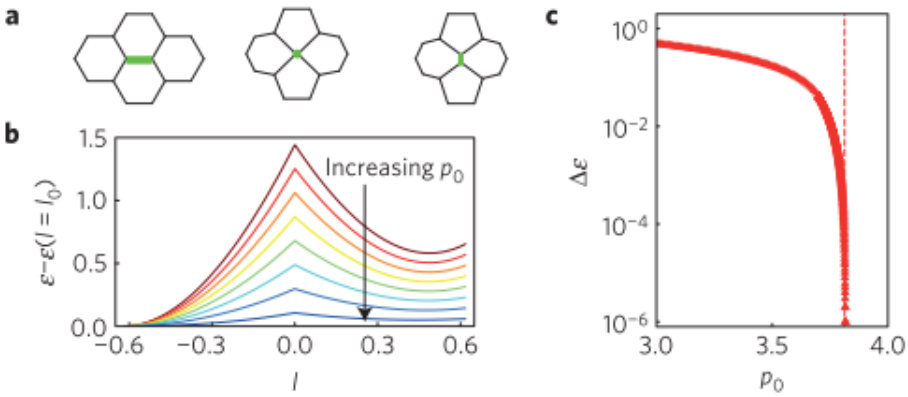

Figure 2.8: The direct environment of an edge undergoing a T1 transition b, Energy of a four-cell aggregate during a T1 transition. Negative lengths correspond to length after the transition. The energy function used is given by the expression (2.4). The maximum of the energy occurs at the point where the length of the edge vanishes. p_0 takes values from 1.5 to 3.8 in equal increments. c. Energy barrier height as a function of p_0. At a certain critical point, the barrier disappears. Image reproduced from ref. [Bi et al., 2015].

2.6 TENSION INFERENCE FROM APICAL GEOMETRY

Measuring forces in tissues can provide critical information on mechanics in the tissue and on its morphogenesis. In general, to measure tension in-vivo, several methods have been developed [Bonnet et al., 2012]. Here we will focus on the experimental method of laser ablation and some non-invasive methods.

2.6.1 *Laser ablation*

The method of laser ablation uses a laser to destroy with a tightly focused laser biological structures that support force transmission, mainly cell-cell junctions, but also cytoskeletal filaments of cells [Ma et al., 2009]. The observed recoil movement can be used to infer the tension [Ishihara et al., 2013] (see figure 2.9).

Here the junction is consider elastic, with E being its elastic constant, moving in an overdamped media with viscosity μ and a length L. The initial tension is T_0, and assuming the network is in mechanical equilibrium, that must be the magnitude of the forces produced by adjacent junctions. After the ablation, if the junction reaches a new equilibrium, it can be modeled as a Kelvin–Voigt material [Fernandez-Gonzalez et al.,

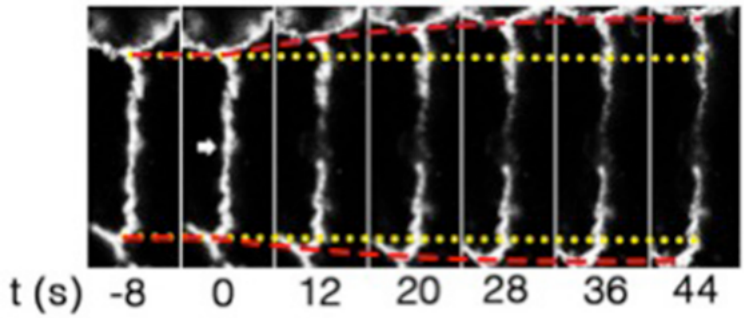

Figure 2.9: Example of an ablated junction. The horizontal direction shows different frames. Yellow lines are the initial position of the junction vertices. Red lines are the position evolving in time. Image reproduced from ref. [Liang et al., 2016].

2009], and the equation that governs the length L after tension in the junction vanishes is $T_0 = E\,[L(t) - L(0)] + \mu dL/dt$ The solution of this differential equation reads,

$$L(t) = -\frac{T_0}{E}\left(1 - \exp\left[-\frac{E}{\mu}t\right]\right) + L(0) \tag{2.9}$$

Measuring the trajectory of the vertices of the ablated junction, the distance is fitted using $L(t) = (v_0/k)\,(1 - \exp[-kt]) + L(0)$, where k and v_0 are free parameters. The relaxation rate is k related to the mechanical parameters as $k = E/\mu$ and the initial recoil $v_0 = T_0/\mu$. Assuming the viscosity is similar between junctions, the value of v_0 is considered proportional to the tension.

2.6.2 *Non-invasive methods*

Laser ablation is destructive, and it can just report the tensions in a few junctions in tissue. These issues can be overcome with an alternative approach that takes advantage of the planarity of the network, allowing to write a simple force equation at each vertex. Assuming that the tissue reaches mechanical equilibrium instantaneously, we can solve the inverse problem of finding the forces that are compatible with a given geometry.

The simplest force inference method considers the tension as the only relevant force. Under this assumption, the relative tensions between edges are determined by the angle between them. If they are equal to 120°, the three edges share the same tension. Otherwise, the biggest tension corresponds to the edge opposite to the smallest angle.

In one approach, the pressure acts normally along the edge. After the inverse problem solves simultaneously for the tension and the pressure. In the other approach, the edge is no longer considered straight.

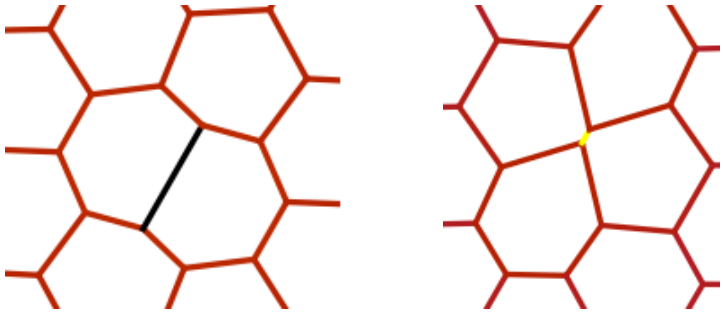

Figure 2.10: In the left, infering from the angles. The black edge has a relative low tension. By contrast, in the right, the relative tension of the yellow edge is bigger.

Dynamical equation and the inverse problem

Let $\vec{r}_i$ and $\vec{r}_j$ be the vertices belonging to the interface ab and let $\vec{r}_{ij}$ be the vector from vertex i to j. In that way, for each vertex i, the total force F_i produced by its neighbours $\{j\}$is given by

$$F_i^\alpha = \sum_{\{j\}} \frac{r_{ij}^\alpha}{|r_{ij}|} T_{ij} + \frac{1}{2} \sum_{\{j\}} \frac{r_{ij}^\alpha}{|r_{ij}|} (P_a - P_b). \tag{2.10}$$

Here, α represents the two different coordinates $\alpha \in \{x, y\}$. Assuming the system reached the steady state, we can impose $F_i^\alpha = 0$ for all i and α. To avoid the trivial solution $T = 0$ and $P = P_0$, we must impose extra conditions. For instance, [Chiou et al., 2012] propose adding the equation $\bar{T} = \sum T_i / E = 1$. In a matrix form

$$M\mathbf{X} = C, \tag{2.11}$$

where M is an $(d+1) \times u$ matrix and $\mathbf{X}^T = (T_1, T_2, \dots T_{N_e}, P_1, P_2 \dots P_{N_c})$ and $C^T = (0, \dots 0, 1)$. The matrix is not square. However, the system can be solved with the method of the pseudo-inverse, obtaining as the general solution

$$\mathbf{X} = \Psi + \sum \alpha_n \phi_n, \tag{2.12}$$

where $\Psi = M^{-1}C$ and ϕ_n element of the kernel of M, and α_n are the amplitude of those zero-modes. To choose a particular solution, extra assumptions must be imposed.

Nevertheless, this solution has an important problem, with respect to the stability under perturbation of the position of the vertices [Chiou et al., 2012]. One way to address this problem is to reduce the number of parameters, for instance, considering a constrained pressure $P_c = P_0$ for all cells. The system becomes over-determined, and a solution for T_e can be obtained as the result of a least-square minimization,

$$\mathrm{Tr}\left[\left(M'\mathbf{X} - C \right)^T \left(M'\mathbf{X} - C \right) \right], \tag{2.13}$$

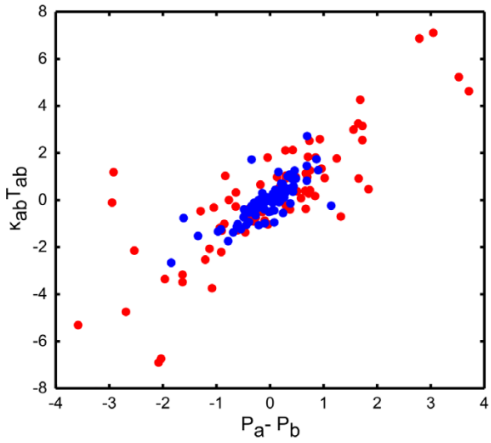

Figure 2.11: Scatter plot comparing inferred pressure differential across an interface, $P_a - P_b$, with the product of inferred tension T_{ab} and the measured curvature kab of the same interface. Different colors distinguish results obtained from different images. The scatter plot exhibits a clear correlation between the two quantities, as expected from Laplace' law $P_a - P_b = k_{ab}T_{ab}$. Image reproduced from ref. [Chiou et al., 2012].

Where M' is the matrix derived from M by removing the columns associated with the pressure, the solution is still given by the pseudo-inverse of the rectangular matrix M'.

Could we, using the more stable framework of an over-determined system of equations, still take into account the pressure? A method is proposed in [Brodland et al., 2014]. Again, a matrix that relates tensions and forces in each vertex is built, but instead of assuming straight edges, the edges are considered curved, and the matrix is built as follows,

$$F_i^\alpha = \sum_{\{e\}} v_{i,e}^\alpha T_e \tag{2.14}$$

where the unit vectors $v_{i,e}$ are constructed as a tangent to the limiting angle at which the junction e approaches the i-th triple junction and point away from the junction. The summation runs over all edges that connect to that vertex. This system has the same dimensionality as the method with straight edges. A new set of linear equations can be written to recover the pressures from the inferred tensions, making use of the Laplace's Law

$$\Delta P_e = k_e T_e \tag{2.15}$$

Here, we have a relation between the different of pressure Δp_e, curvature k_e and tension T_e of an individual edge e. The curvature k_e can be directly obtained from the tissue image. This can be rewritten as,

$$G_P \mathbf{X}_P = \mathbf{q} \tag{2.16}$$

where G_P is an $(N_e + 1) \times N_c$ matrix $\mathbf{X}_P^T = (p_1, p_2, \ldots p_{N_c})$, and $\mathbf{q}^T = (k_1 T_1, k_2 T_2, \ldots k_{N_e} T_{N_e})$.

3 A FIRST VISIT TO EXPERIMENTAL DATA AND THE QUESTION IT RAISES.

In this section, we will present the aim of our endeavour and introduce an experiment where the theoretical framework developed during this thesis work will be applied: how to understand better the disorder found in tissues? Can we infer from mechanical geometry and cell parameters in epithelial development?

3.1 TACKLING THE HETEROGENEITY OF EPITHELIAL CELLS

This thesis presents the research of tools that can be applied to multiple situations in epithelium development and morphogenesis. We want to deduce the right parameter to model a tissue from the geometry that can be measured at different stages of the development of the organism. We discuss an example where these tools can give us insight into the mechanical forces playing a role in the shape and topology of an epithelium. In particular, we present briefly an experiment where we apply our tools.

Here we will present the questions taking one experimental situation in particular. In the following chapters, a framework to address this question will be developed, and finally, in chapter 7, we will come back to this experiment to give an answer to the problem.

3.1.1 *Examples of non-mechanically homogeneous epithelium*

Different types of epithelial cells interacting in a tissue can be found in several situations in an organism: for instance, in *Drosophila*, the veins found in the wings [Blair, 2007,de Celis, 2003] or each segment in its larval development [Larsen et al., 2003]; or it can be an isolated cell as the sensory organ precursor (SOP) found in the thorax, or a group of cells that are embedded in the middle of a rather homogeneous group of cells. Tumoral cells in epithelium express different mechanical properties than their healthy counterparts, and specific mechanical changes can be crucial to tumor metastasis [Wei and Yang, 2016]. Tissues count with tumor suppressors that change mechanical properties and can result in the sorting of tumorous clones to minimize their contact with wild-type cells [Bosveld et al., 2016a].

3.2 GOING BACK AND FORTH BETWEEN THE MODEL AND THE EXPERIMENTAL DATA

In this thesis, we focus on a widely used epithelium model to get insight into their mechanical and geometrical features. Simulations represent a playground where we

can more easily test hypotheses and understand the effect of modification of certain parameters.

To a great extent, the vertex model recovers the mechanics of epithelium. A deeper understanding of the model is providing clues of what we can find in the system that inspired it. A remarkable characteristic of biological tissues is their disordered nature, and it is one of the obstacles to address the problem conclusively with simple analytical calculations. However, statistical physics allows us to reduce the dimensionality of the problem. To achieve that, we need to create a framework that integrates simple average measures that can capture the disorder of tissue, and in the process, better understanding how different aspects determined the tissue shape.

Experimentally, geometry from the apical domain is one of the easiest information to obtain from individual cells in a tissue. For this reason, it is valuable to be able to infer from the other aspects that drive the development of the cells, for instance, mechanical forces or topological rearrangement, including cell division.

We will ask this question on two levels:

- How can one relate coarse-grained geometrical features in-silico with forces and other specifications on the vertex model by simple equations?

- Can we relate geometry from experimental data with the underlying forces in cellular processes? Furthermore, how does the coarse-grained approximation found in-silico hold *in-vivo*? This will depend on whether and to which extent we have captured the relevant variables in our model. The success found characterizing three independent features using the vertex model in [Farhadifar et al., 2007], and many other works, including the present, make us believe that it is possible.

3.2.1 *Can we infer mechanical parameters from geometry?*

Cells are shaped by internal forces; therefore, we can expect that the answer to the above question is yes, at least to some extent. How successful we can be in this approach depends on several aspects that can represent obstacles. We take a partial description from the cells in the tissue; we focus on the apical domain. We explained in the introduction that this region is the most relevant playground for the interplay of forces that rule epithelium morphogenesis, regardless of this, other forces occurring below this domain could affect the geometry. This thesis focus on the case of static images. In that case, we assume that the tissue is continuously near mechanical equilibrium. On the one hand, there are approaches to do force inference [Chiou et al., 2012, Brodland et al., 2014, Ishihara and Sugimura, 2012], as the methods presented in the background chapter 2.6.2. On the other hand, we will present an analytical approach in chapter 5, where in particular, a mean-field approximation is presented in section 5.2 to describe individual polygonal classes.

3.2.2 *How proliferation affects morphogenesis?*

Besides mechanical forces, the way the tissue is prepared plays an important role in development. For example, in the emergence of topological order due to the proliferation reported by [Gibson et al., 2006] presented in the previous chapter, we observe how that division bias the topology, and therefore the shape of the tissue. This information is more subtle to obtain from geometry, as it can be overwritten by the dynamics. Nonetheless, the way cells divide will leave a mark in the tissue topology, a phenomenon already explored in references [Sahlin and Jönsson, 2010, Li et al., 2012, Aegerter-Wilmsen et al., 2010] where different divisions' rules are compared, or in ref. [Mao et al., 2013] where the influence of differential rates of growth in the different regions is analyzed. That analysis will be revisited in section 4.3 where different proliferation times and the Hertwig's rule found in ref. [Bosveld et al., 2016b]. In section 6.1.2 where the case of a non-proliferative cell is addressed. The case of bias in the orientation around a certain type of cell is presented in section 7.3.3, in the context of the experimental data.

3.2.3 *How different types of cells interact between them?*

All those questions asked with respect to a homogeneous tissue where it is reasonable to assume very similar mechanical parameters can also be asked on tissues where different types of cells interact. In our example: which forces are involved behind the round shape of the clone? Moreover, what forces can be involved in the difference of cell area in both activator and repressor clones? What can the angles on its surface tell us? Is the topology coherent with the supposed division rule?

A simple approach to tackle mechanical heterogeneity is presented in different sections of 6, in particular, to address the case of an individual cell with different mechanical properties in section 6.1, two cells in section 6.3.2, and a cluster of them in section 6.3.1.

3.3 OUR TOOLS AND MODEL WILL BE CONTRASTED WITH EXPERIMENTAL DATA

This thesis has been done in collaboration with the group of François Payre at the University of Toulouse, who has made crucial contributions uncovering the mechanism of cell differentiation in *Drosophila* epidermis, and the role of ovo/shavenbaby in the trichome formation [Kondo et al., 2010]. In one of their current efforts, Maleaume Soulard—Ph.D. student—in the group has studied under the supervision of François Payre the interaction between proliferative cells and cells undergoing the differentiation program [Soulard et al., 2019]. This analysis is done in chapter 7.

3.3.1 *Shavenbaby and timing control in trichome formation*

All cells have a complete copy of the genetic material to form an organism, and in very early stages of development, cells are pluripotent, capable of forming any organ. In

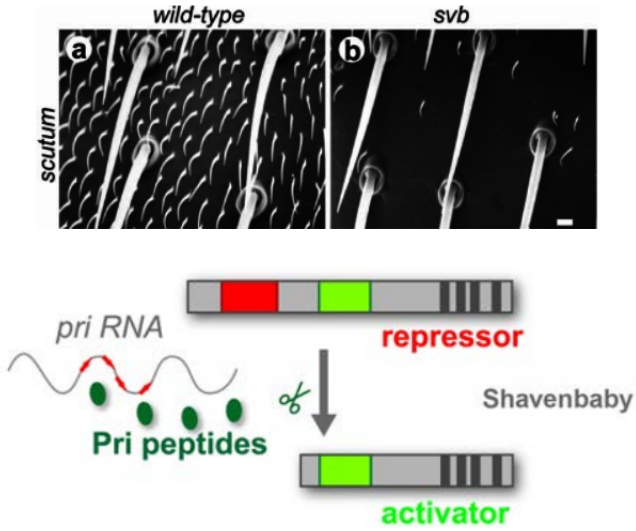

Figure 3.1: **Top:** Trichome formation in the *Drosophila* thorax. In the Sbv mutant at the right (b) we observe that trichomes are replaced by naked regions (Image obtained from ref. [Delon et al., 2003]). **Bottom:** The TF shavenbaby is produced in its repressive form. Pri peptides can catalize the cut and produce the active form of Sbv, acting as a molecular switch of Sbv activity. Image courtesy of François Payre team.

time, a particular cell will differentiate to express a specific function following a precise body plan. This depends on the sensing of positional and temporal information. How a cell-fate is determined given spatial information and how the pattern emerges have been widely explored [Wolpert et al., 2011, Tkačik et al., 2015]. However, the mechanisms underlying temporal control are still poorly understood.

The formation of the trichome, the stereotyped array of cells found in the *Drosophila* thorax, provides a nice example of time-controlled stop of proliferation and start of a differentiation program.

The expression or silencing of a particular gene depends on a cascade of transcription factors (TF). For trichome formation, the transcription factor called Shavenbaby (Sbv) or ovo is required [Payre et al., 1999]. Shavenbaby is the master regulator of epidermis differentiation, as mutants that do not form this TF basically display naked cuticle [Delon et al., 2003]. The production of Shavenbaby is the result of cross regulations of cell signals and genetic cascades that are the product of normal cell development. Shavenbaby is produced in an inhibitory form that indeed prevents cells from differentiating.

Outside the epidermal tissue, the hormone Ecdysone is produced, which has the main role of controlling the timing of post-embryonic development, triggering larval molts, and the larval–pupal transition [Yamanaka et al., 2013]. This hormone travels through

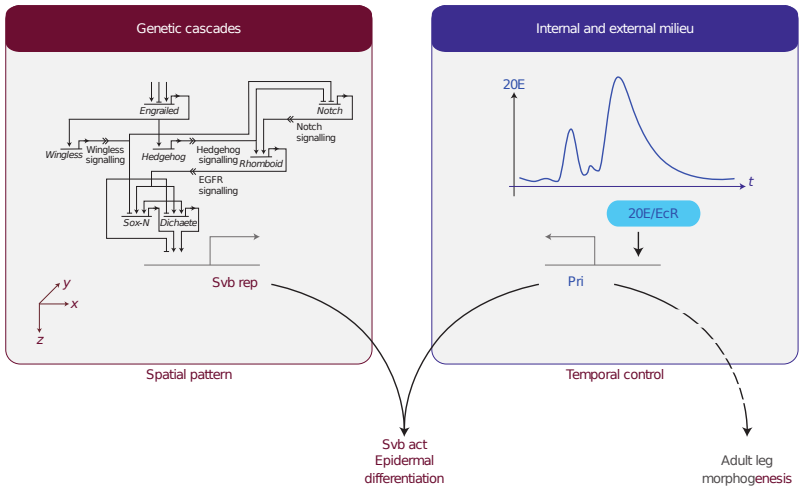

Figure 3.2: Diagram of the conditions to produce the active form the Shavenbaby. Svb production depends on normal cell development. Svb accumulates in its repressive form; cells are held in it proliferative stage. Pri senses the signals from the external milieu. Its production and consequent activation of svb depend on the signaling of the hormone ecdysone. Image reproduced from ref. [Chanut-Delalande et al., 2014].

the larval body. In the epidermal tissue, it induces the production of polished-rice (pri) peptides that catalyze the cut Svb to transform it from its repressive form into its active form that will induce cell differentiation [Chanut-Delalande et al., 2014].

3.3.2 *Experiment of our collaborators: Of the importance of temporally segregating cell proliferation and differentiation during development*

In normal development, cells in the epidermis undergo differentiation in a coordinated manner under the action of ecdysone. Our collaborators have produced *Drosophila* larvae with isolated clones of cells that are being kept in proliferative states; meanwhile, cells around start the differentiation program (ovo A or repressor case), and vice-versa, clones where cells are driven to an early differentiation (ovo B or activator case). Six hours before the *white puparium* stage [Pak and Gilbert, 1987], the larvae are subjected to a heat bath that will drive some cells at random to become ovo mutants, leaving the majority of cells unaffected. In both cases, ovo A and B, we want to understand how cells change, and in particular, our contribution is to provide an insight on systemic responses of the tissue. Examples of those clones at 38 hours after the *white puparium* can be found in figure 3.3.

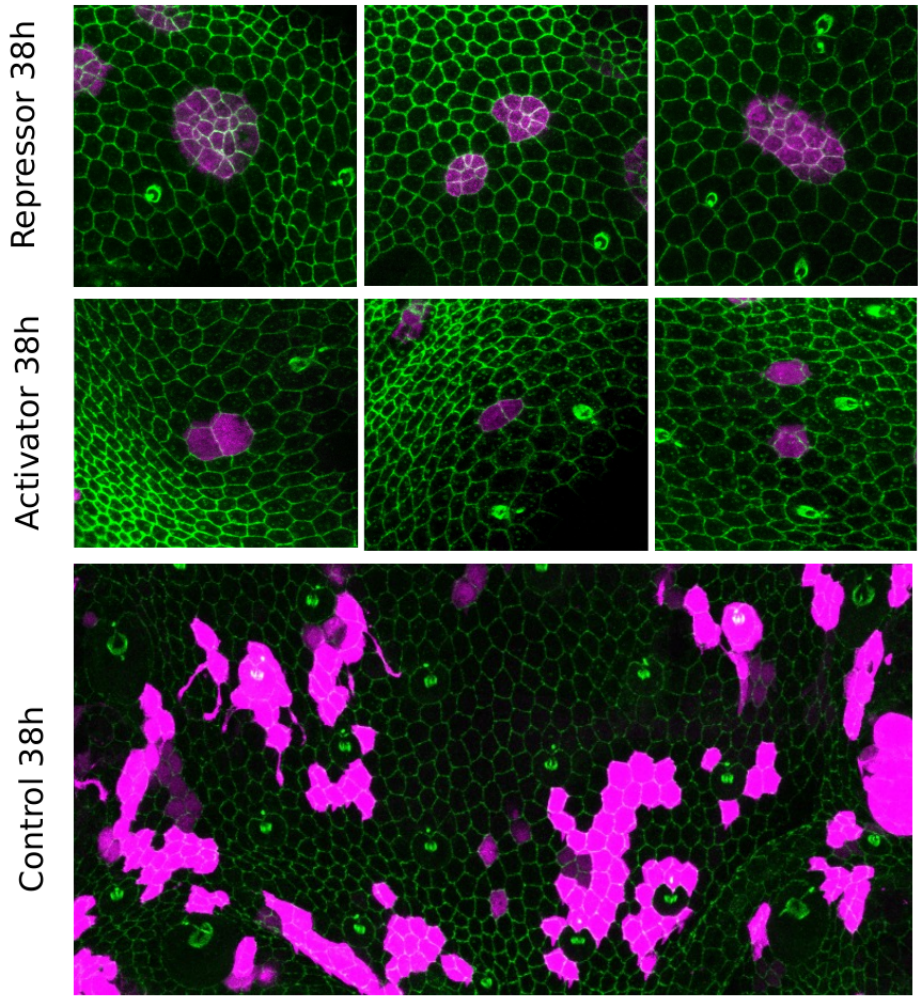

Figure 3.3: Clones at 38 hours. Clonal cells are highlighted by purple color, and the membranes in green (GFP-Arm).**Top:** Repressor clones at 38 hours. They develope into clusters without a round shape, with cells that are on average smaller than WT cells. **Middle:** Activator clones at 38 hours. Clones have only one or two cells, that appear in diverse sizes, but with a tendency to be bigger than WT cells. **Bottom:** Control clones. They have many cells, and, as expected, the cell is not different from WT cells. The first feature that is evident in the repressor case, is that clones have a rounder shape compared with control clones, suggesting a *superficial tension* between the clone and its exterior. This hypothesis is tested by the study of the effect in disordered tissue of the application of a cable of tension over a cluster of cells. The activator case is formed by fewer cells; therefore, the analysis of its roundness is not pertinent. As in this case, proliferation has been stopped early, these clones tend to have fewer cells, and in many cases, the clones only have one cell. Regarding cell area, activator cells are in average bigger, especially in the case of unicellular clones. The images where more than one cell is found, edges between clonal cells are longer, suggesting that their tension may be relatively low.

3.4 OUTLINE OF THE THESIS

Even though the vertex model is a comparatively simple model in regard to the system that it aims to represent, yet it is too complex to be studied without numerical simulations. In the first chapter, a general study of correlations and features of the tissues are presented, along with justification for how parameters have been chosen in the simulations. In the second chapter, a novel approach to study the vertex model is presented: a mean-field approximation that describes a cell by its number of neighbors, and by extension, can describe a disordered tissue composed of these cells. In the third chapter, we use the same approximation to address the inclusion of cells that differ from their environment. In the fourth chapter, we put together the tools that we presented to analyze the experiment performed by Payre's lab (U. de Toulouse) that inspired this work, where a group of cells develops abnormally in the epithelium in the thorax of a *Drosophila* larvae. Finally, we present our conclusions.

Part II

THESIS WORK

4 GENERAL FEATURES OF DISORDERED TISSUES

Vertex models are the central tool that we use to describe forces and mechanical equilibrium in epithelial tissues. In order to model proliferative tissues, we need as well to describe cell division. In this chapter, we introduce our division clock that determines when a cell will divide and the different division rules that describe how cells divide in space. We describe the Hertwig's rule for cell division reported in [Bosveld et al., 2016b] and compare tissues generated under this rule with other ways of choosing the axis of division. We describe the main geometrical properties of proliferative tissues generated by the vertex model with proliferation, analyze statistics from simulations, and focus on how properties as cell area and perimeter distribute among different polygonal cell classes. We report that when cells divide following Hertwig's rule, i.e., according to their geometry, this generates tissues with fewer defects and that are more ordered. Finally, to test the sensitivity of our results to the details of the chosen mechanical model, we introduce a different *pressure-less* vertex model. We find that it behaves similarly to the traditional variational vertex model. We will use this alternative model to test the robustness of our results in the subsequent analyses.

4.1 THE DIVISION CLOCK

4.1.1 *Division time*

In order to simulate a growing tissue, cell division needs to be implemented. Cell division is a complex biological issue. It has been debated whether cells monitor their size ("sizers"), the time elapsed since their birth ("timers") or yet another biological process and this is still a matter of investigation (e.g. [Cadart et al., 2018]). Here, we chose what is perhaps the simplest description: when a cell is born, its lifetime until division is chosen to be t a random variable drawn according to the probability distribution $P_d(t)$. For definiteness, $P_d(t)$ is chosen as,

$$P_d(t) = \frac{1}{\sqrt{2\pi}\sigma}\left[\exp\left[-\frac{(t-\tau_d)^2}{2\sigma^2}\right]\right]_+ \tag{4.1}$$

where the rectification $[]_+$ imposes that the probable density is positive, as it should (σ is chosen small enough so that this does not significantly affect the normalisation).

4.1.2 *Rate of proliferation and distribution of cell ages in an exponentially growing population*

The relation between the distribution of division time $P_d(t)$ and the global rate k of proliferation of the tissue is a classic question of population genetics which dates back to

early investigations by Euler (reprinted in [Euler, 1970]) and Lotka [Lotka, 1907] (see also the review [Painter and Marr, 1968] and the article [Lebowitz and Rubinow, 1974] which generalizes these early results and takes into account correlations between the lifetime of a cell and of its daughters).

One way to determine the growth rate k and the distribution of cell ages in a population is to consider the number $n(t,\tau)$ of cells of age τ at time t, the so-called age-time formalism. The distribution at time t and $t+dt$ are related by

$$n(t+dt,\tau+dt) = n(t,\tau) - D(\tau)n(t,\tau)dt \tag{4.2}$$

or in differential form

$$\partial_t n + \partial_\tau n = -D(\tau)n(t,\tau). \tag{4.3}$$

Equation (4.3) simply says that cells age or divide. Cells that divide give rise to 2 daughters cells of age zero, thus equation (4.3) is supplemented by the boundary condition

$$n(t,0) = 2\int_0^{+\infty} d\tau D(\tau)n(t,\tau) \tag{4.4}$$

The probability $P_d(\tau)$ that a cell divides at age τ is given by a rate of division $D(\tau)$ conditioned on the absence of division up to t. Namely, $D(\tau)$ is related to $P_d(\tau)$ by

$$P_d(\tau) = D(\tau)\exp[-\int_0^{\tau} D(u)du] \tag{4.5}$$

or, inversely

$$D(\tau) = \frac{P_d(\tau)}{\int_\tau^{+\infty} P_d(u)du} \tag{4.6}$$

The growth rate and the age distribution for an exponentially growing population in a steady state are easily obtained if one supposes that $n(t,\tau) = n(\tau)\exp(kt)$, one obtains from Eq. (4.3),

$$\partial_\tau n = -[k + D(\tau)]n(\tau), \quad \text{or,} \quad n(\tau) = n(0)\exp[-k\tau - \int_0^{\tau} D(u)du] \tag{4.7}$$

The boundary condition Eq. (4.4) then gives the self-consistent equation for the growth rate

$$1 = 2\int_0^{+\infty} D(\tau)\exp[-k\tau - \int_0^{\tau} D(u)du] = 2\int_0^{+\infty} P_d(\tau)\exp[-k\tau] \tag{4.8}$$

where in the second equality, the relation (4.6) between $D(\tau)$ and $P_d(\tau)$ has been used. Eq. (4.8) was explicitly written in this form by Lotka [Lotka, 1907]. The distribution of time τ until the next division, that is the fraction of cells present at time $t = 0$ that will divide at time τ is,

$$P_T(\tau) = N\int_\tau^{\infty} \exp\left[-k(\tau-\tau')\right] P_d(\tau')d\tau' \tag{4.9}$$

$$= N\exp\left[k\frac{k\sigma^2+2\tau-2}{2}\right]\left(1 - \mathrm{erf}\left[\frac{k\sigma^2+\tau-1}{\sqrt{2}\sigma}\right]\right), \tag{4.10}$$

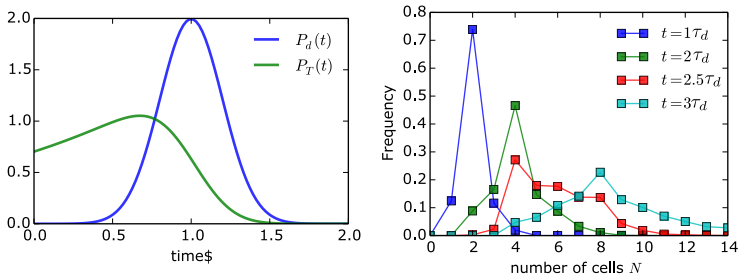

Figure 4.1: **Left:** Distribution of division age $P_d(\tau_c)$ (blue) and distribution of time until next division $P_T(\tau_c)$ (green) for $\sigma = 0.2$ and $k = 0.702$. **Right:** Distribution of number of cells descendent from a same cell at time $t = 0$ at different times, for an initial distribution of cells with next-division time from the distribution (4.10)

where N is a normalization factor, and τ_d has been taken equal to 1 in the second equality. In our simulations, we use $\sigma = 0.2\tau_d$. With this value, the solution of Eq. (4.8) is $k \approx 0.703$.

4.2 CELL FEATURES STATISTICS

The energy function (2.3) can be normalized in space and energy, leading to ground states depending only on two parameters, the line tension Λ and the perimeter contractility Γ. Two main regions can be distinguished, one where the ground state—the state that minimizes the energy function—is a hexagonal lattice, and the other one where energy relaxation produces soft networks. As a representative sample of the different behaviors that the model exhibits, we will take three of the cases considered in [Farhadifar et al., 2007], those being:

- **Case A** $\Lambda = 0.12, \Gamma = 0.04$: this corresponds to parameters that describe well the epithelium in the wing of drosophila in the larval stage.
- **Case B** $\Lambda = 0, \Gamma = 0.1$: In this case, the perimeter contractility is high compared to other forces, and cells of the different polygonal class will have very different expected areas, with cells of more sides being noticeably bigger than cells with fewer sides.
- **Case C** $\Lambda = -0.32, \Gamma = 0.04$: In this case the adherence dominates the tensile force. Cells of different polygonal classes have similar areas on average, as the preferred perimeter p_0 is positive, and the area term is not opposed by the perimeter term and both can be minimized, giving rise to a soft network.

Case A and Case B both have as ground state a hexagonal lattice but with a different equilibrium area per cell. In these two cases, all cells are convex, in contrast to the soft

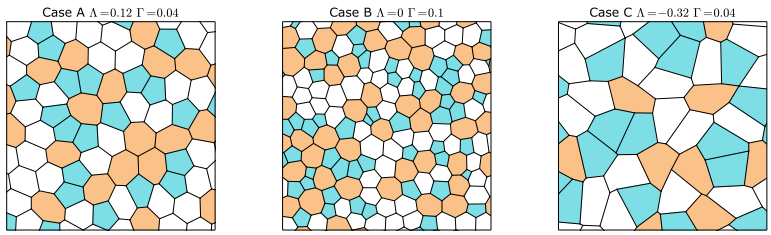

Figure 4.2: Examples of tissues under different conditions. Cells with more than six neighbors are shown in orange. Cells with less than six neighbors are shown in cyan. The tissues were generated after 2 cell cycles of proliferation, i.e, during a time $t = 2t_d$, starting out with 15 cells, following the Hertwig's rule and the division clock defined in the previous section.

network case exemplified by Case C, where several concave cells are found. This arises as in the soft network case, cells have an area close to the preferred one A_c. This makes the force derived from the cell pressure rather weak as compared to adhesion, and these biases cells to adopt shapes with longer perimeters.

All our simulations are run under periodic boundary conditions, and more details about the implementation can be found in the appendix A.

An important aspect is how to choose the noise intensity for a different set of parameters. For case A, the intensity of the noise has been fixed by comparison with fluctuations in experimental tissue to $\eta = 0.3$, meaning that the value of the line tension Λ varies by 30%. We do not have experimental examples of tissues modeled by another set of parameters and their level of noise. Therefore, how to choose noise for different parameters is ambiguous. One way to address this is to simply keep the rule of that the line tension Λ should vary by the same amount as in case A. However, in case B, Λ vanishes, and as noise is a crucial ingredient, we need to use different criteria. Instead, the noise intensity can be chosen such that the total tension varies by a comparable amount in each case, where the total tension includes the contribution of the perimeter contractility. This and other details on how the simulations are implemented are described in the appendix.

4.2.1 *Polygonal classes as a meaningful category*

Throughout this thesis, we will be interested in characterizing the complexity of disordered tissues by few parameters that can describe a wide range of mechanical and geometrical features. The energy function in the vertex model depends on the area and the perimeter of each cell. In the region where the hexagonal lattice is the ground state, and pressure forces keep cells to have a convex shape, we find that the cell area strongly correlates with the cell perimeter, as shown in figure (4.3). In this case, the cell area provides a good guess of its perimeter. Notably, this holds as long as the model

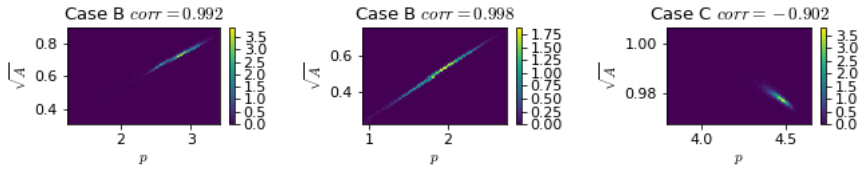

Figure 4.3: Two-dimensional histogram of the pairs of the square root of cell areas $\sqrt{A}$ and cell perimeters p for cases A, B, and C. The color bar identify different percentages found for each bin. We observe a strong linear correlation between two values for case A and B, and a negative correlation in the case of the soft network in case C. The cells are taken from 150 tissues with 60 cells each, that grew from cells generated by the Voronoi tesselation of 15 points drawn from a Poissonian distribution—random points to define cells—under periodical boundary conditions, dividing following Hertwig's rule.

parameters do not fall in the soft-network region. The correlation becomes tighter as the cell contractility becomes stronger, contracting the cells and making the cell pressure more relevant.

In turn, another category that shows weaker correlation with cell area and perimeter, but still allows us to characterize the tissue, is the number of edges of a cell, the polygonal class to which it belongs. In this work, several theoretical analyses will be performed under the assumption that the polygonal class of a cell is a meaningful category; describing an average cell of each of these categories, we then extrapolate to the whole tissue. Analyses of relations between features of individual cells are presented. In particular, between cell area, perimeter, polygonal class, and aspect ratio. To start, in figure 4.4, the average and distribution of area, perimeter, and edge length by each polygonal class is presented.

For the standard parameters (case A), cells of different polygonal classes have defined distributions of area, perimeter, albeit the overlap between different distributions increases for cells with a higher number of sides. However, simultaneously, their dispersion also decreases. Still, the distribution of length between different polygonal classes are not that different; the length of an edge does not give much information about the polygonal class of the cells to which it belongs.

How does this scenario change when choosing parameters in the strong Lewis' law region (case B), or the soft network region (case C)? We observe crucial differences. In a soft network, the polygonal class is no longer a meaningful category. In the strong Lewis' law region, we observe more dramatical differences between different polygonal types.

4.3 HOW CELL DIVISION AFFECTS MORPHOGENESIS

Cell proliferation is evidently a fundamental ingredient in tissue development. In epithelia that aspect has been already partially addressed [Gibson et al., 2006, Ranft et al., 2010]. However, it is not an easy task to integrate the interplay of mechanical forces

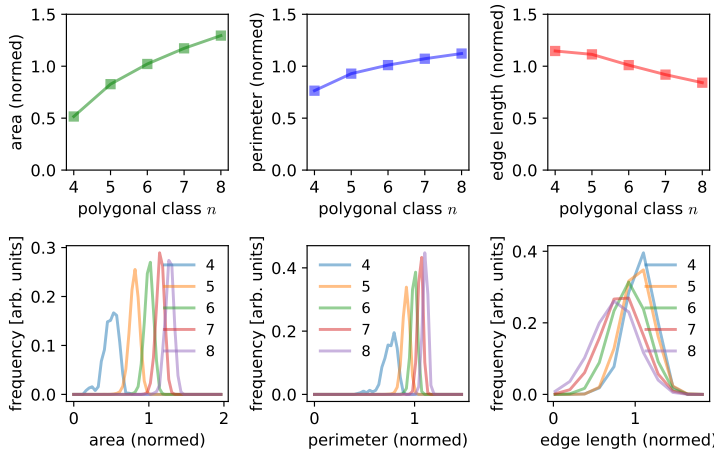

Figure 4.4: Average value (top) and distribution (bottom) for different cell features for each polygonal type, for Case A, normalized by their average. The mean area and perimeter increases with the number of sides, meanwhile the length of individual edges shows a small variation. The cells are taken from 150 tissues, that grew from cells generated by the Voronoi tesselation of 15 points from a Poissonian distribution under periodic boundary conditions, dividing following Hertwig's rule until they reach 60 cells.

Stats.	$\langle A \rangle$	$\langle p \rangle$	σ_A	σ_p	
Case A	0.549	2.788	0.088	0.199	
Case B	0.263	1.904	0.088	0.309	
Case C	0.997	4.039	0.005	0.057	
Distribution P_n	4	5	6	7	8
Case A	0.016	0.274	0.445	0.225	0.038
Case B	0.023	0.267	0.437	0.21	0.055
Case C	0.06	0.337	0.421	0.16	0.021
Area per class A_n	4	5	6	7	8
Case A	0.282	0.452	0.558	0.64	0.707
Case B	0.081	0.175	0.265	0.343	0.409
Case C	0.990	0.996	0.998	0.999	0.999

Table 4.1: Numerical values of the average and dispersion of cell areas and cell perimeters, frequency and average area of each polygonal class, for cases A,B, and C. The simulations are the same that were used in figures 4.4,4.5 and 4.6.

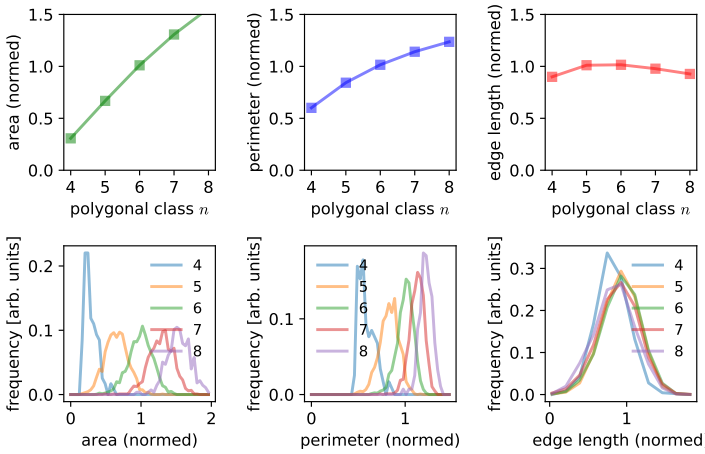

Figure 4.5: Average value (top) and distribution (bottom) for different cell features for each polygonal type, for Case B, normalized by their average. In this case, the cells are smaller than in case A. The average area and perimeter increases with the number of sides. Meanwhile, the length of individual edges only shows a small variation. Simulations are performed in the same fashion as for case A (shown in figure 4.4), only varying the parameters Γ and Λ.

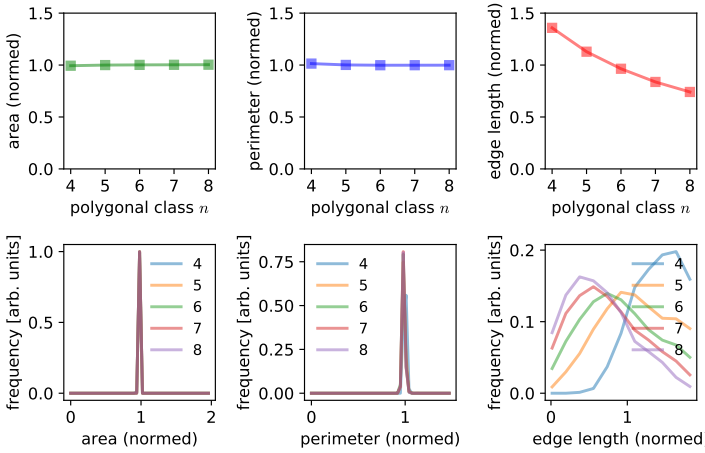

Figure 4.6: Average value (top) and distribution (bottom) for different cell features for each polygonal type, for Case C, normalized by their average. The average area and perimeter are basically equal among polygonal classes. In this case, the polygonal class is not informative about other features of the cell. Simulations are executed in the same fashion as for case A (shown in figure 4.4), only varying the parameters Γ and Λ.

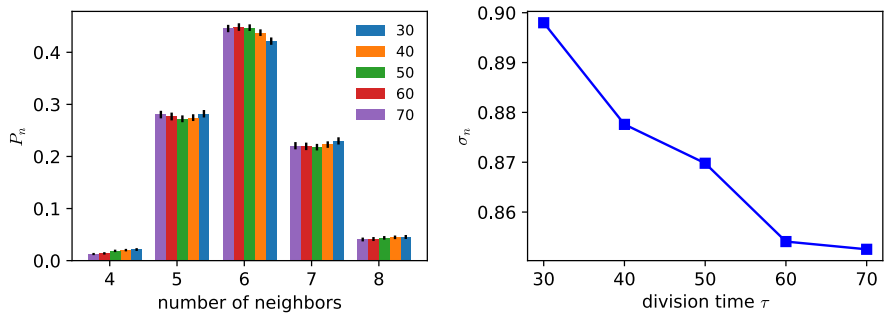

Figure 4.7: Distribution of polygonal classes (**Left:**) and dispersion (**Right:**)—measured as the standard deviation of the number of sides per cell— in the tissue for different average division time τ_d. As time increases, the dispersion decreases, and more six-sided cells are observed. The statistic is recovered from 50 tissues that starting out from 15 cells proliferate until reaching 60 cells.

with the topological changes that proliferation induces, in a comprehensive theoretical framework. Rearrangement can allow the tissue to relax stress and change the topology of the network. In that regard, even non-proliferative tissues created from Voronoi cells determined by a random Poissonian distribution of points will relax into a topology similar to a proliferative tissue. To shed more light on this problem, we will focus on measuring the disorder in tissues regarding the way the cells proliferate, first different division times, and different ways to choose how to divide a cell.

4.3.1 *Fast proliferation rate creates more disordered tissues*

A first element to take into account is the rate at which cells divide. In our model, a time scale is determined by the forces and the noise—that is generated by a stochastic process with correlation time $\tau = 3.9$—that determines the rate of rearrangements. Proliferation creates defects, and how the division rate compares with the time scale of rearrangement determines different levels of disorder in the tissue. A lower proliferation rate will give more time for fluctuations to rearrange cells and to release local stress. That is what we observe in figure 4.7. However, beyond $\tau_d = 60$, there are not important differences compared with longer times. In the simulations presented in this work, this proliferation rate will be used as the default value, if not otherwise specified.

In any case, the differences are in all respects small between the tested proliferation rates. Regardless, in chapter 6, we will explore the case of different proliferation rates between cells in the same tissue, where these cases will manifest a more evident difference phenomenologically.

4.3.2 *Comparison between Hertwig's rule and other division rules*

In order to define the proliferative dynamic in a tissue, it is not enough to know when and how often cells divide; another critical ingredient is the choice of the axis of division. Cells divide following Hertwig's rule, which is based on the position of the vertices [Bosveld et al., 2016b]. However, it is not clear how exactly this will affect the development of a proliferative tissue in comparison with other alternative rules, such as the simple choice of a division axis in a random direction. In this section, we will be comparing different divisions rules, namely:

- **TCJ axis:** The Hertwig's rule that takes into account the TCJ position as described in ref. [Bosveld et al., 2016b] and in the background section. It is the method used by default in this work in general.
- **Main Axis:** A different Hertwig's rule, where the division occurs along the direction of the main axis of the second moment of area, adding a new edge in the direction of the shortest axis. This is the method used in ref. [Fletcher et al., 2013].
- **Random Axis:** The direction of division is chosen at random. A random angle from a uniform distribution between 0 and π is chosen, and a new edge is created passing through the cell geometric center. This is the method used in ref. [Farhadifar et al., 2007].

In addition, we will consider tissues generated, without proliferation, as:

- **Relaxed Poisson:** The tissue is generated by relaxing a tissue generated by the Voronoi cells of points distributed following a Poisson distribution, i.e., points generated by a uniform distribution in the box.

In all the cases, noise is present and catalyzes T1 transitions. Figure 4.8 shows examples of tissues generated under those four division rules. The differences are subtle and not easy detected by the naked eye.

One simple test to measure the discrepancies between these different division rules, it is to look at the polygonal class distribution resulting from various division rule choices. We can identify the differences between contrasting types of proliferation. Hertwig's rule and cells dividing along their main axis create tissues with less defect than tissues where the axis of division is chosen at random, or a Poissonian random network relaxed under noise, as shown in figure 4.9.

However, the discrepancy in the number of defects is not large enough to necessarily expect important changes in the mechanical and topological properties of the tissue, at least not as a consequence of the dispersion in the number of sides. But, if we wish to characterize how organized or disordered the tissue is, a complementary measure is provided by the radial pair distribution function in two dimensions $G(r)$, defined as

$$G(r) = \frac{1}{2\pi r\rho} \sum_i \sum_{j \neq i} \left\langle \delta(r - r_{ij}) \right\rangle , \tag{4.11}$$

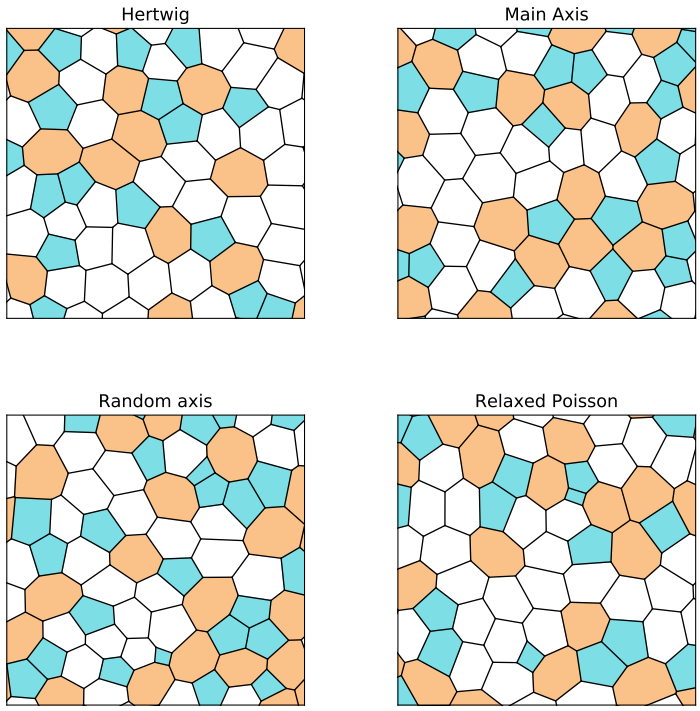

Figure 4.8: Examples of proliferative tissues generated with different division rules. Cells with more than six neighbors are in orange, and cells with less than six neighbors are in cyan. The tissues were generated with the parameters of Case A ($\Lambda = 0.12$ and $\Gamma = 0.04$) after two cell cycles of proliferation, starting out with 15 cells generated by the Voronoi cells of a Poissonian distribution of points. In the case of relaxed Poisson, the tissue starts with 60 cells already.

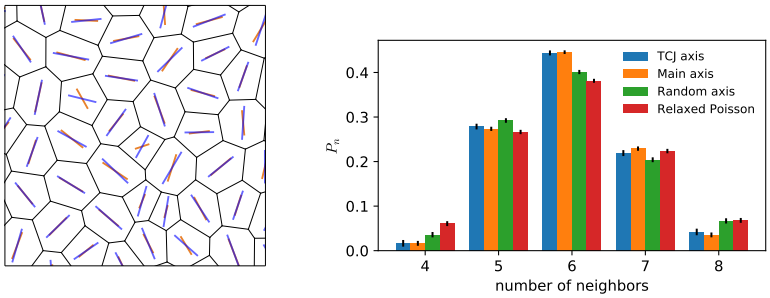

Figure 4.9: **Left:** Example of tissue (case A; $\Lambda = 0.12$ and $\Gamma = 0.04$) and the direction of the axis of the division following Hertwig's rule (blue) and the direction of the main axis of the second moment of area (orange). No important differences are found between them, except for very specific cells. **Right:** Comparison between the distribution of polygonal classes among cells in tissues that proliferated under different rules. Average among 50 tissues that proliferate starting with 15 cells until they reached 60 cells. The original cells were created using the Voronoi cells of 15 Poissonian random points. In the case of relaxed Poisson, the tissue is initialized with 60 Poissonian random points, and there is no proliferation to relax for five units of time with noise.

where ρ is the mean density of cells in the tissue, the function (4.11) describes the variation of density as a function of distance from a reference particle, and it reflects the degree of order of the local environment of a cell. Figure 4.10 shows that random proliferation leads to less structured tissues than when cells divide following the Hertwig's rule or along their main axis.

In figure 4.11, we also compared the distribution of aspect ratios between the different division rules. Dividing a cell along its main axis decreases the average aspect ratio of daughter cells.

4.4 PRESSURE-LESS VERTEX MODEL

Can we trust the vertex model? It depends. Even within the realm of vertex models, a fair question to ask here is how many of the phenomena obtained for the variational vertex model are particular to it, and which others are more general properties of a random tessellation which takes into account inter-cellular forces. To address this question, we can compare the results obtained for the vertex model to a simpler model.

The first proposal for a simpler vertex model is to assume constant pressure and tension. However, this model is not stable, as the equilibrium will only depend on the angles. A meaningful model must have edge tension depending on cell geometry. An

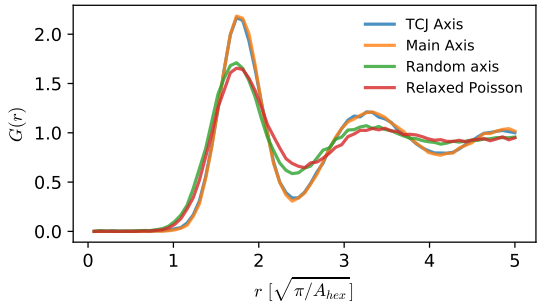

Figure 4.10: Comparison between the radial pair distribution function of cellular centers in the tissue. Distance is normalized considering the effective radius of an equilibrated hexagonal cell. After three cell diameters, pair correlation is almost completely lost in the case of a random axis and relaxed Poisson. Meanwhile, still clear and coherent oscillations are observed for the geometrical bias division rules.

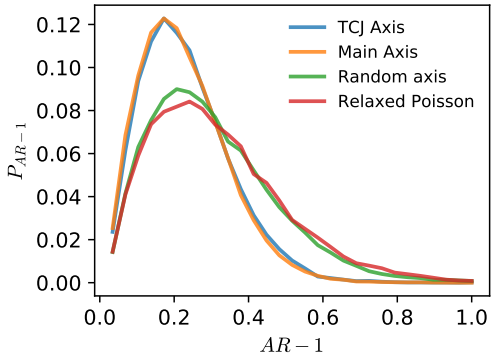

Figure 4.11: Comparison between the distribution of aspect ratio for cells in the tissue under different division rules. The division rules depending on the shape are indistinguishable, comparing their aspect ratio distribution. On the other hand, the random division is indistinguishable from a relaxed Poisson network, and both generate cells on average more elongated than the shape-depending proliferation rules. The simulation used is the same as the one in figure 4.9.

alternative model is one in which the tension of an edge varies with the cell areas. We take the tension in each junction to be given by

$$T(A_a, A_b) = T_0 + k(A_a + A_b - 2A_0), \tag{4.12}$$

where T is the tension in the edge, T_0 a constant tension associated with all edges, and the second term depends on the areas of the cells a and b on the two sides of the junction, A_a and A_b respectively. In this model also, we consider a preferred area A_0. The system is simulated in a box with a fixed size of $\langle A \rangle$, as a change of scale will represent an effective change of T_0. Indeed, this model has only one effective parameter; the force can be normalized in units of $k \langle A \rangle$ and the space in units of $\langle A \rangle$. Defining $\bar{T}_0 = T_0 - 2A_0$, it yields

$$\bar{T}(A_a, A_b) = \bar{T}_0 + A_a + A_b. \tag{4.13}$$

This model is simpler than the variational vertex model, since it has a single parameter to fit, and still it makes physical sense. It offers an alternative to the energy function (2.3).

As in the classic vertex model, noise must be introduced to allow rearrangement. This is done by replacing the constant tension term T_0 by $T_{0,e}(1 + \eta_e(t))$, where $\eta_e(t)$ is a coloured noise independently drawn for each edge e and given by an Ornstein-Uhlenbeck process with characteristic time τ such that $\langle \eta_e(t), \eta_e(t') \rangle = \eta_0 \exp(-|t - t'|/\tau)$.

T1 transition cannot be produced by evaluating a change of energy. Therefore, in simulations of this model, to know if a T1 transition is a favorable move when an edge reaches a length shorter than a threshold, it is tested if the edge increases its length by changing its orientation.

4.5 CONCLUSIONS

The most significant difference between tissues in the soft network parameter region and the region where a hexagonal lattice is the ground state is that in the latter, cells are always convex, and cells with fewer neighbors tend to be smaller. Here, we proposed to use the polygonal class of a cell as an informative category for two critical aspects of its geometry: the cell area and perimeter. This category will be critical for our further analysis. As compared to previous studies, we implemented a division clock and different division rules. In particular, we considered Hertwig's rule based on the position of the vertices of a cell due to the biological evidence of its occurrence in epithelium development [Bosveld et al., 2016b]. We characterized the properties of tissues grown with these different rules. We found, perhaps not surprisingly, that tissues in which cells divide along their main axis have fewer defects and are more ordered.

Finally, we presented a simple vertex model which has neither an energy function nor a cell "pressure", but that produces the main features found in the variational vertex model. It serves as a useful alternative to the classic model, and we will compare results produced by these two models in the following chapter.

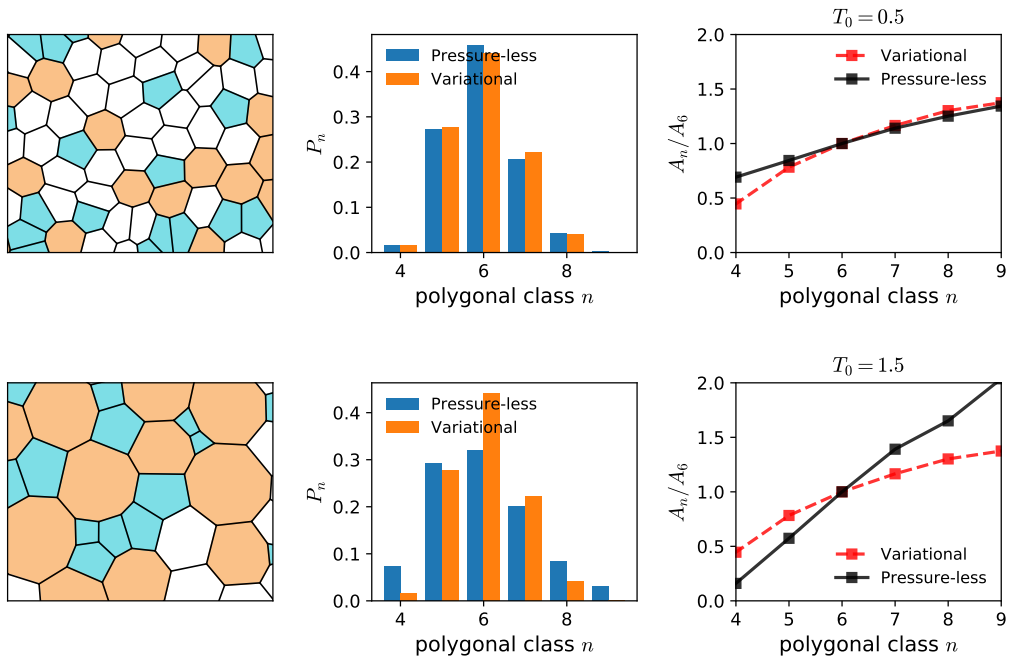

Figure 4.12: **Right:** Example of a proliferative tissue simulated with the pressure-less model. The parameters are $k = A_0 = 1$,and $\eta_0 = 0.1$, for $T_0 = 0.5$ (top) and $T_0 = 1.5$ (bottom). An explicit calculation can be found in chapter 5 in section 5.2.4. Distribution of polygonal classes in the tissue **(Center)** and relative average area for cells of different number of neighbours **(Left)** comparing the pressure-less model and the variational model under the parameters of case A.

5 A MEAN-FIELD APPROXIMATION FOR DISORDERED TISSUE

Biological tissues are, by nature, disordered. In this chapter, we present ways to analytically and numerically characterize disordered epithelial tissues modeled by the vertex model. First, we obtain some exact relations relating mean values and dispersions of cell areas and perimeters. We present a mean-field approximation to describe individual polygonal classes and to describe tissues based on their distribution of polygonal classes. An average n-sided cell is approximated as a regular polygon surrounded by n identical cells that represent a typical cell found in the tissue. We derive an analytical expression for the slope of Lewis' law and predict the bulk modulus of the tissue.

5.1 ANALYTICAL STUDY OF NON-HEXAGONAL TISSUES

Epithelial tissues are clearly geometrically disordered. Vertex model can provide several analytical results for the simplified case of a hexagonal lattice [Murisic et al., 2015]. However, it is not trivial to provide an analytical characterization in the disordered case. In several conditions, we can assume that a solution for the hexagonal lattice can hold in the case of a disordered tissue. As we will show in this chapter, mechanical properties such as the bulk modulus are reasonably well approximated by the value found in a honeycomb lattice. In the vertex model defined by equation (2.3), a cell with area A and perimeter p has an energy

$$\epsilon(A,p) = \frac{1}{2}K\left(A - A_0\right)^2 + \frac{1}{2}(\Gamma p^2 + \Lambda p). \tag{5.1}$$

Thus the energy of a tissue with N cells is entirely determined by the average area A and perimeter p, and the dispersion of those variables, σ_A and σ_p,

$$E(A,p,\sigma_A,\sigma_p) = N\left(\frac{1}{2}K\left[\sigma_A^2 + (A - A_0)^2\right] + \frac{1}{2}\Gamma(p^2 + \sigma_p^2) + \frac{1}{2}\Lambda p\right) \tag{5.2}$$

From this simple formula, it is possible to obtain exact expressions for several properties, even in the case of non-hexagonal tissues, where defects modify the tissue behavior. Considering an affine global change on the area, a pressure P can be defined from equation (5.2) as,

$$P = -\frac{\partial E}{\partial A}_{tot} \tag{5.3}$$

$$= -\frac{1}{2\sum A_c}\left[\sum_c \frac{\partial}{\partial \alpha}\epsilon(\alpha^2 A_c, \alpha p_c)\right]_{\alpha=1} \tag{5.4}$$

$$= -\frac{1}{\sum A_c}\left[\sum_c K A_c(A_c - A_0) + \frac{1}{2}\Gamma p_c^2 + \frac{1}{4}\Lambda p_c\right] \tag{5.5}$$

$$P = K(A_0 - A) - \frac{1}{A}\left[K\sigma_A^2 + \frac{1}{2}\Gamma(p^2 + \sigma_p^2) + \frac{1}{4}\Lambda p\right] \tag{5.6}$$

Although we assume a vanishing external pressure as boundary condition in our simulations, an external pressure P_{ext} can be included in the model by redefining $A_0 \to A_0 - P_{ext}/K$. Or equivalently, keeping normalized parameters $A_0 = K = 1$, the line tension and contractility change as $\Lambda \to \Lambda/(1 - P_{ext})$ and $\Gamma \to \Gamma/(1 - P_{ext})^{3/2}$. Notice that in this case the length units will change. This is relevant, as it allows to easily generalize the results for tissues under an external stress [Bonnet et al., 2012].

5.1.1 *Equilibrium state*

We can recover the average cell area that corresponds to zero pressure from equation (5.6) as function of the normalized perimeter $\mu = p/\sqrt{A}$, and dispersions $\sigma_a = \sigma_A/A$ and $\sigma_\mu = \sigma_p/\sqrt{A}$, where A is the average area. Formally,

$$A_{eq}(\mu, \sigma_a, \sigma_\mu) = \text{root}_A\left\{P(A, \mu\sqrt{A}, \sigma_a A, \sigma_\mu\sqrt{A})\right\} \tag{5.7}$$

An explicit expression for A_{eq} is possible but cumbersome. Regardless, this expression will be used for numerical calculations in future analyses. Alternatively, following the analysis on a hexagonal lattice [Murisic et al., 2015], we can write a compact expression for value for Λ given the area and perimeter averages A and p and dispersions σ_A and σ_p

$$\Lambda + \frac{2}{p}\left[2K\sigma_A^2 + \Gamma\sigma_p^2\right] = -\frac{2A}{p}\left[2K(A - A_0) + \Gamma\frac{p^2}{A}\right]. \tag{5.8}$$

The expression found in [Murisic et al., 2015] for a hexagonal network is recovered by taking $\sigma_A = \sigma_p = 0$ and $p = 2\sqrt{2\sqrt{3}A}$. We can see in a non-hexagonal network that the value of Λ fixing the parameter A is corrected with a term that effectively increases mean contractility. This is expected, considering that the honeycomb is the structure that for a given number of cells and areas to cover, it minimizes the total length. Adding disorder will increase the density of tensile forces. In figure 5.2, we found that for the three sets of parameters of the selected cases, the average area is smaller than the corresponding area in the honeycomb-network case.

The exact amount that the average area per cell decreases due to the disorder of the tissue varies with the way this disorder has been implemented. Different levels of noise

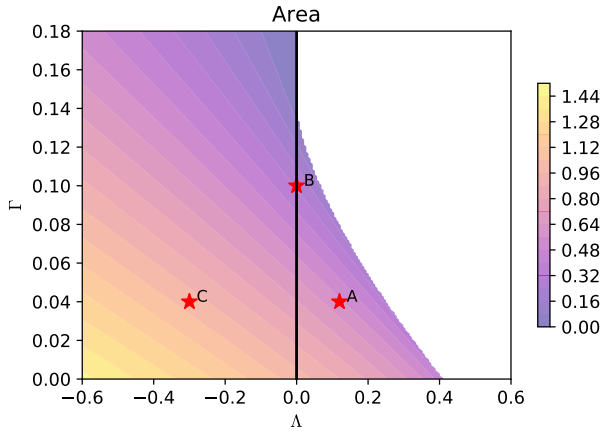

Figure 5.1: Countour plot of the equilibrium areas for regular hexagons obtained by minimizing the energy function (2.3) under different values of Γ and Λ. In the white area there is no solution. The stars point to the cases that will be used as representative of different packing in the vertex model.

and proliferation rules will produce more ordered or disordered tissue. In chapter 4, we included a discussion about how diverse proliferation methods affect the disorder in the system.

5.1.2 *bulk modulus*

One of the key characterizations we can make of the tissue is the bulk modulus. Defined as the ratio of the infinitesimal pressure increase to the resulting relative decrease of the volume—or the area in a system constrained to two dimensions like ours—it is a measure of the opposition to compression of a medium. First, we can define a simplified version of the bulk modulus by evaluating changes in the pressure deriving equation (5.6), considering an affine rescaling of the tissue.

$$B_{aff} = -A_{tot} \frac{dP}{dA_{tot}}\Big|_{A_{tot}^{eq}} \tag{5.9}$$

Here, A_{tot} refers to the total area of the tissue, defined as the sum of the area of all its cells, and A_{tot}^{eq} is the total area that minimizes the energy function (2.3). Subsequently, computing the derivative and evaluating in Λ_0, yield,

$$B_{aff} = \frac{1}{2A}\left[A(3A - A_0)K + \frac{\Gamma}{2}\left(p^2 + \sigma_p^2\right) + 3\sigma_A^2 K\right] \tag{5.10}$$

Where B_{aff} is an affine bulk modulus, i.e. the bulk modulus related to the work done to change the tissue scale where all cells are rescaling by the same factor. The affine

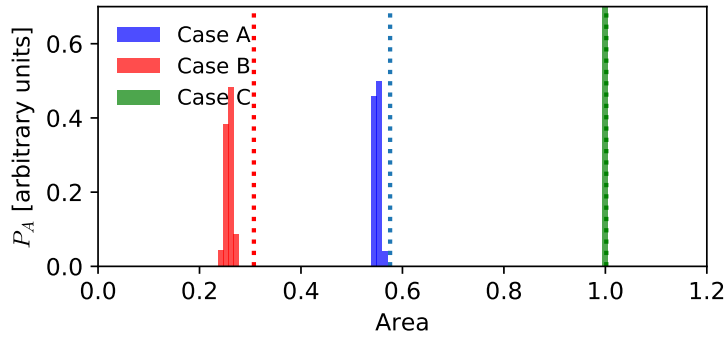

Figure 5.2: Comparison between hexagonal equilibrium area (dotted lines) and distribution of average area among different realizations of proliferative tissues with 60 cells, after allowing the tissue to relax to its optimal scale. The initial state had 15 cells. In case A, parameters are $\Lambda = 0.12$ and $\Gamma = 0.04$; in case B, parameters are $\Lambda = 0$ and $\Gamma = 0.1$; and in case C, parameters are $\Lambda = -0.32$ and $\Gamma = 0.04$. In all cases, disorder decreases the equilibrium area per cell, an effect that holds for all the parameters as result of equation (5.8).

bulk modulus must be higher than the real one, as a consequence of the relaxation of additional degrees of freedom.

Equation (5.10) accounts for an affine transformation of the tissue. In a heterogeneous tissue, not all the cells will respond in the same way under a change in scale. This is shown in Figure 5.3, where the affine approximation is compared with the true bulk modulus obtained by varying the scale of the tissue and allowing its relaxation. This produces a bulk modulus that is smaller than the affine one, even if by a small amount. To evaluate cell actual change of energy by imposing a rescaling of a disordered tissue, we have no option but to run a simulation where this rescaling is imposed by successive steps, multiplying distances by a factor α, and to relax. From the variation of energy after different values of α in the tissue, we can obtain the real bulk modulus. The bulk modulus is defined around the equilibrium, and a non-linear effect will manifest under a big compression or expansion. Therefore, we consider a maximum of α of 3%. Note that the distance to the hexagonal case and the differences between the affine bulk modulus and the one found by relaxing the tissue at different scales will vary with the level and type of disorder in the tissue.

The expressions found so far are analytical and exact. However, they do not allow us to go much further. In the next section, a more general method will be presented.

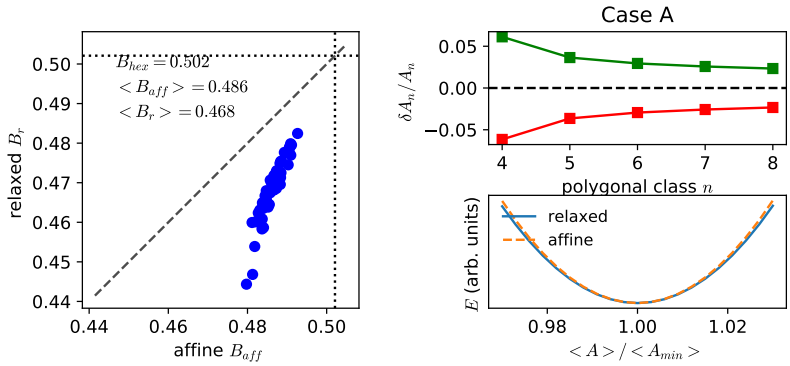

Figure 5.3: **Left**: Scatter plot of the values of the bulk modulus obtained for tissues with 60 cells under the parameters of case A. B_{aff} is the affine bulk modulus obtained using equation (5.10), and B_r the bulk modulus obtained by fitting a parabola $E_p(A) = (B_r/2)(A/A_{eq} - 1)^2 + E_0$ to the energy as the area changes continuously between plus and minus 3% its optimal size. The vertical and horizontal lines show the value of the bulk modulus for a hexagonal network B_{hex}, and the diagonal line is the identity. The bulk modulus is dispersed. However, it held that for this set of parameters $B_{hex} > B_{aff} > B_r$. The **top right** panel shows the relative average change of area for cells of different numbers of sides when the tissue is 3% bigger (green) or smaller (red). The response is stronger in cells with fewer neighbors. The **bottom right** panel show the energy landscape as a function of the change of the average area.

5.2 MEAN-FIELD APPROXIMATION

The methods and approaches presented before can describe meso and macroscopic features of disordered tissues as the bulk modulus and effective equilibrium area. However, they cannot provide much insight into several features of individual cells. For instance, is it possible to theoretically predict the expected area of a cell if its number of sides is known? The variation of the area with the number of sides is a key feature used to adjust the parameters in the vertex model [Farhadifar et al., 2007], and gives important information about the geometry of the tissue. In general, this approach can allow us to characterize the vertex model under different parameters and address the interaction between groups of cells with different mechanical properties, observing the effect at the interface between them.

5.2.1 *Individual cells*

The shape of a cell in a tissue depends not only on its mechanical properties but also on its neighboring cells. For instance, the cell apical area, depends on the number of neighbors, as stated by Lewis' law. A simple possible way to characterize the tissue could be to characterize each cell in isolation. Optimizing cell area, constraining the cell shape to a polygon, under the energy function (5.1) leads to a small difference in area between different polygonal classes compared with the actual observed Lewis' law, as we can see in figure 5.4. The different sizes among different polygonal classes originate from the fact that cells with fewer neighbors are subjected to less outward forces. Besides the hexagonal lattice, we need to include the exterior forces of the cell.

Fortunately, we only need to include the mean approximation of the adjacent cell to recover Lewis' law. In such *mean-field* approximation, an average cell of n sides is described by a simple system where a regular n-sided polygon is surrounded by n equal cells with the average area A_r, as it is represented in figure 5.5. In a first approach, we will use the predicted area for a hexagonal lattice (that is the same than one hexagonal cell in isolation) without considering the dispersion of the network; nonetheless, the expected area for a disordered tissue is smaller as it was shown in figure 5.2. However, we will see that the effect on the prediction of the relative behavior between cells with different numbers of sides is negligible.

Symmetry will impose that each edge and vertex is equivalent, and the force in the direction perpendicular to the arriving edge will be trivially zero and in the parallel direction will be given by,

$$F(A, n; A_r) = 2T_r - 2\sin\left(\frac{\pi}{n}\right)\left[T_r + T_n(A)\right] - \frac{\mu_n}{n}\sqrt{A}\cos\left(\frac{\pi}{n}\right)K(A - A_r) \tag{5.11}$$

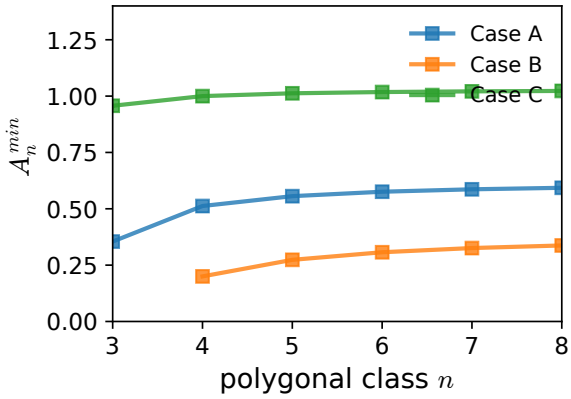

Figure 5.4: Optimal area for an isolated (or equivalently, if possible, a tessellation of identical polygons) n-sided cell (shaped as a regular polygon) for a different set of parameters. The area A_n^{min} is obtained by minimizing the energy function (5.1) for one single cell of perimeter $\mu_n \sqrt{A_n^{min}}$ where μ_n is the perimeter of a regular polygon of n sides with unitary area. The calculation yields a positive slope as the number of neighbors increases. However, the effect is far below the trend found in simulations and experimental data. There is no stable 3-sided cell for case B.

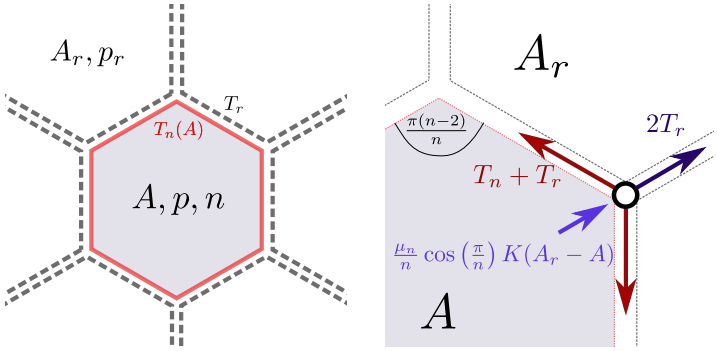

Figure 5.5: **Left:** Scheme of the mean-field approximation. Edges are explicitly represented as two opposed cortices, with a total tension equal to the sum of the contribution of each side. Surrounding cells mimic an average environment. They are assigned with fixed geometry and mechanical parameters that correspond to the values found in an average cell. **Right:** Diagram of forces over the vertices of a cell under our mean-field approximation.

where μ_n is the perimeter for a cell of n sides and unit area. T_n is the tension contribution from one cell,

$$\mu_n = 2\sqrt{n\tan\left(\frac{\pi}{n}\right)} \tag{5.12}$$

$$T_n(A) = \Gamma\mu_n\sqrt{A} + \frac{1}{2}\Lambda \tag{5.13}$$

$$T_r = \Gamma p_r + \frac{1}{2}\Lambda \tag{5.14}$$

$$\tag{5.15}$$

Here, p_r is the perimeter of a neighboring cell. The model receives input from the parameter of an average configuration (area A_r and perimeter p_r), and imposing $F(A, n; A_r) = 0$, we calculate the mean size of a n-sided cell embedded in the tissue. This result will be very useful in many analyses during this work. This straightforward model is in good agreement with simulations under a different set of parameters, as shown in Figure 5.6. In this case, we supposed the area and perimeter of adjacent cells to be minimal for the energy (5.1) in the case of an hexagonal cell, that is $A_r = A_6^{min}$ and $p_r = \mu_6\sqrt{A_6^{min}}$ where A_6^{min} is the optimal area. Later on, this analysis will be refined to predict the dispersion as well.

The agreement is remarkably good, especially in the case of polygonal classes 5,6 and 7. As deviation for cells with fewer or more edges is to be expected given Aboav's law, since the average environment where a four or eight-sided cell is embedded is biased towards cells that are not the average cell. It is conceivable to extend the present approximation to include such correlations between neighboring cells.

Since cells are approximated as regular polygons, the present approach cannot capture the geometry of the tissue in case C, and in general, in the soft-network region.

Lewis' law slope

The exact expression for A_n is not linear and the solution of a transcendental equation. Nevertheless, we can approximate the factor λ by deriving an equation with respect to n equation (5.11) to obtain $\frac{dA}{dn}$. Evaluating that expression for $A = A_6$ and $n = 6$, assuming that $\langle A\rangle = A_6$,

$$\lambda = \frac{1}{A_6}\frac{dA}{dn}\Big|_{n=6} = \frac{\pi}{\sqrt{3}A_6\mu_6}\frac{2A_6\Gamma\mu_6 + \sqrt{A_6}\Lambda}{\sqrt{3}A_6k + 6\Gamma}. \tag{5.16}$$

We note that equation (5.16) allows for external stress to be applied to the tissue, through the value of A_6. Alternatively, if the goal is to obtain parameters Λ, Γ, K and A_6 to model empirical data from where λ has been measured,

$$\Lambda = -\frac{\mu_6}{\pi\sqrt{A_6}}\left[3(A_6K + 2\sqrt{3}\Gamma)\lambda - 2\pi A_6\Gamma\right]. \tag{5.17}$$

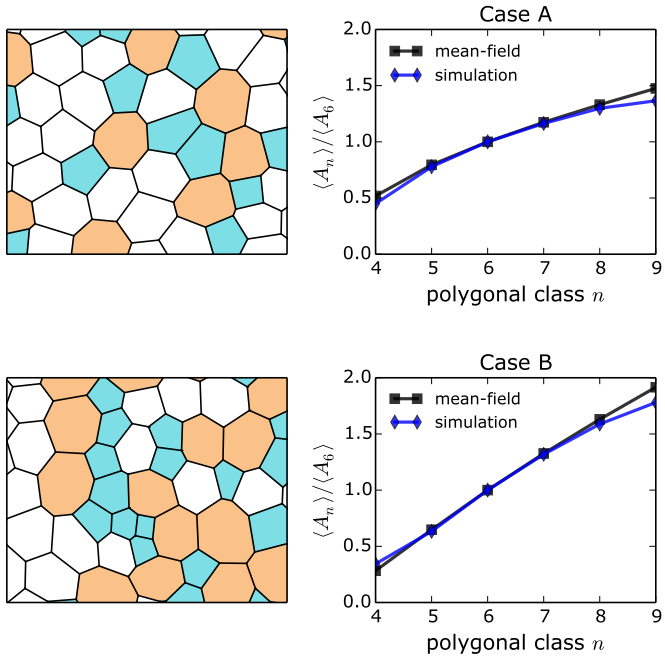

Figure 5.6: Lewis's law in silico (blue bars) and deduced by a mean-field analysis (black line). **Right:** Examples of proliferative tissues for different parameters. Cells with more/fewer than six sides are marked red/blue. Six-sided cells are white. **Left:** Comparison between average area for cells of different number of sides, normalized by the size of six-sided cells. **Top:** Case A where parameters are $\Lambda = 0.12$ and $\Gamma = 0.04$ **Bottom:** Case B where parameters are $\Lambda = 0$ and $\Gamma = 0.1$. In both cases, the value for an regular cell is the solution for a hexagon in isolation, $A_r = A_6^{min}$ and $p_r = \mu_6 \sqrt{A_6^{min}}$.

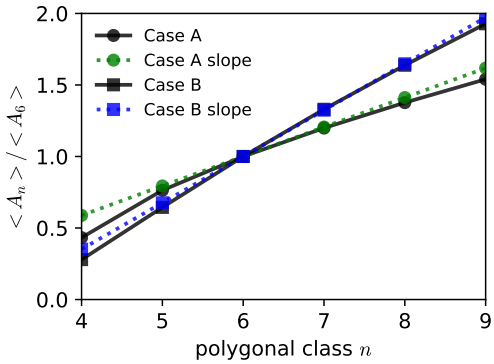

Figure 5.7: Slope of Lewis' law in case A (in green) and B (in blue). The thick black lines are the relative size by polygonal class for each of those cases obtained as root of equation (5.11). The dotted line corresponds to the line $y = 1 + \lambda(n-6)$, where λ is given by equation (5.16).

In figure 5.8, the variation of the Lewis' slope is shown in a contour plot for different parameters. As Lewis' law becomes stronger and we increase the value of Λ and Γ, the expected difference among the area of polygonal classes becomes bigger.

5.2.2 *Area and perimeter dispersion*

We have shown that the dispersion in cell areas and perimeters determines how the mean area will differ from the hexagonal case in equilibrium by using the expression (5.7). Yet, the use of this expression requires knowing the relative dispersions of cell area and perimeter. These values can be obtained from simulations, or alternatively, here we present how using Lewis' law and the distribution P_n of polygonal classes, we can obtain a good prediction of the dispersion in the area (see table 5.1).

For an hexagonal lattice the equilibrium area A for its cells is given by optimizing equation (5.1) considering a cell with perimeter $p = \mu_6\sqrt{A}$ (values shown in for case A and B in the column hex in table 5.1). We can use those values as the area and perimeter for surrounding cells in equation (5.11), and obtain a first prediction for the area A_n for each polygonal class. Now, we can predict an average area $\langle A \rangle = \sum_n A_n P_n$ and the dispersion as,

$$\sigma_A^2 = \sum_n A_n^2 P_n - \langle A \rangle^2 . \tag{5.18}$$

Similarly, a prediction for the average cell perimeter can be obtained assuming the cells are regular polygons $\langle p \rangle = \sum_n \sqrt{A_n}\mu_n P_n$, and the dispersion analogously $\sigma_p^2 = \sum_n A_n \mu_n^2 P_n - \langle p \rangle^2$. Now that we have the average and dispersion for the area and

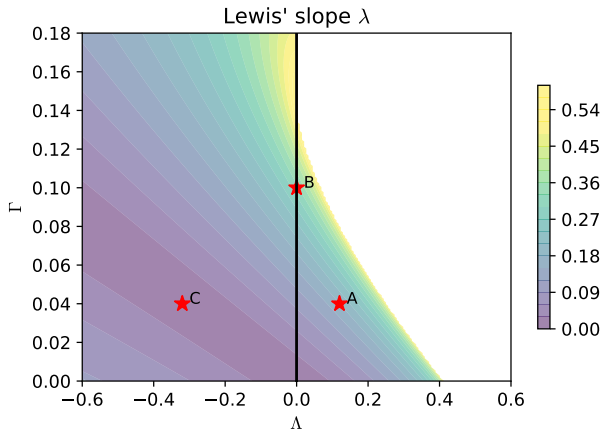

Figure 5.8: Contour plot for Lewis' law slope for different values of Λ and Γ predicted by equation (5.16). In the white region there are no stable solutions.

perimeter, we impose zero-pressure using equation (5.7) that provides an equilibrium area $A = A_{eq}(\langle p \rangle, \sigma_A / \langle A \rangle, \sigma_p / \sqrt{\langle A \rangle})$, that rescales the perimeter $p = \langle p \rangle \sqrt{A' / \langle A \rangle}$ and dispersions analogously. The values obtained by this procedure are shown in table 5.1 in the column mfhex, and a scheme is presented in figure 5.9.

This procedure can be repeated coming back to equation (5.11) but using the updated value of A as input for the mean-field calculation. The result after the first iteration is shown in table 5.1 in the column mf, and the result after succesive self-consistent repetitions in the column mf s.c..

Those two equations are valid when the area is well predicted by the number of neighbors. As the Lewis' law slope λ becomes small, cells with different numbers of sides are not significantly different in average. Therefore, the main source of the area and perimeter dispersion comes from variations in cell shape, e.g. anisotropy. In case C, and in general the soft-network region, we cannot be captured by our mean-field analysis, and in particular, we cannot predict the dispersion (we would trivially predict zero-dispersion as all the polygon types have the same mean area).

Going one step further, it would be possible to use the distribution of polygonal classes deduced in [Gibson et al., 2006] and predict the cell and perimeter dispersion purely from theory. However, the very simple treatment in that reference cannot capture the changes in the distribution with different vertex model parameters, and we prefer to use the empirical distributions obtained from our simulations. Doing so also ensures that deviations between simulations and theory are originated by variations in cell shape. We run an iterative process, starting with A_r equal to cell area of equilibrium for an hexagonal lattice, and we predict values for $\langle A \rangle$, $\langle p \rangle$,σ_A^2 and σ_p^2 that we use to obtain a new A_r by optimizing the area for equation under equation (5.7), to then be injected

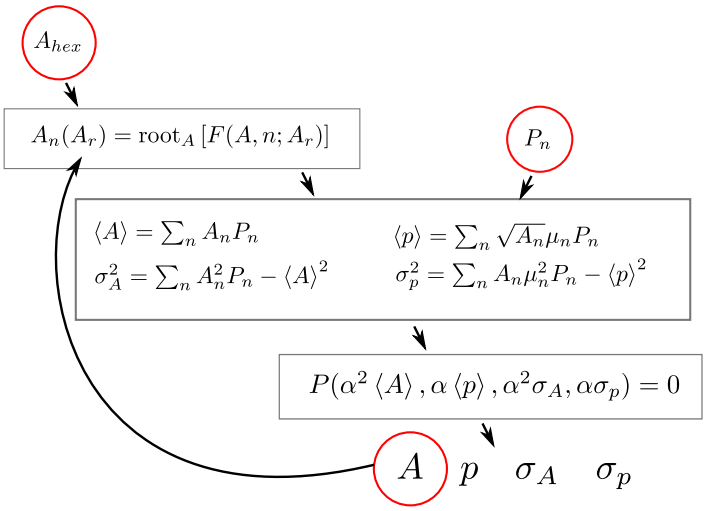

Figure 5.9: Scheme of the method to find the average area and dispersion given a distribution of polygonal classes P_n.

Case A	sim	hex	mfhex	mf	mf s.c.
Area A	0.549	0.576	0.558	0.557	0.557
Perimeter p	2.788	2.824	2.777	2.774	2.773
Disp. Area σ_A	0.088	-	0.092	0.094	0.095
Disp. Perim. σ_p	0.199	-	0.19	0.197	0.198
Case B	sim	hex	mfhex	mf	mf x10
Area A	0.263	0.307	0.282	0.281	0.28
Perimeter p	1.904	2.063	1.954	1.949	1.945
Disp. Area σ_A	0.088	-	0.087	0.089	0.09
Disp. Perim. σ_p	0.309	-	0.284	0.291	0.295

Table 5.1: Mean-field predicts average area, perimeter and dispersions for tissues *in-silico*, for case A and B. The columns have the numerical values found in the simulation, and the rows, different parts of the statistic for area and perimeter. **sim** column is the result obtained in simulations; **hex** the values for an hexagonal lattice; **mfhex** the computation obtained as a result of considering $A_r = A_{hex}$; **mf** refines the calculation considering for A_r the output of the mfhex proccess; **mf s.c.** repeats the process self-consistently until values do not change. The values for the distribution of polygonal classes for each case are given in the table 4.1.

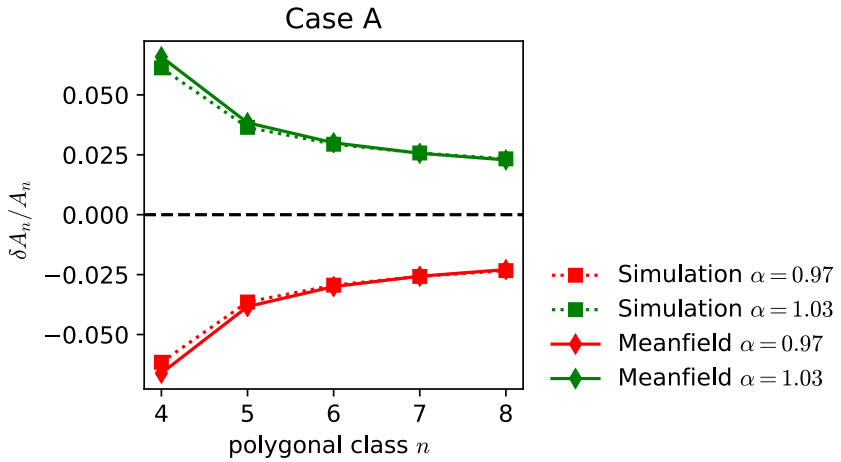

Figure 5.10: Mean-field approximation can predict the relative change in area $\delta A_n / A_n$ of dissimilar polygonal classes. Simulation with parameters of case A.

back in the mean-field equation (5.11) for each polygonal class, and repeat until we get stable values. In the table 5.1 we put the values obtained using this procedure, that is remarkably good in the aim to predict the equilibrium average equilibrium area, without running any simulation.

5.2.3 *Bulk modulus from mean-field approximation*

Let us return to the figure 5.3, where we analyze the dissimilarities between the affine bulk modulus, and the one obtained by relaxing a tissue varying the pressure. First of all, the relative change in the area after imposing a rescaling of the tissue can be well recovered using the mean-field approximation. If an average cell in the tissue has an area $\langle A \rangle$, we can compute the response in various polygonal classes using equation (5.11) when increasing the total area by a factor α, considering that the area of surrounding cells increases with the same factor $A_r = \alpha \langle A \rangle$. Diverse polygonal classes will change following

$$A_n(\alpha) = \text{root}_A \{F(A, n; \alpha A_r)\} \tag{5.19}$$

Here, $F(A, n; \alpha A_r)$ is the force over each vertex of a n-sided cell of area A when is surrounded by cells with area A_r defined in equation (5.11).

	hexagonal	simulation B_r	affine B_{aff}	mf correction B_{mf}
Case A	0.502	0.474	0.484	0.476
Case B	0.307	0.280	0.297	0.283
Case C	1.166	1.017	1.159	-

Table 5.2: Bulk modulus for a tissue for case A and B. Mean-field predicts area and dispersion for tissues in-silico. The numerical values for the mean area found in the simulation $\bar{A}$, the average found in the mean-field approximation $\langle A \rangle$, the relative error on the three representative cases, as well as the dispersion σ_A for both simulation and mean-field approximation, for cases A and B. Case C correspond to the soft-network and our mean-field approximation is not meaningful for the system.

The variation of energy of the tissue can be broken down into the variation under an affine rescaling.

$$E_{aff} = \frac{1}{2} A_{eq} B_{aff} (\alpha - 1)^2, \tag{5.20}$$

plus the energy drop associated with the non-affine deformations of cells in the various polygonal classes. The work $W_n(\alpha)$ to take a n-sided cell from $\alpha A_n(1)$ to $A_n(\alpha)$ can be calculated as the integral of force over the displacement of its vertices,

$$\begin{aligned} W_n(\alpha) &= n \int_{\alpha A_n(1)}^{A_n(\alpha)} F(A, n; \alpha A_r) \frac{dR}{dA} dA & (5.21) \\ &= n R_n \int_{\alpha A_n(1)}^{A_n(\alpha)} F(A, n; \alpha A_r) \frac{1}{2\sqrt{A}} dA. & (5.22) \end{aligned}$$

Here, R_n is the radius of a n-sided regular polygon, given by the expression,

$$R_n = \frac{\mu_n}{2n} \left[\sin \frac{\pi}{n} \right]^{-1}. \tag{5.23}$$

For α close to 1, $F(A, n; \alpha A_r)$ varies linearly around its equilibrium, and we get

$$W_n(\alpha) = \frac{1}{2} n R_n \left(\sqrt{A_n(\alpha)} - \sqrt{\alpha A_n(1)} \right) F(\alpha A_n(1), n; \alpha A_r) \tag{5.24}$$

The total energy per cell can be calculated as,

$$E_{mf}(r) = E_{aff} + \sum_n P_n W_n(\alpha) \tag{5.25}$$

Using the empirical distribution P_n found in the simulations and adjusting the energy $E_{mf}(\alpha)$, we can predict the bulk modulus with precision above 1%.

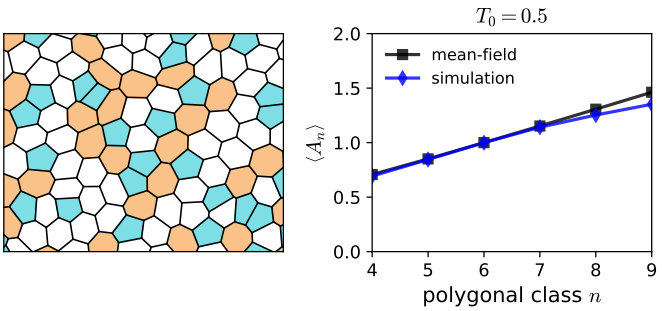

Figure 5.11: Lewis's law in silico (blue bars) and deduced by a mean-field given by equation(5.28) (black line). **Right:** Examples of proliferative tissues for pressure-less model with T_0. Cells with more/fewer than six sides are marked orange/cyan. Six-sided cells are white. **Left:** Comparison between average area for cells of different number of sides, normalized by the size of six sided cells.

5.2.4 *Pressure-less model*

.

The same previous analysis can be done in a pressure-less model, pressented in 4.4, now considering no pressure and a different function for the tension in equation (5.11),

$$F(A) = T(A_r, A_r) + 2\cos\left(\frac{\pi}{n}\right) T(A_r, A), \tag{5.26}$$

where A_r is the average area of the cells in the tissue; but in this case as the size of the box is fixed, we can chose $A_r = 1$. Therefore,

$$T(A_a, A_b) = T_0 + A_a + A_b - 2. \tag{5.27}$$

The solution for $F(A) = 0$ in this case is more compact than the usual vertex model,

$$A_n = T_0 \left(\left[\sin\left(\frac{\pi}{n}\right) \right]^{-1} - 2 \right) + 1. \tag{5.28}$$

The Lewis' law slope λ has an exact and simple expression where λ is exactly proportional to the tension T_0,

$$\lambda_n = \left.\frac{dA}{dn}\right|_n = \frac{\pi}{2n^2} \frac{\cos\left(\frac{\pi}{n}\right)}{\sin^2\left(\frac{\pi}{n}\right)} T_0, \tag{5.29}$$

and in particular, $\lambda_6 = T_0 \pi / \left(12\sqrt{3}\right)$.

5.3 CONCLUSIONS

Epithelia modeled as regular hexagonal lattices provide a good first approximation. But to go further, the disorder must be taken into account. Our mean-field approximation allows us to address disordered tissues by characterizing average features for cells of different polygonal classes. Many features and statistics of a disordered tissue can be obtained by combining and averaging over different polygonal classes with the right proportion. Here, we have shown how the dispersion in areas and perimeters can be predicted by combining the predicted Lewis' law and the distribution of polygonal classes. As well, we show that the optimal scale for a tissue under the vertex model can be obtained only depending on cell area and perimeter mean and dispersion, and derived from the same analysis; we derive a simplified bulk modulus.

Experimentally and in-silico cells are often elongated, and having an aspect ratio different from the unit is a universal feature [Atia et al., 2018]. Ignoring this anisotropy is an obvious limitation of the mean-field approach presented here, although of limited consequences in the parameter regimes that are proposed to describe *Drosophila* epithelia. On the other hand, this approach does not extend to the soft-network regime since cells in this regime are far from being regular polygons, and the number of sides of a cell tells us little about their size and perimeter.

We have also noted that our mean-field approximation could be tweaked to refine its predictions or cover more diverse situations. For instance, to capture that the mean neighborhood varies depending on the polygonal class of a cell, by changing the mean area and perimeter according to the number of sides of the cell considered, as stated by Aboav's law. Or, as we will present in chapter 6, allowing for non-uniform mechanical parameters.

6 CLONE INCLUSION

In this chapter, we study the interaction between cells with different mechanical parameters under the light of mean-field approximations—introduced in the previous chapter—and topology. First, we study the effect of diverse mechanical parameters in the vertex model for isolated cells. The effect of differences in proliferation rate, and how they affect the local topology is also examinated. After this analysis of isolated cells, we tackle the problem of a group of cells. We studied the effect of a cable of tension surrounding a cluster of cells. We propose effective Laplace's law for this discrete system and present general properties on the topology of these clusters embedded in a tissue. Finally, we integrated all those ingredients to study the effect of a superficial tension on a cluster of cells.

6.1 ISOLATED CELL WITH DIFFERENT PARAMETERS

6.1.1 *Isolated cell with different mechanical properties*

The simplest example of a tissue with mechanical heterogeneity is an isolated cell that differs in its parameters from its environment. Our mean-field approach suits the problem perfectly, considering an isolated cell with a particular value of prefered area A_0^c, line tension Λ_c, or perimeter elasticity Γ_c, leads to the same equation (5.11) as before, but the tension $T_n(A)$ and difference of pressure ΔP_n associated with the cell are now given by

$$T_n(A) = \Gamma_c \mu_n \sqrt{A} + \frac{1}{2}\Lambda_c, \tag{6.1}$$

$$\Delta P_n = K\left[(A - A_0^c) - (A_r - A_0)\right]. \tag{6.2}$$

The resulting dependency of the area A on the parameters is illustrated in figure (6.1), showing as expected, that increases with the preferred area A_0^c, and it decreases with the tension. For a given number of sides n, multiple combinations of parameters produce the same area. These satisfy a simple linear relation,

$$\Lambda_c = -2T_r\left[\csc\left(\frac{\pi}{n}\right) + 1\right] - 2\Gamma_c\mu_n\sqrt{A} + \frac{\mu_n}{n}\sqrt{A}\,\operatorname{cotg}\left(\frac{\pi}{n}\right)\Delta P_n, \tag{6.3}$$

which expressed in this form gives the change in Λ_c to keep the same area when the other two parameters are varied. Nevertheless, the above analysis does not account for the fact that bigger cells are expected to have more neighbors than smaller cells.

Also, the fact that there are redundant changes of parameters that produce the same change in the cell area will limit our ability to infer mechanical parameters from experimental data (cf. chapter 7).

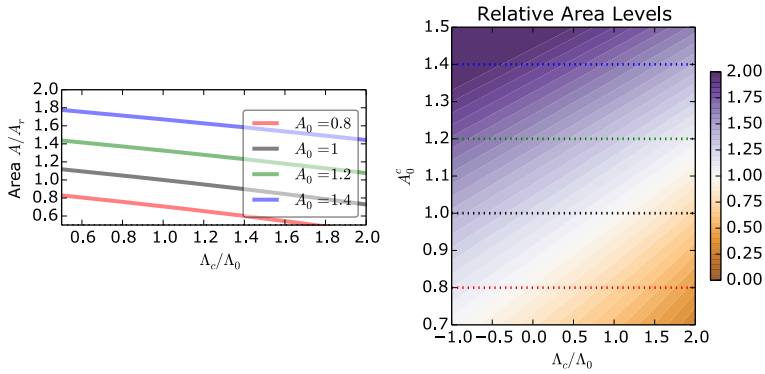

Figure 6.1: **Right:** Equilibrium area of a 6-sided cell under the function of the value of Λ_c for different preferred areas. **Left:** Contour plot of the variation of the area relative to the area of a normal cell under those parameters. All the plots for Case A $\Lambda = 0.12$ and $\Gamma = 0.04$.

6.1.2 *Non-proliferative cell*

Besides their different mechanical properties, cells may also differ from their environment by their rate of proliferation. As we show in chapter 4, the main element driving geometry is mechanical forces, but differences in proliferation also influence the geometry of tissue, more clearly in the extreme case, considered here, of a non-proliferative cell in a proliferating tissue.

After a cell divides, the two daughters have equal or fewer neighbors, while two of their neighbors gain an edge. Non-proliferative cells will constantly gain sides from the division of their neighbors. Without division to reduce their number of sides, only neighbor exchanges keep the cells from gaining neighbors indefinitely. A simple model to describe the process reads,

$$\frac{ds}{dt} = \frac{r_{div}}{3} s - r_{T1}(s-6), \tag{6.4}$$

where s is the number of sides of the non-proliferative cell, r_{div} the rate of proliferation for the surrounding cells, and the factor $1/3$ assumes that surrounding cells are 6-sided and that in each division two sides at random are picked to create a new junction (factor that can be changed if one of those hypothesis is false). r_{T1} is the rate at which non 6-sided cells undergo a T1 transition. This equation, with the initial condition $s(t=0) = 6$, has the simple solution

$$s(t) = 6\frac{3r_{T1}}{3r_{T1} - r_{div}}\left[1 - \frac{r_{div}}{3r_{T1}} \exp\left[-\left(r_{T1} - \frac{r_{div}}{3}\right)t\right]\right]. \tag{6.5}$$

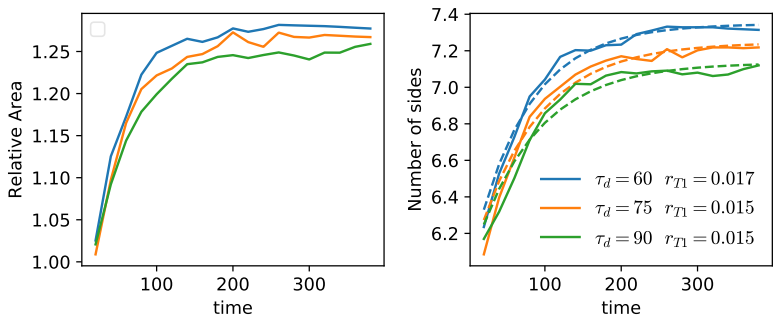

Figure 6.2: Temporal evolution of expected area **(left)** and number of sides **(right)** for a non-proliferative cell embedded in a proliferative tissue. As the cell gains neighbors, its area increases until it reaches a steady-state. Three values for the mean division time τ have been tested. The dashed lines correspond to the fit of equation (6.5), considering $r_{div} = 0.703/\tau_d$, as this is the effective growth rate (see 4.1). The simulations were run with the parameters of Case A. After relaxing the tissue from a Poissonian distribution, a cell is chosen at random as non-proliferative, and during 400 units of time, the tissue around proliferates.

This dynamics simplifies the problem and assumes uncorrelated times for cell divisions. In our simulations, this model captures well the dynamics observed for isolated non-proliferative cells, as shown in figure 6.2. The rate r_{T1} cannot be directly measured, and it is a function of r_{div}, since faster proliferation increases the tissue disorder, which induces more T1 transitions.

Cells that do not proliferate are slightly bigger on average, even compared to regular cells of the same polygonal class, as shown in figure (6.3). Their distribution in polygonal classes is different from the distribution of proliferative cells. They have an average number of sides that increases as the proliferation rates increases.

6.2 CLUSTER OF CELLS

6.2.1 *Compressed isolated cluster*

The bulk modulus analysis presented in chapter 5 was performed by a system where the pressure is applied homogeneously in space. When forces are applied over a bounded cluster, the deformations maybe even more non-uniform, especially if the pressure is applied with a tension cable. To well appreciate this, figure 6.4 shows the effect of increasing the line tension Λ_s in the frontier of a cluster of hexagonal cells with different numbers of cells. Most cells change their size but keep their hexagonal shape, except cells in the boundary, which undergo stronger changes in shape than cells in the interior.

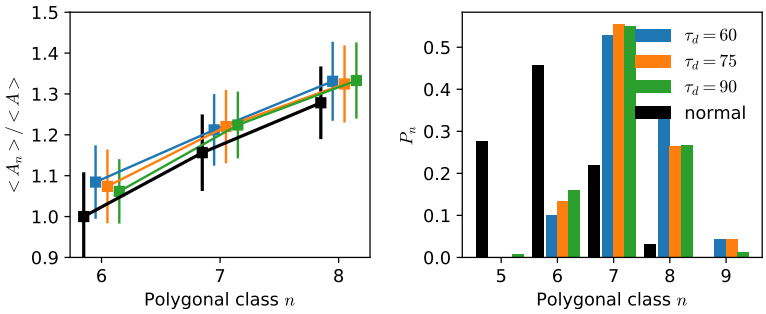

Figure 6.3: **Left:** Relative area for different polygonal classes with standard deviation as error bar (the small offset is for clarity). **Right:** Histogram of polygonal classes. For both graphs, the average for regular cells in the tissue is shown in black. In colors, the cases of non-proliferative case embedded in a tisssue that proliferates with mean division time τ_d. These statistics are from the same simulations than figure 6.2.

Clusters eventually collapse as the value of Λ_s increases. Bigger clusters resist bigger tensions.

6.2.2 *A Laplace's law for a discrete system*

Laplace's law, also called Young-Laplace law, relates the pressure difference between the two sides of a continuous surface to its shape. In two dimensions, a surface with tension T facing a change of pressure ΔP, will locally deform with a curvature R following a simple equation,

$$\Delta P = \frac{T}{R}. \tag{6.6}$$

How this simple continuous law applies to a discrete system is not straightforward. The work done by the boundary is proportional to its length. The question is how to coarse-grain to express force balance at the tissue scale, as an apparent paradox emerges: an irregular surface should induce a bigger drop in energy if an extra tension is applied, given that the perimeter of the cluster is bigger and the tensile energy proportional to it.

We can break down the energy change around the equilibrium area A_{eq} and perimeter L_{eq} induced by a surface tension δT into: *i)* an energy associated with affine changes in area, accounted by a harmonic potential for the area A around its equilibrium A_{eq} with its constant proportional to the bulk modulus B, *ii)* a term proportional to the length and excess of surface tension, obtained by simply multiplying the length of the border L.

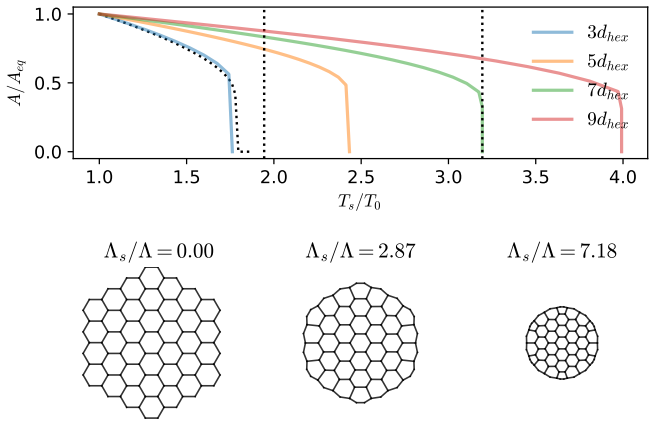

Figure 6.4: **Top:** Relative average cell area versus relative tension on the boundary for different cluster sizes. Area and tension are normalized by their values before adding the cable. **Bottom:** Example of the cluster geometry for different boundary tensions in the cable for the case of diameter $7d_{hex}$. The vertical lines in the top panel correspond to the tension levels shown in the bottom panel.

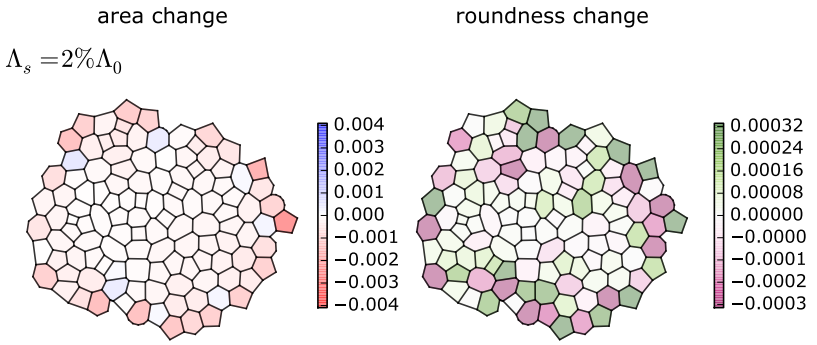

Figure 6.5: Relative change in the area (left) and roundness (right) for individual cells in an example of cluster comparing before and after relaxing with a cable of tension $\Lambda_s = 2\%\Lambda_0 = 0.024$ in the edges of the boundary. The change of area, calculated as the ratio between the area difference and the original area, is stronger in cells near the border. The change of roundness, defined as the ratio between the roundness difference and the original roundness.

Where we have used L that the perimeter L is a function of the area A. The total energy of the system reads,

$$E_{lap} = \frac{BA_{eq}}{2}\left(1 - \frac{A}{A_{eq}}\right)^2 + L(A)\delta T + E_0. \tag{6.7}$$

We can approximate $L(A)$ as the perimeter rescaled to the new clone size. Here, it is convenient to define the roundness of a cluster with area A and perimeter L as $\rho = 4\pi\frac{A}{L^2}$, which measures how circular it is (in a circle $\rho = 1$ and in line $\rho = 0$). Defining as well the effective radius $R_{eff} = \sqrt{A/\pi}$ as the radius of a circle with the same area than the cluster A, the perimeter is given by $L(A) = 2\pi\sqrt{\rho}R_{eff}(A)$. The minimum of equation (6.7) satisfies,

$$\Delta P = B\left(\frac{A}{A_{eq}} - 1\right) = \frac{dL}{dA}\delta T = \frac{\delta T}{\sqrt{\rho}R_{eff}(A)}. \tag{6.8}$$

Equation 6.8 predicts the change of area in a cluster of cells induced by a superficial tension (see figure 6.6). We recover the continuous Laplace's law (6.6) in the limit of $\rho = 1$. However, the change in area is not uniform, and cells exhibit bigger changes in area and shape near the boundary, as shown in figure 6.5. The change of the area of cells in the interior far from the clone boundary is better predicted by a smooth perimeter, corresponding to the perimeter of a circle that has the same area as the cluster $L = 2\sqrt{\pi A}$. Substituting in (6.7) and minimizing for A yields,

$$B\left(\frac{A}{A_{eq}} - 1\right) = \frac{\delta T}{R_{eff}(A)}, \tag{6.9}$$

where we defined the effective radius. This suggests that the cells in the interior of the cluster do not sense the details of the geometry of the surface of the cluster; instead, they only sense a homogeneous force similar to a pressure applied over a smoothed surface. In figure 6.6 those two predictions provided by equation (6.8) and (6.9) are compared.

6.2.3 *Geometrical relations between interior and outward angles*

In the vertex model, a cluster of cells defines a closed curve formed by discrete edges. A general property in a polygon is that external angles must add up to 2π radians (see figure 6.7). As we are interested in studying clusters with mechanical differences with their environment, there are two relevant categories of angles: internal (or convex) angles and outward (or concave) angles. If tensions in the interior of the clone are big, outward angles will tend to be smaller than internal, and if tensions in the boundary are big, then both types of angles will straighten. With this distinction, we can write,

$$\sum_{i:\text{internal}} (\pi - \theta_i) - \sum_{j:\text{outward}} \left(\pi - \theta_j\right) = 2\pi \tag{6.10}$$

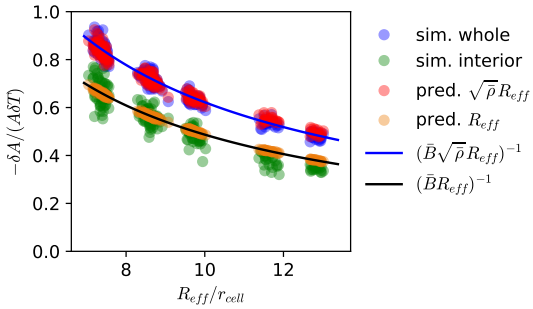

Figure 6.6: Scatter plot comparing the rate of compression $\delta A/(A\delta T)$ obtained in simulations with parameters of case A of clusters of different sizes and our predictions. The size of the clone is represented by its effective radius $R_{eff} = \sqrt{A/\pi}$ in the x-axis. Normalized by the average effective radius of a single cell $r_{cell} = \sqrt{0.55/\pi}$. We compare the predictions of equation (6.8) (red dots) with the rate of compression of the whole cluster (blue dots). As well, we compare the prediction of equation (6.9) (orange dots) with the rate of compression of interior cells (green dots), defined as cells whose centers are at least a distance $6r_{eff}$ from the surface. The continuous lines are the values that predicted by equation (6.8) considering the average roundness (blue), and by equation (6.9) (black). The cluster is prepared by taking all the cells inside a radius and adding cells that share most of their perimeter as part of the surface. The average roundness is $\rho = 0.61$. The cable in these simulations has a tension $4\%\Lambda$.

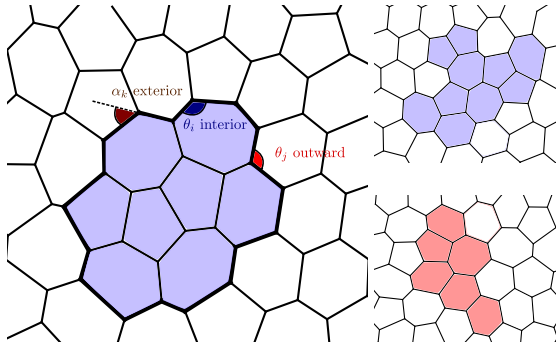

Figure 6.7: **Left:** Example of a small cluster and the angles over its surface. **Right:** Examples of a compact cluster in violet, and a non-compact cluster in red, with one cell that is only connected with one other cell in the group.

We can see that not only tensions influence the value of the boundary angles, but also topology. If the number of one type of angle increases and the other remains constant, then the average of the difference between the mean of each category must increase.

6.2.4 *Compact clusters*

The following analysis is more straightforward in the case of a compact cluster, i.e. a cluster where each cell has at least two neighbors that also belong to the cluster (see figure 6.7 for an example). Moreover, the analysis assumes and is more accurate for clusters that tend to be round, as produced by surface tension. Round clusters also tend to be compact in the above sense.

In compact clusters, by definition, each interior angle θ_i matches with an arriving junction between two adjacent cells, and each outward angle θ_j matches with a junction between two inner cells. Then, if there are N_s cells in the surface of the cluster and N_a cells adjacent to the cluster we can write,

$$N_a\left(\pi - \bar{\theta}_{in}\right) - N_s\left(\pi - \bar{\theta}_{out}\right) = 2\pi \tag{6.11}$$

where, $\bar{\theta}_{out}$ and $\bar{\theta}_{in}$ are the mean interior and outward angle respectively. This relation constrains the value of the mean angles θ_{out} and θ_{in}.

6.2.5 *Topological approximations*

Now that we can relate angles and the number of cells at both sides of a cluster boundary, we can go a step further and estimate those numbers from simple geometrical features.

A first property that produces an exact relation between the number of cells in the surface of the cluster N_s (i.e. cells that have as neighbor at least one cell outside the

cluster), and the number cells adjacent to the cluster N_a can be obtained by simple topological arguments. For the cluster, the Euler equation states that $v + c - e = 1$, where v is the number of vertices, c the number of cells in the cluster, and e the number of edges of the cells part of the cluster. In the case of trivalent junctions we have $3v = 2e$. In the case of a cluster we have vertices connecting only two edges,therefore $3v = 2e + N_a$, from which we get $3c - e = 3 - N_a$. On the other hand,$e = (\bar{n}c + N_s + N_a)/2$, where $\bar{n}$ is the mean number of sides for the cells in the cluster. Therefore, we obtain the exact relation,

$$\bar{n} = 6 + \frac{N_a - N_s - 6}{c} \tag{6.12}$$

We can predict the average number of sides per cells in the cluster by only knowing the total number of them and the difference between the number adjacent and surface cells. The quantity $q = N_a - N_s - 6$ is a topological charge of the cluster, i.e. the number of edges that need to be added or removed to have six sides on average.

We can approximate the numbers N_a and N_s by supposing that the cluster has a round shape, c cells inside with average area a_c, and regular cells with area a_0. The number of cells adjacent to the clone can be approximated by counting the number of hexagonal cells that can be packed along a perimeter. Considering a round clone, its perimeter can be approximated as the perimeter of a circle with the same area $L_c = 2\pi R$, with radius $R = \sqrt{ca_c/\pi}$. For the outer (and respectively inner) ring of cells, dividing this length by the width—distance between two opposing sides—of an hexagon of the area of the cells at each side ($h_a = \sqrt{a_0}\sqrt{3}\mu_6$ for an adjacent cell and $h_s = \sqrt{a_c}\sqrt{3}\mu_6$ for a cell in the cluster). We consider an augmented radius by half cell diameter for the outer ring, and respectively, a reduced radius for the inner ring, which gives a difference of $\pm\pi/2$. This is an approximation, and since the difference must be six on average in a uniform tissue (from equation (6.12)), we replace the $\pm\pi/2$ by 3 to recover the exact result in that limit,

$$\begin{aligned} N_a &= \frac{L_c}{h_a} + 3 && (6.13)\\ &= \sqrt{2\pi\sqrt{3}}\sqrt{c\frac{a_c}{a_0}} + 3 && (6.14)\\ N_s &= \frac{L_c}{h_s} - 3 && (6.15)\\ &= \sqrt{2\pi\sqrt{3}}\sqrt{c} - 3. && (6.16) \end{aligned}$$

We compare these approximations with simulations in figure 6.8, and find reasonable agreement. They slightly underestimate the number of cells since clones are not perfectly round.

6.3 INTERACTION BETWEEN HETEROGENEOUS CELLS

Finally, we have all the ingredients to address the initial problem from the theory: Can we predict the geometry of cells in an epithelium when they differ in their mechanical

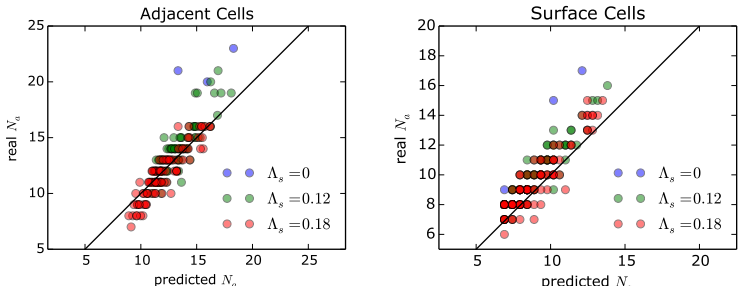

Figure 6.8: Comparison between the approximation from equation (6.15) and (6.16) for the number of cells adjacent to a clone N_a and in its surface N_s and the actual value, for a set of clusters that proliferate under different values for the surface tension. Edges in the boundary have a line tension $\Lambda_0 + \Lambda_s$, where $\Lambda_0 = 0.12$ is the default value for case A.

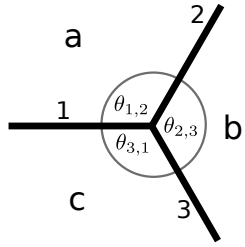

Figure 6.9: To write equations (6.17) and (6.18) for a given vertex, the labelling of cells, edges, and angles presented in the figure is used.

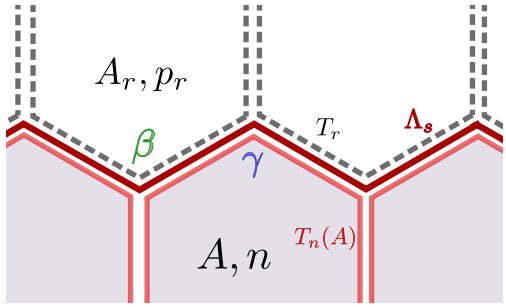

Figure 6.10: Simple geometry that can represent the properties in the surface of a large cluster of cells, as the frontier of two domains of cells: regular average cells of area A_r and perimeter p_r in white, and light violet cells representing cells in the clone of area A and n sides. In the frontier of the two domains of cells, a cable of tension Λ_s is added. Two degrees of freedom are captured by the outward angle β and internal angles γ formed in the frontier.

parameters? While the predictions cannot be expected to be exact, and need to be tested against simulations, it turns out that we can predict many relevant features with relatively simple expressions. The key will be, as before, to replace the details of individual cells by suitable averages, defined here for different classes of cells, to express force balance in the tissue. In general, the force equation in a vertex is given by the tension at their three edges and the difference on pressure,

$$\begin{aligned} F_{||} &= T_1 + T_2\cos(\theta_{1,2}) + T_3\cos(\theta_{1,3}) \\ &\quad + \frac{1}{2}l_2\Delta P_{b,a}\sin(\theta_{1,2}) + \frac{1}{2}l_3\Delta P_{b,c}\sin(\theta_{2,3}) \qquad (6.17) \\ F_{\perp} &= T_2\sin(\theta_{1,2}) - T_3\sin(\theta_{1,3}) \\ &\quad - \frac{1}{2}l_1\Delta P_{c,a} - \frac{1}{2}l_2\Delta P_{a,b}\cos(\theta_{1,2}) - \frac{1}{2}l_3\Delta P_{b,c}\cos(\theta_{2,3}) \qquad (6.18) \end{aligned}$$

Where $F_{||}$ designates the projection of the force over the direction of the edge 1 and $F_{\perp}$ designates the projection perpendicular to this direction, and is positive towards the direction of the edge 2. l_i is the length of the edge $i = 1, 2, 3$, $\theta_{i,j}$ the angle between the edge i and j. $\Delta P_{x,y}$ the difference in pressure between cells y and x.

6.3.1 *Mean-field approximation for a cluster of cells*

The simplest geometry that we can consider to capture the forces at the interface between mechanically different cells is presented in figure 6.10. This geometry can represent diverse situations, like the interface between cells mechanically divergent. Here, we will consider the case of a cluster of cells that is compressed by a cable of constant tension Λ_s on the surface. There are only two types of vertices, corresponding to internal and

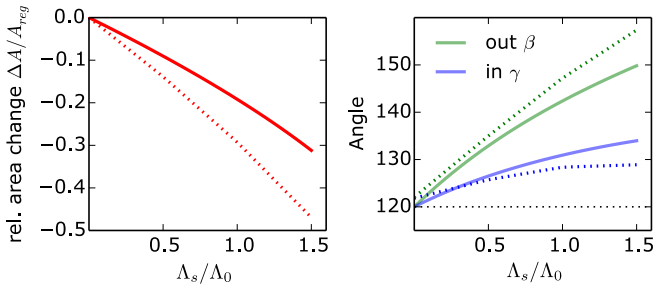

Figure 6.11: Solving the system of equations (6.20),(6.21) and (6.22) for different values of Λ_s and $c = 12$. Dotted lines are results from simulations. **Left:** Relative change on area as the tension in the surface increases. The area decreases, but not at the same rate than in the simulations. **Right:** Change on surface angles. Both of them get straighten by the tension as expected.

outward angles. In equilibrium, setting the force $F_{||}$ as defined in (6.17) to zero for these two classes of vertices leads to,

$$0 = 2T_r - 2\cos\left(\frac{\gamma}{2}\right)[T_r + T(A) + \Lambda_s] - lK(A - A_r)\sin\left(\frac{\gamma}{2}\right), \tag{6.19}$$

$$0 = 2T(A) - 2\cos\left(\frac{\beta}{2}\right)[T_r + T(A) + \Lambda_s] + lK(A - A_r)\sin\left(\frac{\beta}{2}\right). \tag{6.20}$$

$$\tag{6.21}$$

For these equations we can derive the inner and outward angles, by first computing the area A using Laplace's law, then approximating the tensions by their values for hexagonal cells, $T(A) = \Gamma\mu_6\sqrt{A} + \Lambda/2$ for cells in the cluster and $T_r = \Gamma\mu_6\sqrt{A_r} + \Lambda/2$ for regular cells. Computing the area of the cells from equation (6.9), which idealizes the border of the cluster as a circle with the same area (with an effective radius $R_{eff} = \sqrt{cA/\pi}$), recovers the correct trends in areas and angles, but underestimate compression inside the clone (figure 6.11). Indeed, we have found in section 6.2.2 that the compression is better predicted by taking into account the full length of the border. There is no simple way to predict this full length, but if we take the average cluster roundness ρ from simulations (see figure 6.12), and use the perimeter $L = 2\pi\sqrt{\rho}R_{eff}$ in equation 6.8 yielding

$$B\left(1 - \frac{A}{A_r}\right) = \frac{\Lambda_s}{\sqrt{\rho}R_{eff}} \tag{6.22}$$

we find a close agreement with simulations, in terms of both compression and changes in angles as the tension increases, as shown in figure 6.13

The angles vary accordingly to our intuition: An increase in tension makes them flatter. However, they do it at a different rate, with the outward angles being more responsive

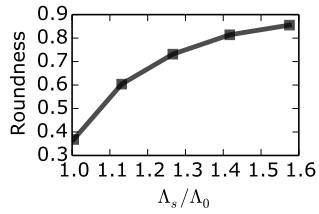

Figure 6.12: Roundness of clones subjected to different levels of surface tension.

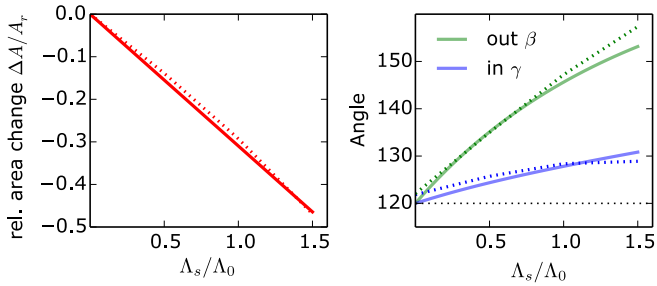

Figure 6.13: Solving the system of equations (6.20),(6.21) and (6.22) for different values of Λ_s and $c = 12$. Dotted lines are results from simulations. **Left:** Relative change on area as the tension in the surface increases. **Right:** Change on surface angles. Both of them get straighten by the tension as expected.

than the internal ones. The topology strongly affects the response to an increase in tension at the clone boundary. We saw as well as its influence in equation (6.11) that constrains the summation of total angles.

6.3.2 *Two identical interacting cells*

The exact solution of two interacting cells of diverse polygonal classes can only be addressed by actually solving over the equations (6.17) over all their vertices. No symmetry allows us to write a simple system. A simplified system for which explicit analytical calculation can be performed, is formed by two identical n-sided cells sharing an edge of length l (that is a chord in the circle of radius r which contains the other edges

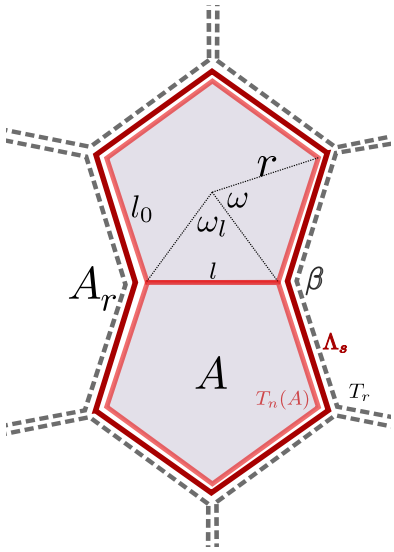

Figure 6.14: Diagram of our model for two identical cells interacting, showing the variables used to describe their geometry.

as well). Each vertex is at a distance r of the center of the circle. This gives the following values for the angles and edges depicted in figure 6.14,

$$\omega_l = 2\arcsin\left(\frac{l}{2r}\right) \tag{6.23}$$

$$\omega = \frac{2\pi - \omega_l}{n-1} \tag{6.24}$$

$$l_0 = 2r\sin\left(\frac{\omega}{2}\right) \tag{6.25}$$

$$A = \frac{r^2}{2}\left[(n-1)\sin(\omega) + \sin(\omega_l)\right]. \tag{6.26}$$

ω_l is the center angle associated with the edge of length l, ω the center angle associated with the other edges, l_0 is the length of the other edges of the cell, and A the cell area. Here, we have only two types of vertices, the two belonging to both cells, and the ones that only correspond to one cell. In equilibrium, setting the force $F_{||}$ as defined in (6.17) to zero for these two classes of vertices leads to,

$$0 = 2T_r - 2\cos\left(\frac{\omega}{2}\right)\left[T_r + T(A) + \Lambda_s\right] - l_0 K(A - A_r)\sin\left(\frac{\omega}{2}\right), \tag{6.27}$$

$$0 = 2T(A) + 2\cos\left(\frac{\omega_l}{2}\right)\left[T_r + T(A) + \Lambda_s\right] - lK(A - A_r)\sin\left(\frac{\omega_l}{2}\right). \tag{6.28}$$

$$\tag{6.29}$$

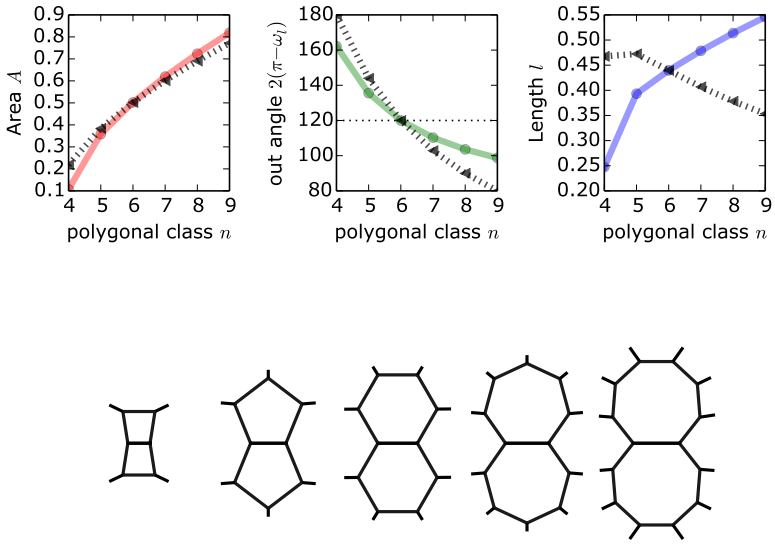

Figure 6.15: **Top:** Interaction between two cells for different values of their number of neighbours n. The dotted lines correspond to the values obtained with the geometry of a cell in isolation. Angle corresponds to the external angle between the two cells. Length to the length of the shared junction. **Bottom:** Examples of the geometry obtained for different pairs of cells of the polygonal classes 4 to 8.

Cells bigger than the typical cell will have a bigger perimeter, thus a bigger tension under the vertex model. Then the angle $\beta = 2(\pi - \omega_l)$ between the two interacting cells will be flatter. That the effect remains limited may explain in part why the mean-field approximation is successful in predicting the size of cells according to their number of edges, even though it ignores correlations between neighbors, which are replaced by average cells. Even in a relatively extreme case, for instance, two eight-sided cells interacting together, the effect on their area and geometry is small. And the only case where we observe a significant difference is a pair of four-sided cells, that is precisely the case where the area predicted by the mean-field approximation deviates most from simulations.

6.4 CONCLUSIONS

In the previous chapter 5, we introduced our mean-field approximation and applied it to address cell heterogeneity. Simple models can capture the average geometry of isolated cells that differ from their surroundings in mechanical properties or proliferation rate, or clusters of cells under a cable of tension. How a tension cable generates pressure unveils interesting aspects of our discrete system that a continuous approximation cannot properly capture, as we saw in section 6.2.2.

Our mean-field approximation is based on the idea that beyond the many particular different topologies and geometries, if there is a way to group vertex under a meaningful category, then we can study the average vertex for each case and unveil how the average case will behave. Our approximation is limited to cases where it is possible to exploit this approximate symmetry.

Not every aspect can be addressed under this mean-field approximation: topology is still elusive to analysis, it strongly depends on the way cells proliferate - to mention one factor. We found that a critical ingredient to predict the effect of a cable of tension over a cluster of cells is knowing how round it is.

The framework that we have developed allows us to understand in the context of the vertex model how each parameter affects the geometry of cells. Simple equations give us a good approximation of the geometry and topology of cells that differ mechanically from their environment. These tools can be applied to experimental data, as we will see in chapter 7.

7 MODELING SHAVENBABY MUTANT CLONES

In this chapter, we will apply the tools developed to understand tissues with a heterogeneous array of cells to analyze the growth of clones in the *Drosophila* notum in an experiment performed in the group of François Payre (University of Toulouse) [Soulard et al., 2019]. Their differentiation is in one case promoted prematurely (activator case or ovo B clones), or delayed (repressor case or ovo A clones). First, we present a geometrical analysis of target features and reproduce them using the vertex model with clone inclusion. We explore the space of mechanical parameters in the vertex model, searching for the parameters or region of parameters that can accurately describe the experimental findings. Doing this, we discovered an ingredient that was missing in the activator case: cells adjacent to the clone tend to divide along an axis that is perpendicular to the surface of the clone, limiting the addition of new neighbors to the clonal cell. Simulations are compared with our mean-field approximation with satisfactory results.

7.1 EXPERIMENTAL ANALYSIS

In this section, we will show the main features found in Shavenbaby mutant clones, obtained from the segmentation of experimental images and compared to control clones (examples of those are shown in image 7.1).

7.1.1 *Adjusting parameters to model our experimental data*

For our experimental analysis, we have used three sets of images: control, repressor, and activator. For each of those cases, we have experimental data at two different stages: at 20 hours and 38 hours after the *white puparium* stage. All the mutants were induced six hours before this stage. By observing the mean area by polygonal class, we chose parameters that reproduce the Lewis' law in images at 20 hours of development. We found that the parameters for case A that well represent the wing disc epithelium [Farhadifar et al., 2007] is also a good set of parameters to model our experimental data (see figure 7.2).

In all our analyses, we only consider *core cells*, i.e. cells that are surrounded by other cells visible in the same image. Also, we excluded clones where one or more cells are in contact with a precursor sensory organ.

7.1.2 *Labeling elements in the tissue with respect to the clone*

We will classify cells and junctions in categories, according to their degree of topological separation with the clone surface: edges in the surface get the index $e + 0$; edges

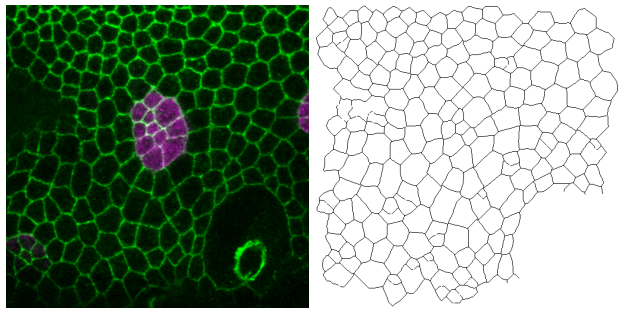

Figure 7.1: **Left:** Example of image obtained from experiment [Soulard et al., 2019]. This example is a repressor clone at 38 hours. **Right:** Skeletonatized image where cell boundaries are detected, obtained by processing the image at the left.

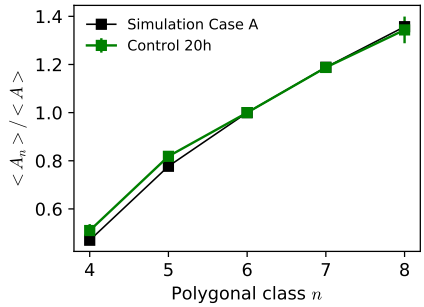

Figure 7.2: Relative area by polygonal class, comparing experimental images at 20 hours and simulations for case A. Simulations show very good agreement with simulations under parameters for case A.

connecting to a vertex in the surface get the index $e-1$ if they belong to the clone, or $e+1$ if they belong to cells adjacent to the clone, etc. Analogously, cells with edges defining the surface of the cluster get the index $c-1$ if they belong to the clone, or $c+1$ if they are adjacent to the clone. Note that this is a topological measure of distance to the clone, which may differ from an ordering based on metric-distance. An illustrative example is shown in figure 7.3.

This handy notation allows us to generalize and designate new categories easily. For instance, $e>0$ will denote the union of the categories $e+n$ with $n>0$ and represents all the edges that do not belong to clonal cells. In the same way, $e>2$ denotes the category of edges that do not belong to any cell in contact with the clones.

7.2 SIMULATING A CLONE

To simulate clones, we choose the value of the mechanical parameters associated with clonal cells to differ from regular cells. The latter keep the value fitted for case A, i.e. preferred area $A_0=1$, cell perimeter contractility $\Gamma_r=0.04$, and line tension $\Lambda_r=0.12$. Edges will be classified into three categories: regular, surface, and interior. 'Regular' are the edges that connect two regular cells ($e>0$), and they will keep the default value Λ_0; 'interior' edges, are those that connect two clonal cells ($e<0$), and may vary in their value Λ_c; and 'surface' edges, these connect a clonal cell and a regular cell ($e+0$), and will take the value of the average between Λ_r and Λ_c, plus an imbalance Λ_s. As a summary, the effective Λ at each edge given the position is,

$$\text{regular } e>0 \quad \Lambda \to \quad \Lambda_0 \tag{7.1}$$

$$\text{surface } e+0 \quad \Lambda \to \quad \Lambda_s + \frac{1}{2}\left(\Lambda_c+\Lambda_0\right) \tag{7.2}$$

$$\text{interior } e<0 \quad \Lambda \to \quad \Lambda_c. \tag{7.3}$$

In this section, the relative area is explored as the preferred area A_0 and the value of line tension in the surface of the clone Λ_s vary, given a fixed value for the line tension in the clone Λ_c.

Although cell elimination may play a role in the experiments, for simplicity we chose to exclude it from the model. To prevent cells from being compressed to the point where they collapse, the energy function is modified to diverge at area zero. How pressure varies far from the equilibrium is not a trivial problem, and we have no reason to stay attached to the choice. We find convenient to modify the vertex model energy function as follows,

$$E=\sum_{edges}\Lambda_e l_e+\sum_{cells}\frac{1}{2}\Gamma_c p_c^2+\sum_{cells}\frac{1}{2}K\left(A_c-A_0^c\right)^2\left[1+\frac{\varepsilon}{A_c^2}\right]. \tag{7.4}$$

The parameter ϵ controls how strong this avoidance of compression is. The chosen value is $\epsilon=0.001$. With such a small value, the effect on the behavior of the model is negligible, except when a cell approaches exclusion.

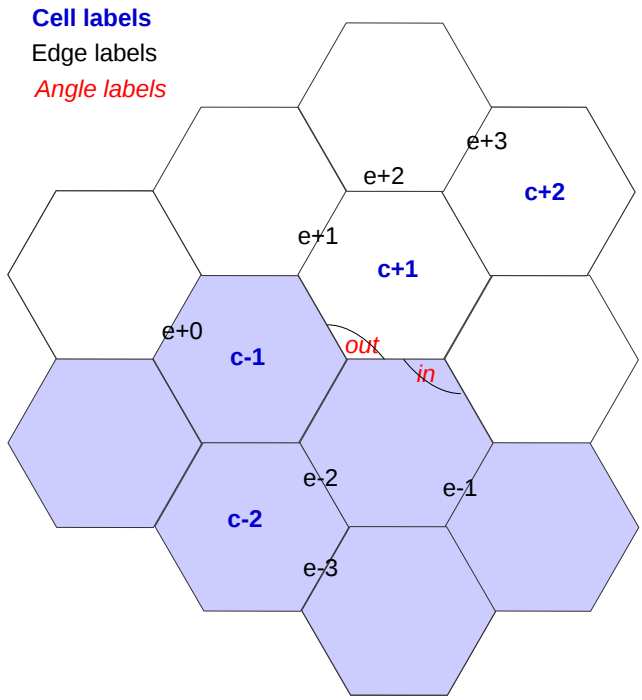

Figure 7.3: Illustrative image of a tissue with examples of edges and angles labels. The indices are a measure of how topologically far an edge or a cell is from the surface of the clone. Edges on the surface of the clone are labeled $e+0$. Cells that have at least one edge $e+0$ are labeled $c+1$ if they do not belong to the clone, and $c-1$ if they do. The relevant angles are in the surface of the clone, and we label them as in/ out if they are in the interior/exterior of the clone.

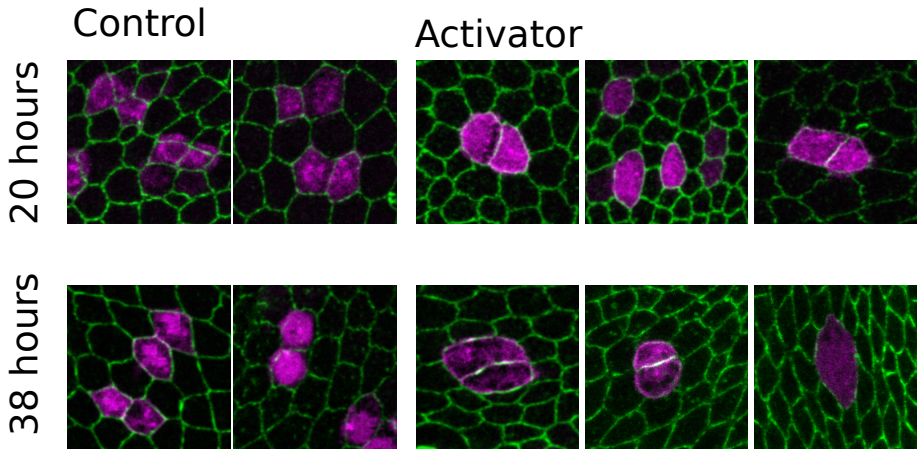

Figure 7.4: Examples of activator and control clones at 20 hours and 38 hours.

7.3 ACTIVATOR CLONES

7.3.1 *Experimental analysis*

In the activator case, cell division is prematurely arrested, and clones usually comprised of one or two cells. Examples of these clones compared with control clones are shown in figure 7.4. The most noticeable characteristic of clonal activator cells is that they tend to be bigger than wild-type cells, particularly in unicellular clones, as it can be seen in figure 7.5. We will analyze the unicellular and bicellular cases separately. Clones with more than two cells are rare at 38 hours.

As expected, unicellular clones tend to have more than six neighbors. On average, almost seven neighbors are found in our data set. Surprisingly, cells in bicellular clones, even though they are on average almost as big as seven-sided WT cells, have just above six sides on average, as it can be seen in figure 7.6.

Making use of the force inference tools introduced in the background section, we estimated the relative tensions among diverse categories of edges. We used two different methods. However, here we focus on just one of them [Chiou et al., 2012], as the results obtained with the two methods are consistent. Junctions in the clone are slightly bigger compared to the direct neighbors $e+1$ (figure 7.7). In the case of bicellular clones, the interior edges are inferred to have a much smaller tension. The dissimilarities in the inferred tension are strongly correlated to differences with average angles at various positions of the tissue, which are of 120°on average in a tissue where three edges meet each other (see figure 7.8). The low tension in the interior edges $e-1$ is consistent with

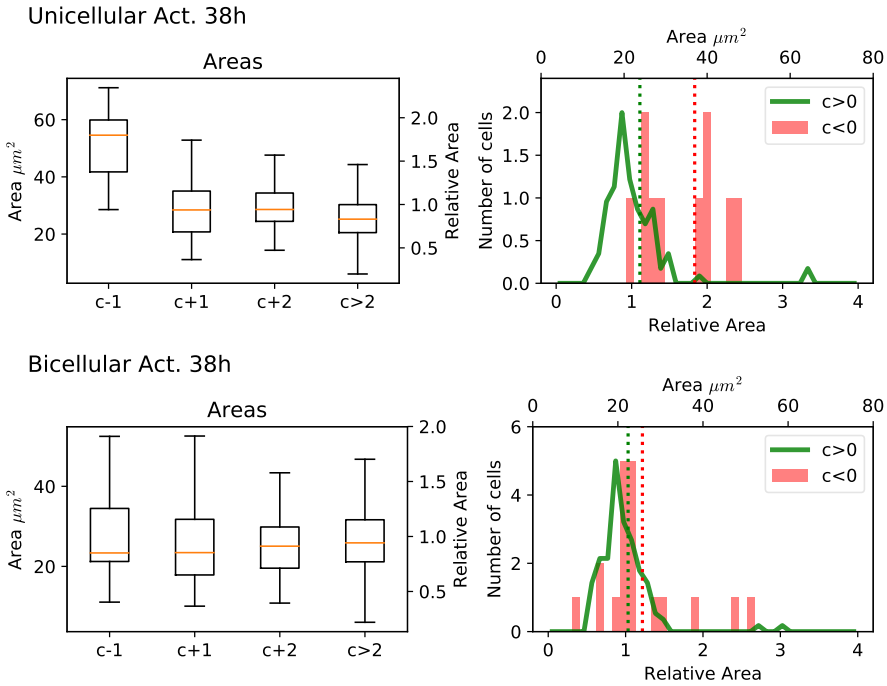

Figure 7.5: Analysis of the average and distribution of cell areas comparing clonal cells ($c < 0$) and WT cells ($c > 0$). In the unicellular activator case **(top)**, clonal cells on average have an area almost twice bigger than regular cells. In the bicellular activator case **(bottom)**, clonal cells are slightly bigger than WT cells. The y axis count the number of cells for clonal cells, and WT cells are normalized in arbitrary units.

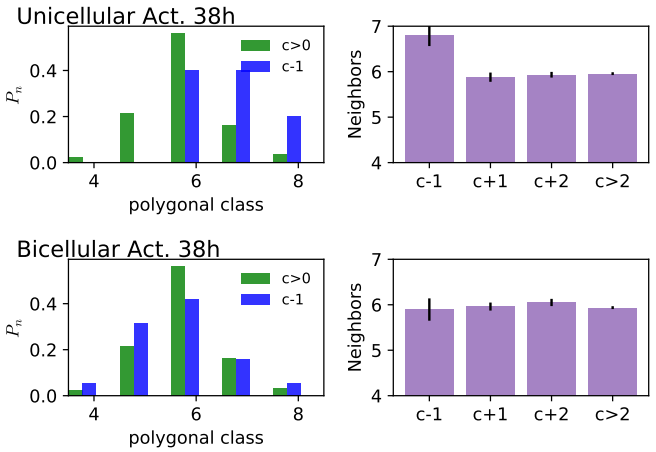

Figure 7.6: Distribution of polygonal classes (left) and number of neighbours (right) for cells given their relative topological position to the clone in the activator case **Top:** Unicellular clones. **Bottom:** Bicelullar clones.

the flat out angle found in those clones, as well as with the longer edge that separates clonal cells, as shown in figure 7.7.

7.3.2 *Target features*

In our simulations, we will aim to find the right parameters to obtain clones that are geometrically similar to our typical experimental examples. In particular, our target will be to reproduce the cell area and the number of neighbors for the case of unicellular clones. In addition to those two features, in the case of bicellular clones, we will aim to reproduce the mean outward angle and the average length of the edge category $e-1$ (between two cells). Table 7.1 makes a summary of all those values. We will accept values within a tolerance around the average value. This tolerance will be twice the standard error.

Many parameters may be compatible with each of those values. Here we will present our simulations in contour plots where the compatible regions are highlighted with a color mask.

Our collaborators have reported that clonal cells often have their cell cycle disrupted [Soulard et al., 2019]. They develop until G2 but fail to complete mitosis, as revealed by the accumulation of nuclear material. For this reason, we expect that a proper model of ovo B clonal cells will have a bigger value for the preferred area A_0^c. Moreover, the accumulation of actin and myosin at the clone boundary suggests that the values for the line tension in the surface Λ_s and Λ_c may be divergent. We run simulations with

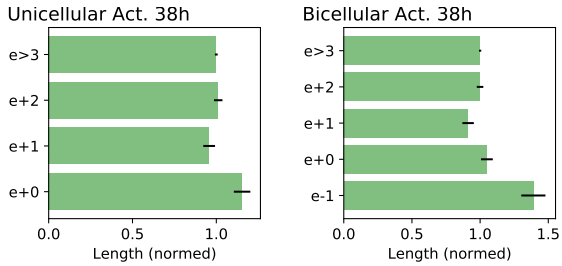

Figure 7.7: Average length for edges in diverse positions relative to the clone in the activator case at 38h, for unicellular (left) and bicellular (right) clones. The lengths have been normalized with the global average.

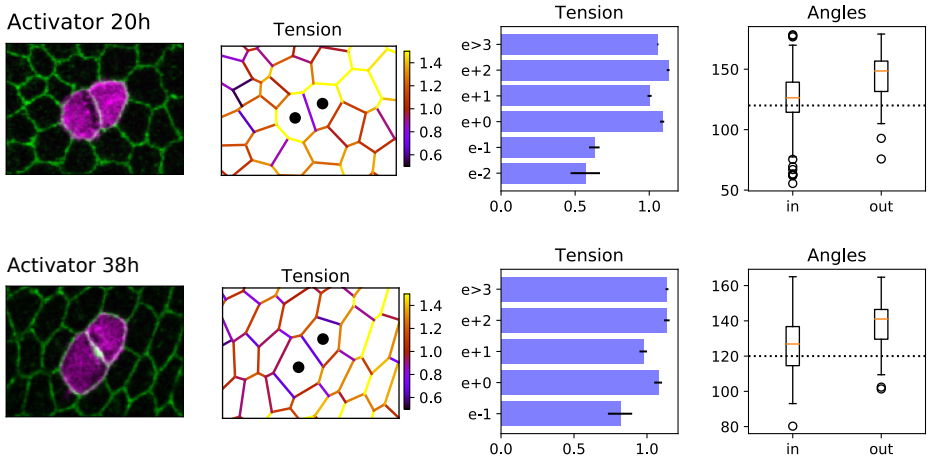

Figure 7.8: **Left:** Example of clones for activator case at 20 hours and (**top**) 38 hours (**bottom**). **Center left:** Vertex representation of the same clone with the edges colored by their inferred tension. **Center right:** Average of inferred tension for edges in different positions relative to the clone. In this case, we observe that in both cases, the tensions in the interior of the clone are lower than in the exterior. The surface has a tension higher than the average over the edges directly adjacent to the clone $e+1$, but not significantly higher than edges far away from $e > 3$. The differences are more noticeable at 20 hours. **Right:** Box plot of angles on the surface of the clone. The dotted line is 120 degrees.

Unicellular	color	Value	Tolerance
Area	Red	1.65	$\pm$ 0.32
Neighbors	Blue	6.8	$\pm$ 0.47
Bicellular	color	Value	Tolerance
Area	Red	1.18	$\pm$ 0.25
Neighbors	Blue	5.89	$\pm$ 0.49
Angle out	Green	127.35	$\pm$ 7.47°
Length e-1	Purple	1.39	$\pm$ 0.18

Table 7.1: The experimental values measured for activator clones at 38 hours. Statistics for unicellular and bicellular clones are shown separately. Area and length are normalized by the area of cells $c+2$ and the length of edges $e+3$ respectively. The tolerance corresponds to twice the standard error. For each feature, the color that will be used to highlight the region of compatible parameters is shown in the second column.

parameters taken from a grid. For points in between, the value is estimated by linear interpolation.

Simulations are run for a fixed time, starting with 20 cells. The tissue relaxes, and then one cell is chosen at random as a clonal cell. In the case of bicellular clones, this clonal cell will undergo a cell division after a short relaxation time before it is assigned its new mechanical parameters. For both cases, unicellular or bicellular, the clonal cells do not divide.

7.3.3 *Unicellular clone simulation and division bias*

It is not as simple as one might expect to model a single clonal cell. The only features we can model for an isolated cell are the number of sides and areas. Nonetheless, the simple analysis presented in section 6.1 is not enough as it does not predict the number of sides, and simulations showed that there were no parameters that matched both of these features.

In figure 7.9 we observe, unsurprisingly, that the cell area increases with increasing preferred clonal area A_0^c, and decreases with the additional line tension Λ_s. The same trend is observed for the number of neighbors, and the internal angle cannot but follow the average number of neighbors as it is constrained by basic geometry. There is no match for the area and the number of neighbors as we vary the preferred area A_0^c and the line tension associated with the clonal cell Λ_c. Unicellular clones have more neighbors than a WT cell, but not as much as their area suggests. Even more surprising, if we analyze this using the model (6.4) in chapter 6 for a sub-proliferative cell: the neighboring cells divide, the clonal cell continuously gains new sides, and it is predicted to have more neighbors than a WT cell with the same area. An extra factor must be added. We propose that division in cells $c+1$ around the clone does not follow Hertwig's rule. Instead, cells choose an axis that avoids adding a new neighbor to the clone; they preferentially divide along a division plane perpendicular to the clonal surface. Simulations with this bias

show that in this case, not only we can find parameters compatible with the experimental values, but that there is almost a complete overlap in the regions where the area and number of neighbors coincide with the experiment (see figure 7.9).

Under biased division, clonal cells with no extra tension are still more likely to be smaller than a normal cell, an opposite trend to the one observed in the unbiased case.

Back to the experimental data, we found that the main axis of cells adjacent to the clone $c+1$ are oriented parallel to the surface of the clonal cell with whom they are in contact, as can be observed in figure 7.10. *In-silico*, regardless of the parameters, the tissues with the unbiased division are oriented against the surface of the clone, providing more evidence for the bias in cell division,

With this evidence, our collaborators measured and corroborated our hypothesis: cells around the activator clone did consistently have biased divisions (see figure 7.11).

Explaining the mechanism and origin of this division bias are beyond the scope of this work, but they might be related to the fact that cell division in epithelia is not a process that involves the mitotic cell alone but also its neighbors, which react to support the division of the mitotic cell during cytokinesis [Pinheiro et al., 2017]. Also, it has been found that a cable at compartment boundaries orients division of cells in contact with it, preventing them from creating a new junction towards the cable [Scarpa et al., 2018]. This example of mechano-sensing factors affecting cell division is consistent with our results here. However, as we will see later, we do not find the same bias in the repressor case as both of those explanations would suggest.

7.3.4 *Bicellular clone*

Having uncovered cell division bias, we consider now the case of bicellular clones. This case will not necessarily be modeled by the same parameters as the unicellular case. In this situation, two additional features are the targets for our model, the outward angle and the internal length. One new mechanical parameter appears, the line tension associated with the clonal cells Λ_c, that previously was redundant with Λ_s.

The trends regarding the change in area and number of neighbors when changing the surface line tension Λ_s and preferred clonal area A_0 are the same as for the unicellular clone. The line tension of clonal cells Λ_c is redundant and has the effect of displacing the diagram shown in figure 7.12. Furthermore, here, we find a region of parameters where the area and the number of neighbors under biased division agree with the experimental observations. Concerning the outward angle and length of $c-1$ edges, they both increase with surface line tension as might be expected. Nevertheless, the length does not depend much on the preferred area. This discrepancy in behavior constrains the space of parameters that reproduce the geometry found experimentally.

Note that the total tension of an edge depends on the perimeter as well as on the line tension parameter. In the regions where we find the best match, we observe a clear increase for the tension in the clone boundary (see table 7.2). Nonetheless, in the two cases, we have redundancy in parameters, and therefore, simulations do not completely

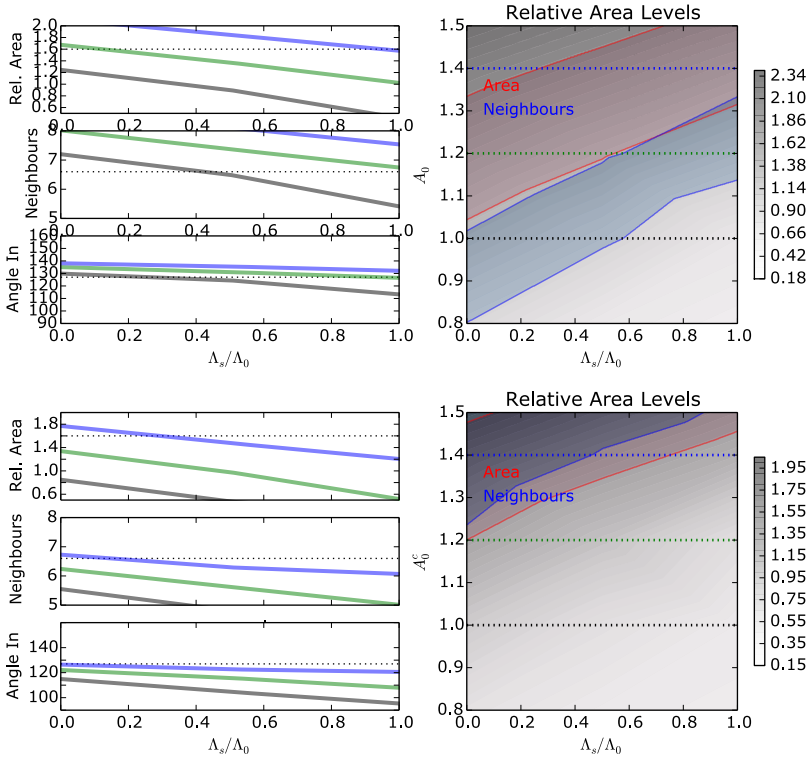

Figure 7.9: Parameter determination for unicellular activator clones. Contour plot of average relative areas for clonal cells as their preferred area A_0^c varies in the vertical axis, and the line tension Λ_s varies in the horizontal axis. The regions where the target geometrical features at 38 hours are inside the ranges define in table 7.1 are highlighted with a semi-transparent color mask; in this case, cell area (red) and the number of neighbors (blue). **Top:** All non-clonal cells divide following Hertwig's rule. There is no possible value of parameters where both geometrical features are satisfied. **Bottom:** Non-clonal cells around the clone have a biased division that avoids giving new sides to the clonal cell. In this case, there is an almost complete overlap between regions representing the different constraints. A wide range of parameters can model the observed geometry. **In the left**, we show the variation of relative area, number of neighboring cells, and internal angle, with line tension on the surface. Each line corresponds to a different preferred area A_0^c. $A_0^c = 1.4$ (blue), $A_0^c = 1.2$ (green), $A_0^c = 1$ (grey).

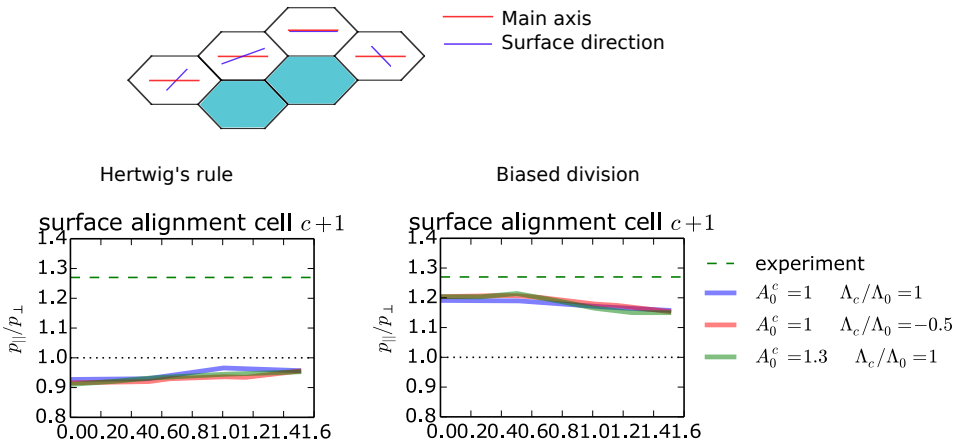

Figure 7.10: Ratio between the projection of the main axis of adjacent cells $c+1$ over the surface of unicellular clones. **Top:** Example of the main axis in red, and their projection over the surface of the clonal cells in blue. The precise mathematical definition can be found in A.1.7 **Left:** Unbiased division with all cells following Hertwig's rule. **Right:** Biased division, where cells adjacent to the clone divide with the axis of division parallel to the surface of the clone.

determine the possible values. Preliminar simulations with the pressure-less model presented in section 4.4 agree with the possible values for the tensions as well.

7.3.5 *Mean-field model for two identical clonal cells*

Now we can look back and study the case of bicellular clones using our mean-field approach. As we presented in 6.3.2, we can consider a pair of n-sided cells with the same area, parameterized by a radius r, and the length l of the shared junction. If our model captures all the ingredients that shape the geometry of the clones, this model should be able to reproduce the results found in our previous simulations. The number

	A_0^c	Λ_s/Λ_0	Λ_c/Λ_0	T_s/T_0	T_i/T_0
Unicellular	1.3	0.2	1.0	1.12	-
Unicellular	1.5	0.8	1.0	1.33	-
Bicellular	1.2	0.5	1	1.18	1.04
Bicellular	1.0	0.5	-0.5	1.00	0.63

Table 7.2: Numerical values for the parameter modeling the experimental activator clones, and tensions in the surface T_s and in interior T_i relative to the tension T_0 in a regular cell. In both cases, we show two sets of possible parameters.

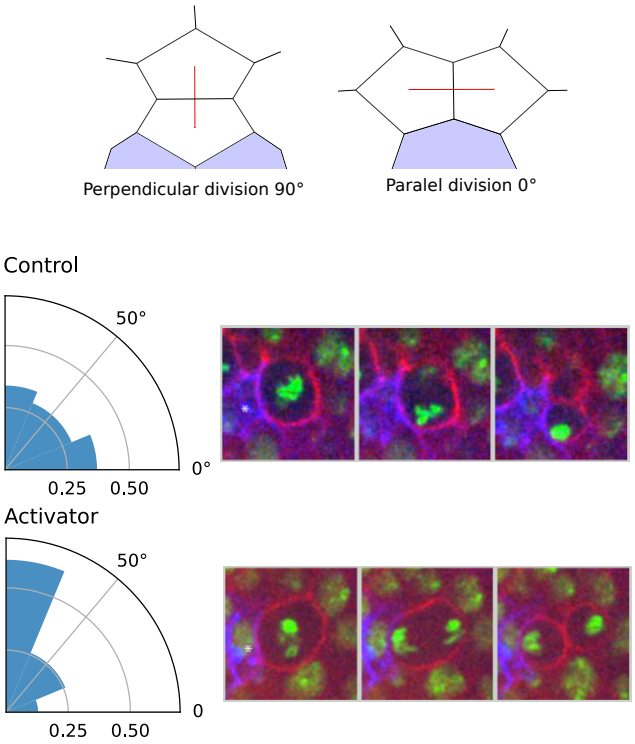

Figure 7.11: **Top:** Diagram showing the cases of a perpendicular and parallel cell division with respect to a clone that is represented in blue. **Bottom left:** Experimental corroboration of the bias in cell division for cells adjacent to the clonal surface. Angles are measured between the axis of the division, given by the line that connects the center of the two daughter cells, and the clonal surface. This result was originally predicted from our numerical simulations. **Bottom right:** Example of cells division for each case (clonal cells are marked in purple)

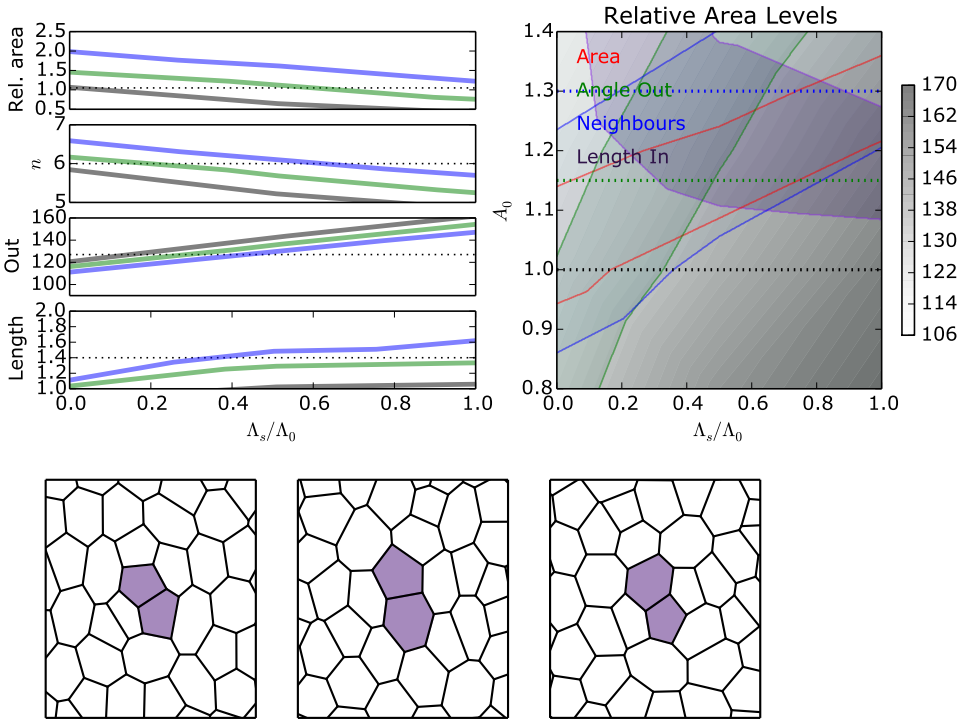

Figure 7.12: Parameter determination for bicellular activator clones. **Top right:** Contour plot of average relative areas for clonal cells as their preferred area A_0^c varies in the vertical axis, and the line tension Λ_s varies in the horizontal axis. The regions where the target geometrical features at 38 hours for bicellular clones are inside the ranges define in table 7.1 are highlighted with a semi-transparent color mask (cell area in red and the number of neighbors in blue). **Top left:** Variation of relative area, number of neighboring cells, outward angle, and length of the edge within cells with line tension in the surface. Each line corresponds to a different preferred area A_0^c. $A_0^c = 1.3$ (blue), $A_0^c = 1.15$ (green), $A_0^c = 1$ (grey).**Bottom:** Examples of clone with the parameters $\Lambda_s/\Lambda_0 = 0.5$, $A_0 = 1.2$, that our simulations suggest are the good region to model clonal cells, at $t/\tau_{div} = 3$ and biased division.

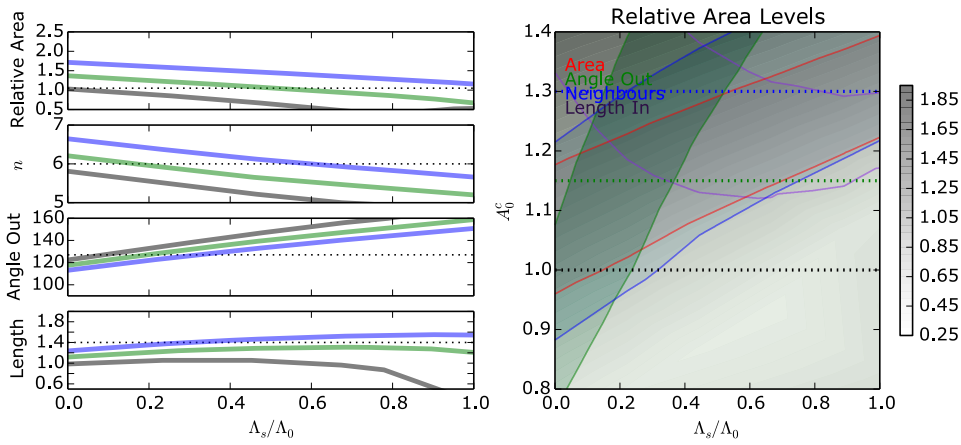

Figure 7.13: Contour plot of the regions where the target features satisfy our constraints, obtained from the mean-field model proposed in section 6.3.2. The number of neighbors for each parameter have been obtained directly from simulations.

of neighbors is a feature that the mean-field approximation does not provide, and it is critical to reproduce clonal geometry. These values will be directly extracted from simulations.

As can be observed in figure 7.13, the features predicted in our simplified case exhibit behavior in qualitative agreement with our simulations, reproducing the trends found as we vary the preferred area A_0^c and tension in the surface Λ_s. However, in this case, we do not find a good quantitative agreement with simulations. Moreover, the angles and areas tend to be overestimated.

7.4 REPRESSOR CLONES

7.4.1 *Experimental analysis*

In the repressor case, the clones of cells keep proliferating while their surrounding cells have started their differentiation. These clones have more cells than control or activator clones. Some examples of their shape can be observed in figure 7.14. The first noticeable feature is that in the repressor case, clones have a rounder shape compared with control clones. Here, roundness is defined according to the perimeter L and total area A_T of the clone as $R = 4\pi A_T / L^2$. In this way, a circle has roundness $R = 1$ and a line $R = 0$ (see figure 7.15).

With respect to the clonal cell area, repressor and activator clones show opposite trends While activator clones tend to have bigger cells, the repressor clones tend to have smaller cells, with a significant difference between cells on the surface (that is, cells that are

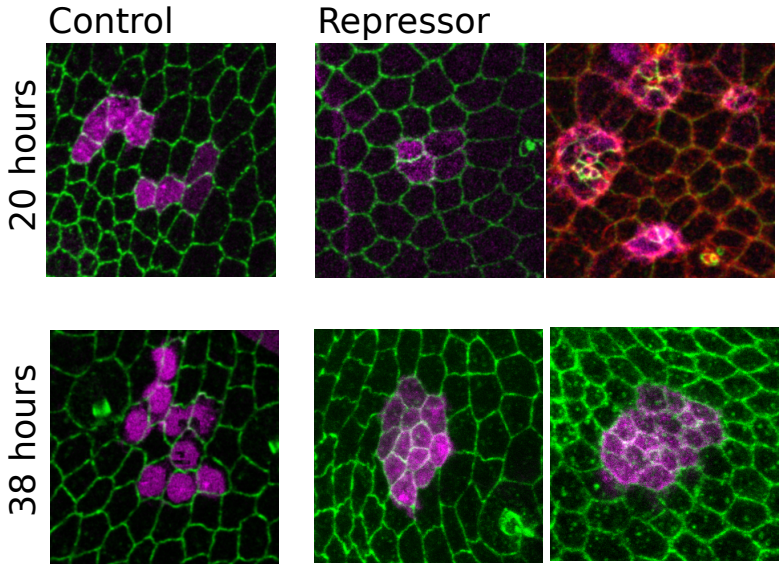

Figure 7.14: Examples of repressor and control clones at 20 hours and 38 hours.

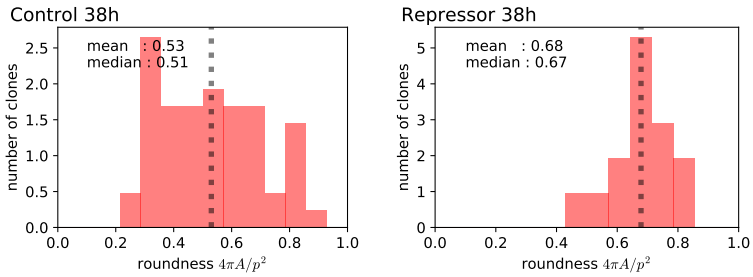

Figure 7.15: Distribution of roundness in clones, measured from the perimeter L and the total area A_T, $R = 4\pi A_T/L^2$. **Left:** Control case at 38 hours. **Right:** Repressor case at 38 hours. Repressor clones are consistently rounder than control clones. The vertical line corresponds to the mean of the distribution.

neighbors of at least one non-clonal cell) and cells completely embedded in the clone, as shown in figure 7.16.

In repressor clones, again, this trend still holds even when we compare cells with the same number of neighbors. As for the distribution of polygonal classes, clonal cells have, on average, less than the six neighbors expected for a WT cell. Cells in the inner region of the clone have an even lower average. Cells directly adjacent to the clone $c+1$ tend to have an average number of neighbors above six, explained by the smaller size of clonal cells (see figure 7.17).

Other features we measured were the angles between edges in the surface of the clone and the inferred tension among various categories of edges (see figure 7.18). Edges in the interior of the clone $e < 0$ have a weaker inferred tension. On the surface, edges $e+0$ have an inferred tension that is slightly stronger than the directly adjacent edges $e+1$ and $e-1$, but still lower than the average. Accordingly, the angles on the surface suggest a relatively stronger tension in the surface, with outward angles that are substantially flatter than 120 degrees. This, in addition to the roundness of the clones, goes in the direction of the existence of a superficial tension in the interface between the clones and the surrounding tissue.

7.4.2 *Target features*

The repressor case has more features to be matched compared with the activator case, namely: The clonal cell area, internal and outward angles, and clone roundness. At the same time, our collaborators do not have evidence of accumulation of nuclear material or other reasons suggesting that clonal cells must be modeled with a divergent preferred area A_0^c. We will only consider two parameters, namely, the line tension in the surface Λ_s and the line tension for the clonal cells Λ_c. In the same spirit, we will present the result of our exploration as contour plots highlighting the regions compatible with our experimental examples. Table 7.3 contains a summary of all those values.

7.4.3 *Simulating a repressor clone*

In the same way, as for the activator case, the compatible regions for the observed geometry in the repressor clones are explored, this time taking a fixed preferred area and exploring the values of the line tensions Λ_c and Λ_s. For those chosen parameters, simulations will be run in a grid. For points in between, the value will be estimated by linear interpolation.

Simulations are run for a fixed time, starting with 20 cells. The tissue relaxes, and then one cell is randomly chosen as the clonal cell. The duration of the simulation is chosen such that the number of cells in the clone matches the average number in experiments.

By comparing the average for simulated clones at two different stages—when they have 4, and 8.8 cells in average—we can obtain a robust conclusion about how the heterogeneity of line tension affects the clone geometry. Clone roundness depends above all on the surface line tension Λ_s, consistent with previous results presented in

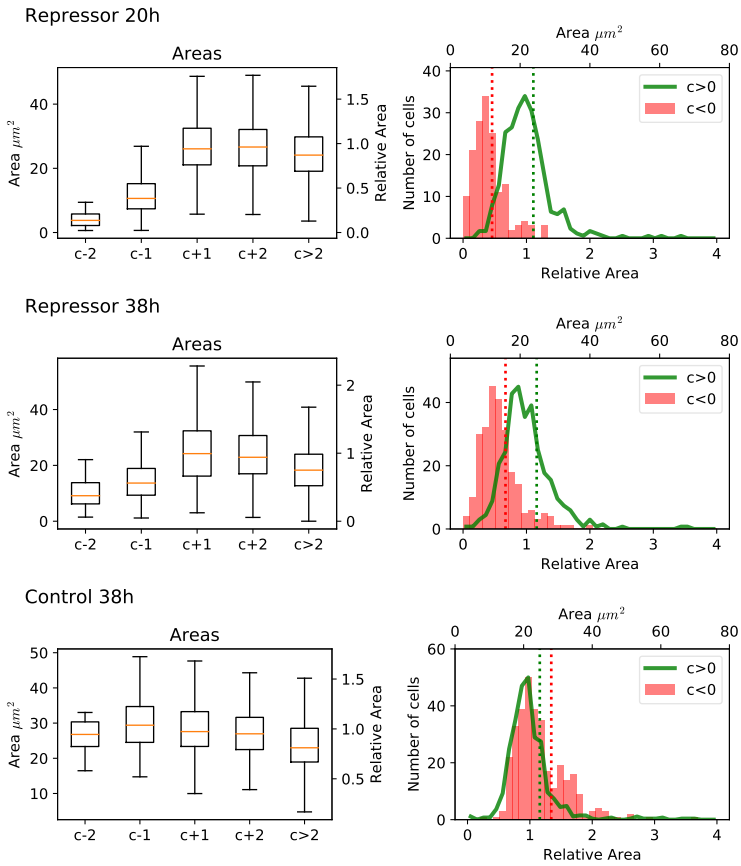

Figure 7.16: Analysis of the area average and distribution in clonal cells ($c < 0$) and WT cells ($c > 0$), for repressor clones at 20 hours (**top**), 38 hours (**middle**) and control clones at 38h (**bottom**). (**Left:**) box plot for comparing each relative position in the clone. (**Right:**) we compare distributions for WT and clonal cells. In the control case, clonal cells are not significantly bigger than regular cells, as expected. Cells completely embedded in the clone are slightly smaller. In the repressor case, clonal cells are on average almost twice smaller than regular cells, even when compared by number of neighbours.

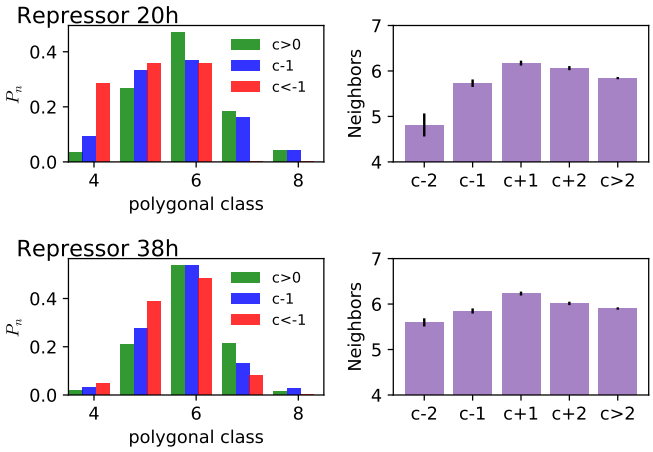

Figure 7.17: Distribution of polygonal classes (left) and number of neighbours (right) for cells given their relative topological position in the clone in the repressor case. On top, at 20 hours and at the bottom at 38 hours.

Ovo A at 20h	color	Value	Tolerance
Area	Red	0.44	± 0.04
Angle in	Blue	121.69	± 2.14°
Angle out	Green	145.50	±3.47°
Roundness	Purple	0.75	± 0.03
Number of cells	-	4.0	-
Ovo A at 38h	color	Value	Tolerance
Area	Red	0.62	± 0.05
Angle in	Blue	119.65	± 2.01°
Angle out	Green	136.08	± 2.61°
Roundness	Purple	0.68	± 0.04
Number of cells	-	8.8	-

Table 7.3: The experimental values measured in our set of images for repressor clones at 20 and 38 hours. Area are normalized by the area of cells $c + 2$. The tolerance corresponds to twice the standard error. For each feature, the color that is used to highlight the region of compatible parameters is given in the second column.

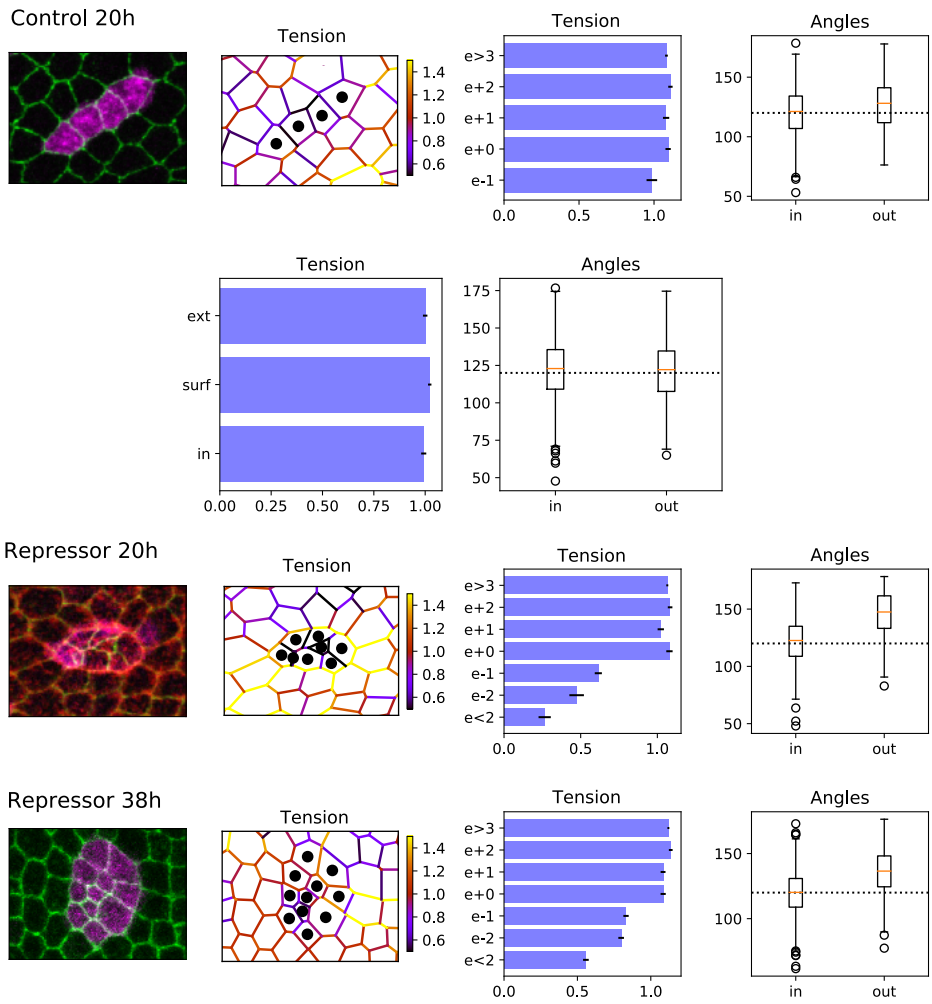

Figure 7.18: **Left:** Example of clones for the control case at 20 hours (**top**) and 38 hours (**middle top**) and the repressor case at 20 hours and (**middle bottom**) 38 hours (**bottom**). **Center left:** Vertex representation of the same clone with the edges colored by their inferred tension. **Center right:** Average of inferred tension for edges in different positions relative to the clone. In this situation, we observe how in both cases the tensions in the interior of the clone are lower than in the exterior. The surface has tension above the average for edges directly adjacent to the clone, but lower than edges far away from the clone. **Right:** Box plot of angles on the surface of the clone. The dotted line is at 120 degrees.

	c	Λ_s/Λ_0	Λ_c/Λ_0	T_s/T_0	T_i/T_0
Modeling 20h	4	0.75	1.5	1.16	1.00
Modeling 38h	8.8	0.5	1.5	1.19	1.04

Table 7.4: Numerical values for the parameter modeling the experimental repressor clones, and tensions in the surface T_s and in interior T_i relative to the tension T_0 in a regular cell.

ref. [Tsuboi et al., 2017]. The line tension associated with the clonal cells Λ_c does not appear to affect the roundness of the clone. A similar situation is found for the outward angle that becomes flattered when increasing the surface tension Λ_s, and is only weakly affected by changes in Λ_c (increasing Λ_c yield slightly flatter outward angles, by making the clonal cells smaller, and thereby reducing the tension of inner junctions). The internal angle gets flattered with increasing surface tension Λ_s as we might have expected, as can be seen in figure 7.19. The clonal area decreases when the surface tension Λ_s or the clonal cell line tension Λ_c increases. As expected, as we increase the number of cells, there is less compression for the same tension. The increase of clonal cell line tension Λ_c is comparable regardless of the strength of the cable of tension in the surface of the clone.

As it can be observed in figure 7.19, we can find a region that reproduces the geometry of the experimental clones for 20 hours and 38 hours. In both cases, as we expected, a cable of tension is suggested, as the values for surface line tension Λ_s are about 50% stronger in the clone. Also, the line tension Λ_c inside the clone is predicted to be higher than in WT cells. These two compressive forces together account for the observed reduction in area (from figure 7.19, if the compressive forces come only from the border, with an unchanged tension $\Lambda_c = \Lambda_0$ inside the clone, the model yields clones that are rounder than observed in experiments).

We observe a significantly higher tension for the tension in the boundary of the clone, and a slightly higher increase in the internal tension for 38h, and no increase at 20h (see table 7.4). Preliminar simulations with the pressure-less model presented in section 4.4 agree with the possible values for the tensions as well.

7.4.4 *No bias in the division is observed in the repressor case*

Similarly to what we found in the activator case, one could suspect that cells adjacent to repressor clones exhibit biased division. We should observe the same in the repressor case, especially, if we believe that the bias in the division is produced by problems in cell-to-cell communication, or the sensing of a cable of tension. However, our experimental collaborators reported that this bias was not observed for cells $c+1$ adjacent to the clone (see figure 7.21).

We do not have experimental measures in cells in the interior of the clone. In simulations, we observe that the cells $c+1$ adjacent to the clone do not have a particular orientation with respect to the surface of the clone, independently of the parameters, as shown in 7.22. Meanwhile, cells $c-1$ in the first layer of the clone are not aligned. This is consistent with what is found experimentally.

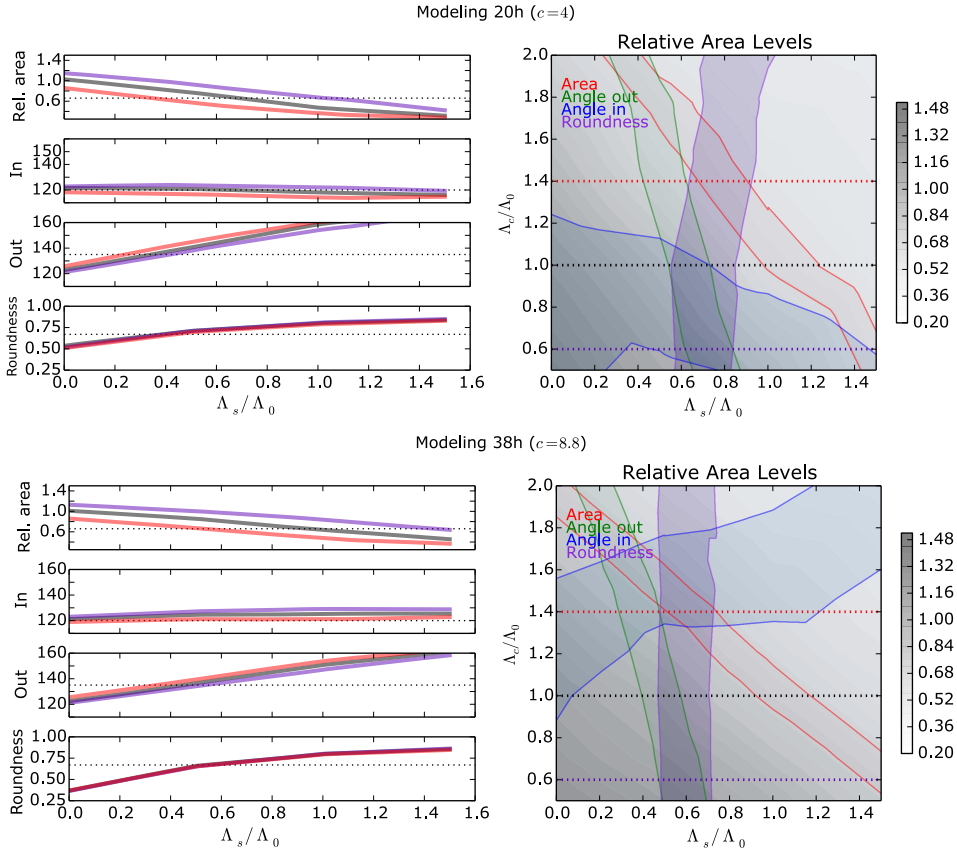

Figure 7.19: Parameter determination for repressor case clones. Contour plot of average relative areas for clonal cells as their line tension Λ_c varies in the vertical axis and the line tension Λ_s varies in the horizontal axis. The regions where the target geometrical features at 38 hours are inside the ranges defined in table 7.3 are highlighted with a semi-transparent color mask, in this case cell area (red), outward angle (green), internal angle (blue) and roundness (purple). **Top:** Clones at time $t = 2\tau_d$ when in average they have $c = 4.0$ as in our experimental images at 20 hours **Bottom:** Clones at time $t = 3.1\tau_d$ when in average they have $c = 8.8$ as in our experimental images at 38 hours.

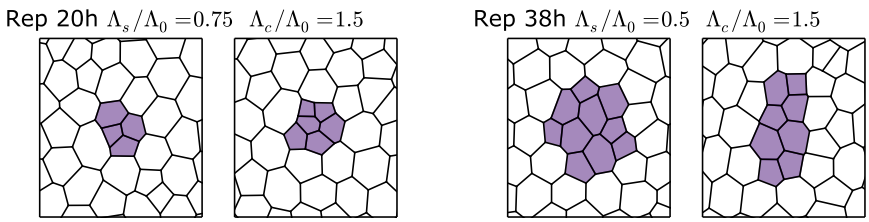

Figure 7.20: Examples of clones for the repressor case. **Left:** Modeling clones at 20h, the surface line tension is $\Lambda_s/\Lambda_0 = 0.75$, and the clone line tension $\Lambda_c/\Lambda_0 = 1.5$. **Right:** Modeling clones at 38h, the surface line tension is $\Lambda_s/\Lambda_0 = 0.5$, and the clone line tension $\Lambda_c/\Lambda_0 = 1.5$. In both cases, with $A_0 = \Gamma_c/\Gamma_0 = 1$.

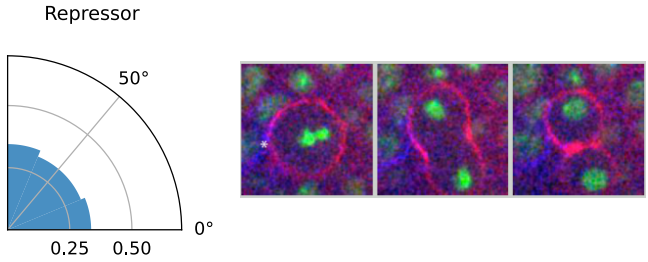

Figure 7.21: **Right:** Histogram of cell division orientation measured experimentally. **Left:** Example of division in the repressor case. In contrast to the activator case, cells $c+1$ adjacent to an ovo A clone do not exhibit bias in the direction of division.

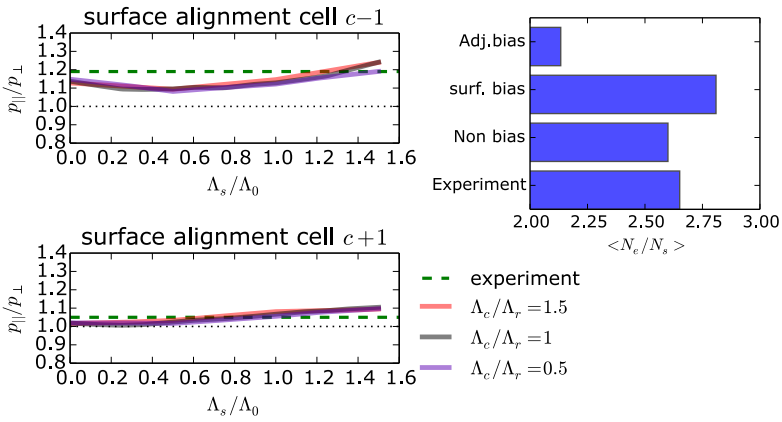

Figure 7.22: **Left:** Cell main axis projection over the clonal surface direction. On the **top left** the cells $c-1$ in the interior surface of the clone. On the **bottom left** WT cells adjacent to the clone surface $c+1$. No relevant differences can be found compared with experimental data (shown in green dashed lines). **Right:** Comparison of the average ratio between the number of edges and cells in the surface of the clone considering three cases: adjacent biased cells around the clone divide perpendicularly; surface biased cells in the surface of the clone divide perpendicularly against the surface when possible; and non-biased, compared with experiment. In the three cases, the clones are simulated with the parameters presented in figure 7.21, the surface line tension $\Lambda_s/\Lambda_0 = 0.5$, and the clone line tension $\Lambda_c/\Lambda_0 = 1.5$.

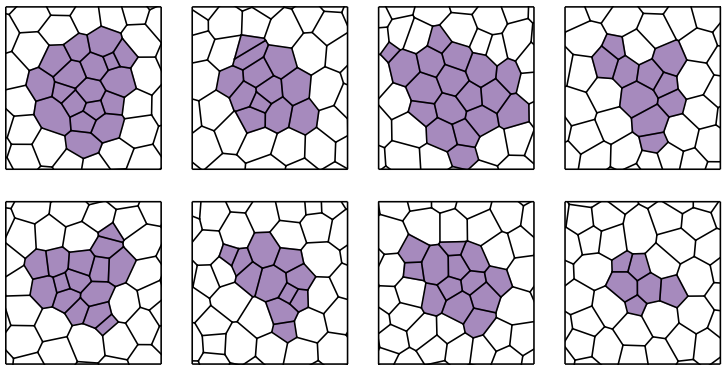

Figure 7.23: Examples of clones with bias division for clonal cells. The surface line tension is $\Lambda_s/\Lambda_0 = 0.5$, and the clone line tension $\Lambda_c/\Lambda_0 = 1.5$, modeling clones at 38h, but in this case the number of cells is $c = 12$ to better appreciate any effect.

We implemented bias in the division for cells inside the clone, by imposing a division that avoids the surface when possible, as clones with few cells may not allow it. Simulations with a bias in the division of cells in the interior of the clone do not show remarkably divergent features at first sight, as shown by the examples of figure 7.23. Moreover, they fail to reproduce the topology and angles, with fewer internal angles than experimental and non-biased clones, as displayed in the bottom right 7.21.

7.4.5 *Mean-field model for a clone of several cells*

In the previous chapter 6.3.1, we presented an approximation to address the case of a cluster of cells under a cable of tension. Here, we will apply it to our repressor clones at 38 hours, expanding it to consider clonal cells with a different line tension Λ_c. Equations for force equilibrium (6.20) and (6.21) are the same, but the partial tension associated with the clonal cell now depends on their line tension $T(A) = \Gamma\mu_6\sqrt{A} + \Lambda_c/2$.

$$0 = 2T_r - 2\cos\left(\frac{\gamma}{2}\right)[T_r + T(A) + \Lambda_s] - lK(A - A_r)\sin\left(\frac{\gamma}{2}\right), \tag{7.5}$$

$$0 = 2T(A) - 2\cos\left(\frac{\beta}{2}\right)[T_r + T(A) + \Lambda_s] + lK(A - A_r)\sin\left(\frac{\beta}{2}\right). \tag{7.6}$$

$$\tag{7.7}$$

where $l = \mu_6(\sqrt{A} + \sqrt{A_r})/12$. The equation for the clonal cells area again makes use of the roundness ρ obtained from simulations. The equilibrium area A^c_{eq} for clonal cells

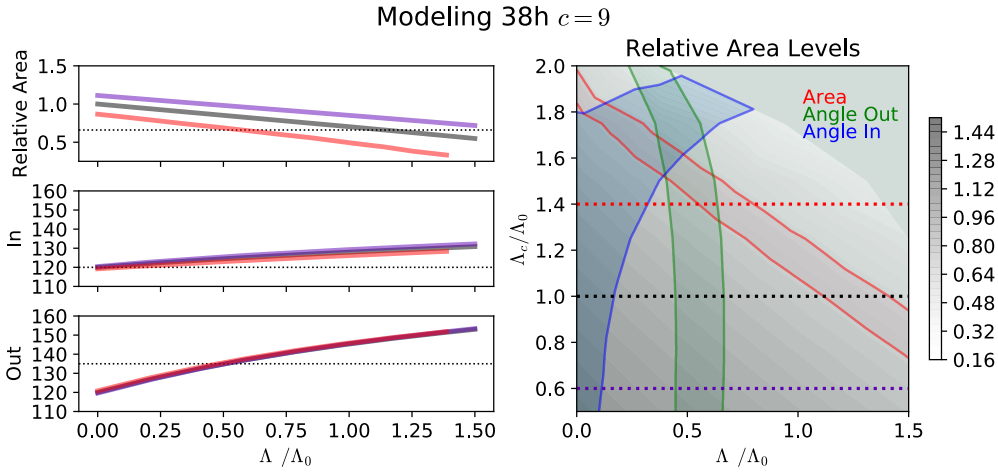

Figure 7.24: Contour plot of the regions where the target features satisfy our constrains, obtained from the mean-field approximation solving equations (7.8), (6.20), (6.21). The roundness for each parameter set has been obtained directly from simulations. In the gray region in the upper right of the contour plot the system of equation did not converge to a solution.

is obtained using equation (5.7) considering the new line tension Λ_c. The average and dispersion of area and perimeter found in WT cells is rescaled with A^c_{eq} to calculate the bulk modulus for the clone, B_c is now a function of the line tension Λ_c using equation (5.10). The new area equation reads,

$$\frac{\Lambda_s}{\sqrt{\rho} R_{eff}} = B_c(\Lambda_c)\left(1 - \frac{A}{A^c_{eq}}\right). \tag{7.8}$$

where the effective radius is $R_{eff} = \sqrt{cA/\pi}$. Solving equation (7.8) for the area A, and then the force equation (6.20) and (6.21) for the angles, leads to a good description of the clone. We not only recover the trends for the target features, but also find that the region in parameter space which reproduces the average geometry of our clones is very close to that found in our simulations, as can be seen by comparing figure 7.19 and figure 7.24.

If we use the model without any input from simulations, and instead make the approximation of considering perfectly round clones, i.e. $\rho = 1$, we still recover the trends for the diverse features. However, this overestimates the area and angles, as could be expected from our analysis in section 6.3.1.

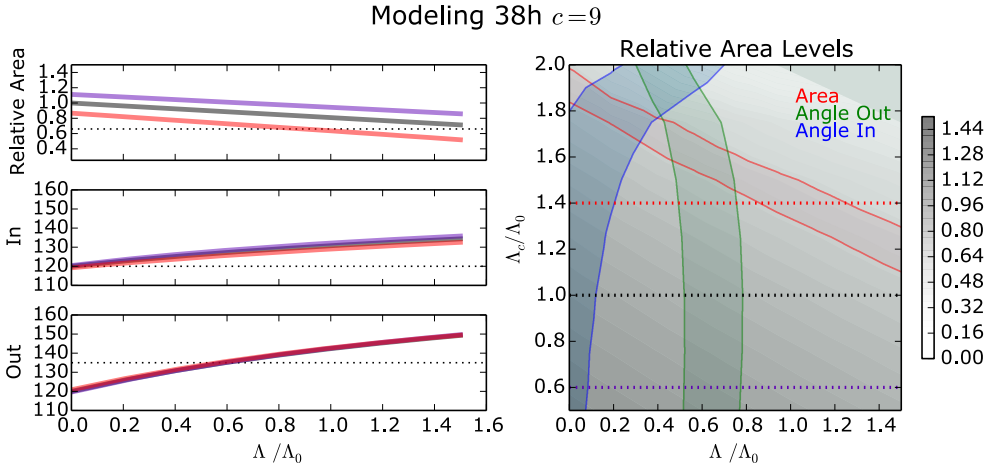

Figure 7.25: Contour plot of the regions where the target features satisfy our constrains, obtained from the mean-field approximation solving equations (7.8), (6.20), (6.21). The roundness is supposed to be $\rho = 1$, in contrast to the diagram in figure 7.24. In the gray region in the upper right of the contour plot the system of equation did not converge to a solution.

7.5 CONCLUSIONS

This chapter connected and applied the tools presented in the previous chapters with experiments performed by our collaborators. Both the repressor and activator cases show cells with distinctive geometrical features. The vertex models have been successfully used to describe the geometry, and even dynamics of epithelial tissues. Here, we applied it to describe a mechanically heterogeneous tissue with two types of cells.

This study had limitations: On the one hand, the vertex model neglects subtle aspects that may play a role, for instance, the already mentioned apoptosis, changes of mechanical properties over time, and differences in the rate of division between the two types of cells. These elements could be included in a more extensive study. Nevertheless, this should still leave another kind of limitation: the uncertainty in the estimation of cell geometry from experimental data (e.g. the imprecision in image segmentation). Features such as area or length are robust, but especially angles are sensible to imprecision. In spite of these limitations—our vertex model only included dissimilarities in proliferation rates and mechanical parameters—we found that we could reproduce the geometry observed in experiments and even predict unanticipated aspects, such as the bias in cell division in the activator case.

8 CONCLUSIONS

The vertex model captures multiple aspects of empirically observed tissue morphogenesis, including dynamical ones while remaining conceptually simple in that its only parameters are mechanical and geometry-dependent in origin (cell area elasticity and perimeter-dependent tensions) and constrained to a two-dimensional description. Furthering our understanding of the model thus contributes to deepening our comprehension of epithelial development. In this thesis, we extend the analysis of the vertex model and apply our approach to account for spatio-temporal features of epithelial morphogenesis in the presence of disorder and heterogeneity intrinsic to cell tissues.

In particular, we introduce a mean-field approximation, that describes the dynamics of cells based on their polygonal class. Cells are considered as regular polygons surrounded by n identical cells with a fixed area. This allows us to accurately predict the average area per polygonal class alongside the average dispersion of area and perimeter, as well as the bulk modulus of a tissue. The success of this approach is a non-trivial result, indicating how cells sense and average forces from their environment. Furthermore, our approach provides a powerful formal tool to investigate a wide array of features and properties of disordered tissues.

It is not obvious to translate concepts and relations used in continuous media and apply them to a discrete media, such as an epithelium. In addition to our study on pressure and bulk modulus in the vertex model, we show that the analog of Laplace's law is quite subtle in this discrete context. We found that the compression on a cluster of cells subjected to superficial tension involves diverse measures of the clone perimeter length (full or "coarse-grained") depending on which property is considered (global change in clone area or compression of inner clone cells).

Beyond exploring how disorder emerges and affect the property of a tissue with mechanically identical cells, we tackle the problem of modeling the effect of heterogeneity between cells. Indeed, this issue is crucial to understand healthy tissue development where diverse cells with various functions interact, as well as abnormal clonal cell growth as observed in tumors. Our mean-field approximation tackles the problem by taking advantage of the symmetry between different vertices, allowing us to write a force balance equation for each class of vertices and making use of other equilibrium equations to complete the set of equations if necessary (for instance our discrete Laplace's law).

We model a clone in which mechanics or proliferation rate differ from the surrounding environment, allowing us to unveil the role of each of these mechanistic ingredients. Moreover, taking into account topology as a function of cell mechanical parameters, the mean-field approximation successfully captures quantitative features of collective dynamics, especially in the limit of large numbers of cells.

These ideas were compared with experimental data, providing insight about the forces at play shaping clones. Our model predicted a biased cell division orientation around activator clones, which was confirmed experimentally. Additionally, that an increased surface tension, as predicted by our model, plays a crucial role in shaping both types of clones, activator and repressor, also appears supported by the observed accumulation of contractile material at the interface between WT and clonal cells.

A natural extension of this work is to further theoretically characterize the emergence of geometric order from forces and proliferation. On the one hand, some previous approaches [Gibson et al., 2006] only consider topology, neglecting cell rearrangements due to mechanical forces. Indeed, in chapter 4 we show that mechanical forces by themselves can largely account for empirical tissue geometry, even in the absence of cell division. However, in addition to topology, mechanical forces arising from rearrangements have also been highlighted to bias the direction of cell division axes [Finegan et al., 2019,Scarpa et al., 2018]. A theoretical approach that integrates both forces and topology will have to be developed to provide a complete theoretical description of planar epithelium, in particular when heterogeneous cells interact.

In summary, the work reported in this thesis provides a theoretical and computational basis that may be elaborated upon, to unveil the mechanisms that allow the complex yet robust cellular self-organization from which life emerges.

Part III

APPENDIX

A NUMERICAL SIMULATION

A.1 NUMERICAL INTEGRATION

The software to run numerical simulations on tissue development was programmed in Python, with the use of the standard libraries (Numpy, Scipy, and Matplotlib). Bellow you can find details on the numerical functions used to simulate the tissue

A.1.1 *Computation of forces*

All terms in the work function are derived from the position of the vertices. From the work function, the force over one vertex i has two parts, one that depends on the area of the cells around F_P^i, and the other that depends on the edges F_T^i. Let us start defining the force associated with cell area,

$$\vec{F}_P^i = \sum_{cell} [K(A_c - A_0^c)\nabla_i A_c] \tag{A.1}$$

The summation runs over the cells of the tissue. The preferred area per cell A_0^c has an index given that in many cases we will choose a different value regarding if the cell c has been chosen as being a different cell class. The cell area given the position of its vertices $\{x_i\hat{x} + y_i\hat{y}\}$ can be calculated using Green's theorem,

$$A = \frac{1}{2} \sum_{i:\text{vertices}} (x_i + x_{i+1})(y_i - y_{i+1}) \tag{A.2}$$

With the indexes i numbered in counter-clockwise fashion. Therefore, the derivative of the area respect the position of one of its vertices i yields,

$$\nabla_i A = \frac{1}{2} [(y_{i-1} - y_{i+1})\hat{x}_i - (x_{i-1} - x_{i+1})\hat{y}_i] \tag{A.3}$$

On the other hand, the forces associated with the edges F_T^i are given by

$$\vec{F}_T^i = \sum_{edge} \left[\Gamma \left(p_e^{(1)} + p_e^{(2)}\right) + \Lambda_e(1 + \zeta_e(t))\right] \hat{e}_i \tag{A.4}$$

The summation over the edges. $p_e^{(1)}$ and $p^{(2)}$ denote the perimeters of the cells that the edge e delimit, and $\hat{e}_i$ is the unitary vector in the direction of the edge e away from the vertex i. The perimeter is simply computed by adding the lengths of all the edges that compose the cell. Λ_e has an index given that in many cases we will select a different value regarding its position. The value of $\zeta_e(t)$, that represents the fluctuations in the

tension of each edge, is computed in parallel solving numerically the following Itô's stochastic differential equation with a discrete time step δt,

$$\zeta_e(t+\delta t) - \zeta_e(t) = -\zeta_e(t)\frac{\delta t}{\tau} + \eta_0\sqrt{\frac{2\delta t}{\tau}}z(t) \tag{A.5}$$

where $z(t)$ is a gaussian random variable, with average $\langle z(t)\rangle = 0$ and normalized correlation $\langle z(t), z(t')\rangle = \delta(t-t')$. This is the numerical implementation of an Ornstein-Uhlenbeck process with characteristic time τ and $\langle \zeta_e(t), \zeta_e(t')\rangle = \eta_0 \exp(-|t-t'|/\tau)$.

The total force is then computed adding up this two equations (A.1) and (A.4), $\vec{F}_i = \vec{F}_P^i + \vec{F}_T^i$. Then, each vertex is displaced proportionally to this force using a discrete time step δt

$$\vec{v}_i(t+\delta t) - \vec{v}_i(t) = \vec{F}_i \delta t \tag{A.6}$$

The table A.1 shows the particular value for the parameters in equations (A.1) and (A.4).

	K	A_0		τ	δt
Value	1	1		3.9	0.02
Cases	Λ	Γ	η_0		
Case A	0.12	0.04	0.3		
Case B	0.0	0.1	0.0413		
Case C	-0.32	0.04	0.002		

Table A.1: Numerical values of mechanical parameters used by default in the simulations. Three pairs of values have been used for Λ and Γ and their values are specified. But unless it is clearly stated otherwise, the values used correspond to Case A.

A.1.2 *Neighbor exchange and apoptosis*

The length of each edge is checked in each step; if the length goes below a critical value L_{crit}, the edge is rotated perpendicularly to the original configuration. If the energy decreases, the change is accepted.

In simulations where apoptosis is implemented, cells that become smaller than A_{crit} are removed by collapsing them to a vertex. If the cell in the moment of collapse had more than three sides, edges of zero-length are created to keep each vertex associated with only three edges.

	A_{crit}	L_{crit}
Value	0.01	0.01

Table A.2: Critical values for cell area before remove it by apoptosis, and for edge length before testing for a T1 transition.

A.1.3 *Cell division*

To implement cell division, each cell keeps an internal clock from the last division t_c, and a time when the division will occur τ_c, that is assigned when the cell is created. When the internal time t_c arrives at τ_c, the cell divides, adding a new edge that divides the cell in two, creating two new daughter cells. The values for τ_c are normally distributed, and they have averaged $\tau_{div} = \langle \tau_c \rangle$ and dispersion σ_τ. The table A.3 we present the default values for τ_{div} and σ_τ.

Cell division follows Hertwig's rule presented in the introduction section. The case of biased division is explained in chapter 7.

	τ_d	σ/τ_d
Value	60	0.2

Table A.3: Default time parameters for cell division.

A.1.4 *Periodic boundary conditions*

Simulations are performed with periodic boundary conditions. A box of dimensions $L_x \times L_y$ is defined, and distances between two points are computed using an auxiliary function defined as follows.

$$d(x, L) = \begin{cases} x & \text{if } 2|x| < L \\ \operatorname{sgn}(x)\,(|x| - L) & \text{otherwise} \end{cases} \tag{A.7}$$

The distance D between two points $v = (x, y)$ and $v' = (x', y')$ reads as follows,

$$D = \sqrt{d^2(x - x', L_x) + d^2(y - y', L_y)} \tag{A.8}$$

And a vector u pointing from the point v' to the point v,

$$u = (d(x - x', L_x), d(y - y', L_y)) \tag{A.9}$$

To compute the area of a cell or other functions that involve a series of points, they are all rewritten using coordinates in respect of one point in the list.

A.1.5 *Dynamical adjustment of the box size*

As the number of cells increases due to successive cell divisions, the size of the box needs changes.

From the work of [Batchelor, 1970], the stress tensor N can be evaluated for a large group of cells using the following expression [Ishihara and Sugimura, 2012],

$$\mathbf{N} = \frac{1}{\sum_c A_c}\left[-\sum_c A_c P_c \mathbf{I}_2 + \sum_e T_e \frac{\vec{l}_e \otimes \vec{l}_e}{|l_e|}\right] \tag{A.10}$$

This matrix can be used to relax the box dimentions. The diagonal elements determine the relative change of scale,

$$\frac{d\lambda_x}{dt} = N_{xx} \tag{A.11}$$

$$\frac{d\lambda_y}{dt} = N_{yy} \tag{A.12}$$

where the total length of the box is $L_x = \lambda_x L_x^0$ and $L_y = \lambda_y L_y^0$. Here, our implementatios follow the procedure found in [Sugimura and Ishihara, 2013].

A.1.6 *Poisson initialization of the tissue*

The tissue is initialized by N_c random points $c_i = (x_i, y_i)$ generated by a uniform distribution $x_i \in [0, L_x[$ and $y_i \in [0, L_y[$, that define Voronoi cells, that are the original state of the tissue.

A.1.7 *Inertia matrix and main axis calculation*

In several analyses of a simulation, the main axis of the cells is computed. The main axis is computed as the eigenvector associated with the biggest eigenvalue of the second moment of area matrix,

$$I = \begin{pmatrix} I_x & I_{xy} \\ I_{xy} & I_y \end{pmatrix} \tag{A.13}$$

where its elements are defined as,

$$I_y = \frac{1}{12}\sum_{i=1}^{n}\left(x_i y_{i+1} - x_{i+1} y_i\right)\left(x_i^2 + x_i x_{i+1} + x_{i+1}^2\right) \tag{A.14}$$

$$I_x = \frac{1}{12}\sum_{i=1}^{n}\left(x_i y_{i+1} - x_{i+1} y_i\right)\left(y_i^2 + y_i y_{i+1} + y_{i+1}^2\right) \tag{A.15}$$

$$I_{xy} = \frac{1}{24}\sum_{i=1}^{n}\left(x_i y_{i+1} - x_{i+1} y_i\right)\left(x_i y_{i+1} + 2x_i y_i + 2x_{i+1} y_{i+1} + x_{i+1} y_i\right) \tag{A.16}$$

The following operation defines the projection p of the main axis over a vector $\vec{v}$,

$$p = \vec{v}^T I \vec{v}, \tag{A.17}$$

A.2 SIMULATIONS CHAPTER 7

We performed simulations in a grid of points, with 120 clones per set of parameters, and then the target features are averaged over each of them. Linear interpolation is used to estimate the values of the target features between points in the grid.

For **activator case**, the grid is generated by combining,

$$A_0^c \in \{0.8, 1.0, 1.2, 1.3, 1.4, 1.6\}$$
$$\Lambda_c/\Lambda_0 \in \{1.0, 1.25, 1.5, 1.75\}$$

For **repressor case**, the grid is generated by combining,

$$\Lambda_s/\Lambda_0 \in \{1.0, 1.125, 1.25, 1.375, 1.5\}$$
$$\Lambda_c/\Lambda_0 \in \{0.75, 1.0, 1.25, 1.5, 1.75, 2.0\}$$

BIBLIOGRAPHY

[Aegerter-Wilmsen et al., 2010] Aegerter-Wilmsen, T., Smith, A. C., Christen, A. J., Aegerter, C. M., Hafen, E., and Basler, K. (2010). Exploring the effects of mechanical feedback on epithelial topology. Development, 137(3):499–506.

[Angelini et al., 2011] Angelini, T. E., Hannezo, E., Trepat, X., Marquez, M., Fredberg, J. J., and Weitz, D. A. (2011). Glass-like dynamics of collective cell migration. Proceedings of the National Academy of Sciences, 108(12):4714–4719.

[Atia et al., 2018] Atia, L., Bi, D., Sharma, Y., Mitchel, J. A., Gweon, B., Koehler, S. A., DeCamp, S. J., Lan, B., Kim, J. H., Hirsch, R., et al. (2018). Geometric constraints during epithelial jamming. Nature physics, 14(6):613.

[Bard, 1981] Bard, J. B. (1981). A model for generating aspects of zebra and other mammalian coat patterns. Journal of Theoretical Biology, 93(2):363–385.

[Bardet et al., 2013] Bardet, P.-L., Guirao, B., Paoletti, C., Serman, F., Léopold, V., Bosveld, F., Goya, Y., Mirouse, V., Graner, F., and Bellaïche, Y. (2013). Pten controls junction lengthening and stability during cell rearrangement in epithelial tissue. Developmental cell, 25(5):534–546.

[Batchelor, 1970] Batchelor, G. (1970). Slender-body theory for particles of arbitrary cross-section in stokes flow. Journal of Fluid Mechanics, 44(3):419–440.

[Berthier and Kurchan, 2013] Berthier, L. and Kurchan, J. (2013). Non-equilibrium glass transitions in driven and active matter. Nature Physics, 9(5):310.

[Bi et al., 2015] Bi, D., Lopez, J., Schwarz, J. M., and Manning, M. L. (2015). A density-independent rigidity transition in biological tissues. Nature Physics, 11(12):1074.

[Bi et al., 2014] Bi, D., Lopez, J. H., Schwarz, J., and Manning, M. L. (2014). Energy barriers and cell migration in densely packed tissues. Soft matter, 10(12):1885–1890.

[Blair, 2007] Blair, S. S. (2007). Wing vein patterning in drosophila and the analysis of intercellular signaling. Annu. Rev. Cell Dev. Biol., 23:293–319.

[Blankenship et al., 2006] Blankenship, J. T., Backovic, S. T., Sanny, J. S., Weitz, O., and Zallen, J. A. (2006). Multicellular rosette formation links planar cell polarity to tissue morphogenesis. Developmental cell, 11(4):459–470.

[Bonnet et al., 2012] Bonnet, I., Marcq, P., Bosveld, F., Fetler, L., Bellaïche, Y., and Graner, F. (2012). Mechanical state, material properties and continuous description of an epithelial tissue. Journal of The Royal Society Interface, 9(75):2614–2623.

[Bosveld et al., 2016a] Bosveld, F., Guirao, B., Wang, Z., Rivière, M., Bonnet, I., Graner, F., and Bellaïche, Y. (2016a). Modulation of junction tension by tumor suppressors and proto-oncogenes regulates cell-cell contacts. Development, 143(4):623–634.

[Bosveld et al., 2016b] Bosveld, F., Markova, O., Guirao, B., Martin, C., Wang, Z., Pierre, A., Balakireva, M., Gaugue, I., Ainslie, A., Christophorou, N., et al. (2016b). Epithelial tricellular junctions act as interphase cell shape sensors to orient mitosis. Nature.

[Breakspear et al., 2010] Breakspear, M., Heitmann, S., and Daffertshofer, A. (2010). Generative models of cortical oscillations: Neurobiological implications of the kuramoto model. Frontiers in Human Neuroscience, 4:190.

[Brodland et al., 2014] Brodland, G. W., Veldhuis, J. H., Kim, S., Perrone, M., Mashburn, D., and Hutson, M. S. (2014). Cellfit: a cellular force-inference toolkit using curvilinear cell boundaries. PloS one, 9(6):e99116.

[Cadart et al., 2018] Cadart, C., Monnier, S., Grilli, J., Sáez, P. J., Srivastava, N., Attia, R., Terriac, E., Baum, B., Cosentino-Lagomarsino, M., and Piel, M. (2018). Size control in mammalian cells involves modulation of both growth rate and cell cycle duration. Nature communications, 9(1):3275.

[Carroll, 2005] Carroll, S. B. (2005). Endless forms most beautiful: The new science of evo devo and the making of the animal kingdom. Number 54. WW Norton & Company.

[Chanut-Delalande et al., 2014] Chanut-Delalande, H., Hashimoto, Y., Pelissier-Monier, A., Spokony, R., Dib, A., Kondo, T., Bohère, J., Niimi, K., Latapie, Y., Inagaki, S., et al. (2014). Pri peptides are mediators of ecdysone for the temporal control of development. Nature cell biology, 16(11):1035.

[Chiou et al., 2012] Chiou, K. K., Hufnagel, L., and Shraiman, B. I. (2012). Mechanical stress inference for two dimensional cell arrays. PLOS Computational Biology, 8(5):1–9.

[Chiu, 1995] Chiu, S. (1995). Aboav-weaire's and lewis' laws—a review. Materials characterization, 34(2):149–165.

[Classen et al., 2005] Classen, A.-K., Anderson, K. I., Marois, E., and Eaton, S. (2005). Hexagonal packing of drosophila wing epithelial cells by the planar cell polarity pathway. Developmental cell, 9(6):805–817.

[Corson et al., 2017] Corson, F., Couturier, L., Rouault, H., Mazouni, K., and Schweisguth, F. (2017). Self-organized notch dynamics generate stereotyped sensory organ patterns in drosophila. Science, 356(6337):eaai7407.

[de Celis, 2003] de Celis, J. F. (2003). Pattern formation in the drosophila wing: the development of the veins. Bioessays, 25(5):443–451.

[Delon et al., 2003] Delon, I., Chanut-Delalande, H., and Payre, F. (2003). The ovo/shavenbaby transcription factor specifies actin remodelling during epidermal differentiation in drosophila. Mechanisms of development, 120(7):747–758.

[Doyle, 2001] Doyle, J. (2001). Computational biology: Beyond the spherical cow. Nature, 411(6834):151.

[Edgar and O'Farrell, 1989] Edgar, B. A. and O'Farrell, P. H. (1989). Genetic control of cell division patterns in the drosophila embryo. Cell, 57(1):177–187.

[Edgar and O'Farrell, 1990] Edgar, B. A. and O'Farrell, P. H. (1990). The three postblastoderm cell cycles of drosophila embryogenesis are regulated in g2 by string. Cell, 62(3):469–480.

[Euler, 1970] Euler, L. (1970). A general investigation into the mortality and multiplication of the human species. Theoretical Population Biology, 1(3):307–314.

[Farhadifar et al., 2007] Farhadifar, R., Röper, J.-C., Aigouy, B., Eaton, S., and Jülicher, F. (2007). The influence of cell mechanics, cell-cell interactions, and proliferation on epithelial packing. Current Biology, 17(24):2095–2104.

[Fernandez-Gonzalez et al., 2009] Fernandez-Gonzalez, R., de Matos Simoes, S., Röper, J.-C., Eaton, S., and Zallen, J. A. (2009). Myosin ii dynamics are regulated by tension in intercalating cells. Developmental cell, 17(5):736–743.

[Finegan et al., 2019] Finegan, T. M., Na, D., Cammarota, C., Skeeters, A. V., Nádasi, T. J., Dawney, N. S., Fletcher, A. G., Oakes, P. W., and Bergstralh, D. T. (2019). Tissue tension and not interphase cell shape determines cell division orientation in the drosophila follicular epithelium. The EMBO journal, 38(3).

[Fletcher et al., 2013] Fletcher, A. G., Osborne, J. M., Maini, P. K., and Gavaghan, D. J. (2013). Implementing vertex dynamics models of cell populations in biology within a consistent computational framework. Progress in biophysics and molecular biology, 113(2):299–326.

[Giardina, 2008] Giardina, I. (2008). Collective behavior in animal groups: theoretical models and empirical studies. HFSP journal, 2(4):205–219.

[Gibson et al., 2006] Gibson, M. C., Patel, A. B., Nagpal, R., and Perrimon, N. (2006). The emergence of geometric order in proliferating metazoan epithelia. Nature, 442(7106):1038.

[Graner and Glazier, 1992] Graner, F. and Glazier, J. A. (1992). Simulation of biological cell sorting using a two-dimensional extended potts model. Physical review letters, 69(13):2013.

[Gregor et al., 2007] Gregor, T., Tank, D. W., Wieschaus, E. F., and Bialek, W. (2007). Probing the limits to positional information. Cell, 130(1):153–164.

[Hayashi and Carthew, 2004] Hayashi, T. and Carthew, R. W. (2004). Surface mechanics mediate pattern formation in the developing retina. Nature, 431(7009):647.

[Heisenberg and Bellaïche, 2013] Heisenberg, C.-P. and Bellaïche, Y. (2013). Forces in tissue morphogenesis and patterning. Cell, 153(5):948–962.

[Henkes et al., 2011] Henkes, S., Fily, Y., and Marchetti, M. C. (2011). Active jamming: Self-propelled soft particles at high density. Physical Review E, 84(4):040301.

[Hertwig, 1884] Hertwig, O. (1884). Untersuchungen zur morphologie und physiologie der Zelle: das Problem der Befruchtung und der Isotropie des Eies, eine Theorie der Vererbung, volume 3. Fischer.

[Hoffman et al., 2006] Hoffman, B. D., Massiera, G., Van Citters, K. M., and Crocker, J. C. (2006). The consensus mechanics of cultured mammalian cells. Proceedings of the National Academy of Sciences, 103(27):10259–10264.

[Hufnagel et al., 2007] Hufnagel, L., Teleman, A. A., Rouault, H., Cohen, S. M., and Shraiman, B. I. (2007). On the mechanism of wing size determination in fly development. Proceedings of the National Academy of Sciences, 104(10):3835–3840.

[Ishihara and Sugimura, 2012] Ishihara, S. and Sugimura, K. (2012). Bayesian inference of force dynamics during morphogenesis. Journal of Theoretical Biology, 313:201 – 211.

[Ishihara et al., 2013] Ishihara, S., Sugimura, K., Cox, S., Bonnet, I., Bellaiche, Y., and Graner, F. (2013). Comparative study of non-invasive force and stress inference methods in tissue. The European Physical Journal E, 36(4):45.

[Iyengar, 2012] Iyengar, B. (2012). The organization of drosophila wing epithelial cells after wing inflation.

[Kondo et al., 2010] Kondo, T., Plaza, S., Zanet, J., Benrabah, E., Valenti, P., Hashimoto, Y., Kobayashi, S., Payre, F., and Kageyama, Y. (2010). Small peptides switch the transcriptional activity of shavenbaby during drosophila embryogenesis. Science, 329(5989):336–339.

[Larsen et al., 2003] Larsen, C. W., Hirst, E., Alexandre, C., and Vincent, J.-P. (2003). Segment boundary formation in drosophila embryos. Development, 130(23):5625–5635.

[Lebowitz and Rubinow, 1974] Lebowitz, J. and Rubinow, S. (1974). A theory for the age and generation time distribution of a microbial population. Journal of Mathematical Biology, 1(1):17–36.

[Li et al., 2012] Li, Y., Naveed, H., Kachalo, S., Xu, L. X., and Liang, J. (2012). Mechanisms of regulating cell topology in proliferating epithelia: impact of division plane, mechanical forces, and cell memory. PLoS One, 7(8):e43108.

[Liang et al., 2016] Liang, X., Michael, M., and Gomez, G. A. (2016). Measurement of mechanical tension at cell-cell junctions using two-photon laser ablation. Bio-protocol, 6(24).

[Lotka, 1907] Lotka, A. J. (1907). Relation between birth rates and death rates. Science, 26(653):21–22.

[Lu et al., 2006] Lu, Y.-B., Franze, K., Seifert, G., Steinhäuser, C., Kirchhoff, F., Wolburg, H., Guck, J., Janmey, P., Wei, E.-Q., Käs, J., et al. (2006). Viscoelastic properties of individual glial cells and neurons in the cns. Proceedings of the National Academy of Sciences, 103(47):17759–17764.

[Ma et al., 2009] Ma, X., Lynch, H. E., Scully, P. C., and Hutson, M. S. (2009). Probing embryonic tissue mechanics with laser hole drilling. Physical biology, 6(3):036004.

[Mao et al., 2013] Mao, Y., Tournier, A. L., Hoppe, A., Kester, L., Thompson, B. J., and Tapon, N. (2013). Differential proliferation rates generate patterns of mechanical tension that orient tissue growth. The EMBO journal, 32(21):2790–2803.

[Martin et al., 2010] Martin, A. C., Gelbart, M., Fernandez-Gonzalez, R., Kaschube, M., and Wieschaus, E. F. (2010). Integration of contractile forces during tissue invagination. The Journal of cell biology, 188(5):735–749.

[Mayr, 1970] Mayr, E. (1970). Populations, species, and evolution: an abridgment of animal species and evolution, volume 19. Harvard University Press.

[Meinhardt, 2009] Meinhardt, H. (2009). The algorithmic beauty of sea shells. Springer Science & Business Media.

[Murisic et al., 2015] Murisic, N., Hakim, V., Kevrekidis, I. G., Shvartsman, S. Y., and Audoly, B. (2015). From discrete to continuum models of three-dimensional deformations in epithelial sheets. Biophysical journal, 109(1):154–163.

[Nagai and Honda, 2006] Nagai, T. and Honda, H. (2006). Wound healing mechanism in epithelial tissues cell adhesion to basal lamina. WSEAS Transactions on Biology and Biomedicine, 3(6):389.

[Narimatsu et al., 2009] Narimatsu, M., Bose, R., Pye, M., Zhang, L., Miller, B., Ching, P., Sakuma, R., Luga, V., Roncari, L., Attisano, L., et al. (2009). Regulation of planar cell polarity by smurf ubiquitin ligases. Cell, 137(2):295–307.

[Nelson, 2018] Nelson, C. M. (2018). Epithelial packing: Even the best of friends must part. Current Biology, 28(20):R1197–R1200.

[Osborne et al., 2010] Osborne, J. M., Walter, A., Kershaw, S., Mirams, G., Fletcher, A., Pathmanathan, P., Gavaghan, D., Jensen, O., Maini, P., and Byrne, H. (2010). A hybrid approach to multi-scale modelling of cancer. Philosophical Transactions of the Royal Society A: Mathematical, Physical and Engineering Sciences, 368(1930):5013–5028.

[Painter and Marr, 1968] Painter, P. and Marr, A. (1968). Mathematics of microbial populations. Annual Reviews in Microbiology, 22(1):519–548.

[Pak and Gilbert, 1987] Pak, M. D. and Gilbert, L. I. (1987). A developmental analysis of ecdysteroids during the metamorphosis of drosophila melanogaster. Journal of Liquid Chromatography, 10(12):2591–2611.

[Park et al., 2005] Park, S., Koch, D., Cardenas, R., Käs, J., and Shih, C.-K. (2005). Cell motility and local viscoelasticity of fibroblasts. Biophysical journal, 89(6):4330–4342.

[Payre et al., 1999] Payre, F., Vincent, A., and Carreno, S. (1999). ovo/svb integrates wingless and der pathways to control epidermis differentiation. Nature, 400(6741):271.

[Petkova et al., 2019] Petkova, M. D., Tkačik, G., Bialek, W., Wieschaus, E. F., and Gregor, T. (2019). Optimal decoding of cellular identities in a genetic network. Cell, 176(4):844–855.

[Pinheiro et al., 2017] Pinheiro, D., Hannezo, E., Herszterg, S., Bosveld, F., Gaugue, I., Balakireva, M., Wang, Z., Cristo, I., Rigaud, S. U., Markova, O., et al. (2017). Transmission of cytokinesis forces via e-cadherin dilution and actomyosin flows. Nature, 545(7652):103.

[Ranft et al., 2010] Ranft, J., Basan, M., Elgeti, J., Joanny, J.-F., Prost, J., and Jülicher, F. (2010). Fluidization of tissues by cell division and apoptosis. Proceedings of the National Academy of Sciences, 107(49):20863–20868.

[Raspopovic et al., 2014] Raspopovic, J., Marcon, L., Russo, L., and Sharpe, J. (2014). Digit patterning is controlled by a bmp-sox9-wnt turing network modulated by morphogen gradients. Science, 345(6196):566–570.

[Sahlin and Jönsson, 2010] Sahlin, P. and Jönsson, H. (2010). A modeling study on how cell division affects properties of epithelial tissues under isotropic growth. PloS one, 5(7):e11750.

[Scarpa et al., 2018] Scarpa, E., Finet, C., Blanchard, G. B., and Sanson, B. (2018). Actomyosin-driven tension at compartmental boundaries orients cell division independently of cell geometry in vivo. Developmental cell, 47(6):727–740.

[Schoetz et al., 2013] Schoetz, E.-M., Lanio, M., Talbot, J. A., and Manning, M. L. (2013). Glassy dynamics in three-dimensional embryonic tissues. Journal of The Royal Society Interface, 10(89):20130726.

[Schweisguth and Corson, 2019] Schweisguth, F. and Corson, F. (2019). Self-organization in pattern formation. Developmental cell, 49(5):659–677.

[Sepúlveda et al., 2013] Sepúlveda, N., Petitjean, L., Cochet, O., Grasland-Mongrain, E., Silberzan, P., and Hakim, V. (2013). Collective cell motion in an epithelial sheet can be quantitatively described by a stochastic interacting particle model. PLoS computational biology, 9(3):e1002944.

[Soulard et al., 2019] Soulard, M., Pélissier-Monier, A., Contreras, D.-A., Hakim, V., Corson, F., Mangeat, T., Ronsin, B., Marques, S., and Payre, F. (2019). In preparation.

[Springer Verlag GmbH, European Mathematical Society,] Springer Verlag GmbH, European Mathematical Society. Encyclopedia of Mathematics. Website. URL: `https://www.encyclopediaofmath.org/index.php?title=Euler_characteristic`. Accessed on 2019-07-01.

[Staddon et al., 2018] Staddon, M. F., Bi, D., Tabatabai, A. P., Ajeti, V., Murrell, M. P., and Banerjee, S. (2018). Cooperation of dual modes of cell motility promotes epithelial stress relaxation to accelerate wound healing. PLoS computational biology, 14(10):e1006502.

[Sugimura and Ishihara, 2013] Sugimura, K. and Ishihara, S. (2013). The mechanical anisotropy in a tissue promotes ordering in hexagonal cell packing. Development, 140(19):4091–4101.

[Tardieu and Delaye, 1988] Tardieu, A. and Delaye, M. (1988). Eye lens proteins and transparency: from light transmission theory to solution x-ray structural analysis. Annual review of biophysics and biophysical chemistry, 17(1):47–70.

[Tkačik et al., 2015] Tkačik, G., Dubuis, J. O., Petkova, M. D., and Gregor, T. (2015). Positional information, positional error, and readout precision in morphogenesis: a mathematical framework. Genetics, 199(1):39–59.

[Tsuboi et al., 2018] Tsuboi, A., Ohsawa, S., Umetsu, D., Sando, Y., Kuranaga, E., Igaki, T., and Fujimoto, K. (2018). Competition for space is controlled by apoptosis-induced change of local epithelial topology. Current Biology, 28(13):2115–2128.

[Tsuboi et al., 2017] Tsuboi, A., Umetsu, D., Kuranaga, E., and Fujimoto, K. (2017). Inference of cell mechanics in heterogeneous epithelial tissue based on multivariate clone shape quantification. Frontiers in Cell and Developmental Biology, 5:68.

[Turing, 1990] Turing, A. M. (1990). The chemical basis of morphogenesis. Bulletin of mathematical biology, 52(1-2):153–197.

[Vicsek et al., 1995] Vicsek, T., Czirók, A., Ben-Jacob, E., Cohen, I., and Shochet, O. (1995). Novel type of phase transition in a system of self-driven particles. Phys. Rev. Lett., 75:1226–1229.

[Weaire and Rivier, 1984] Weaire, D. and Rivier, N. (1984). Soap, cells and statistics—random patterns in two dimensions. Contemporary Physics, 25(1):59–99.

[Wei and Yang, 2016] Wei, S. C. and Yang, J. (2016). Forcing through tumor metastasis: the interplay between tissue rigidity and epithelial–mesenchymal transition. Trends in cell biology, 26(2):111–120.

[Wolpert et al., 2011] Wolpert, L., Tickle, C., and Arias, A. M. (2011). Principles of development. Oxford University Press, USA.

[Yamanaka et al., 2013] Yamanaka, N., Rewitz, K. F., and O'Connor, M. B. (2013). Ecdysone control of developmental transitions: lessons from drosophila research. Annual review of entomology, 58:497–516.

RÉSUMÉ

Les tissus épithéliaux sont ubiquitaires dans les organismes vivants, couvrant des surfaces et séparant différents compartiments dans divers organes et espèces. L'épithélium est le premier tissu qui apparaît au cours du développement et il joue un rôle central pour en structurer les étapes. Dans ce processus complexe, les interactions entre les divisions cellulaires, la signalisation chimique et les forces mécaniques permettent l'émergence de différents tissus avec des fonctions diverses.

Dans l'élucidation des mécanismes en jeu dans la mécanique des tissusépithéliaux, un outil utile est constitué par les modèles de vertex, dans lesquels les cellules sont représentées de façon simplifiée par des polygones. La simulation de la division cellulaire dans ces modèles, produit des tissus avec des cellules géométriquement irrégulières, semblablesà celles observées dans lesépithéliums naturels, même quand les propriétés mécaniques des différentes cellules sont identiques. Les analyses théoriques existantes sont cependant, pour la plupart, confinées aux réseaux réguliers hexagonaux.

Dans ce travail, nous proposons une analyse théorique d'un modèle de vertex géométriquement désordonné. Nous commençons par quantifier à l'aide de simulations numériques, les propriétés géométriques et mécaniques des cellules, dans des tissus désordonnés produits par différentes règles de division cellulaires ou simplement par la relaxation en présence de bruit. Nous développons ensuite une analyse simple de type

Finalement, en collaboration avec le groupe de F. Payre (Université de Toulouse), nous appliquons cette analyse pour décrire la géométrie et la dynamique des divisions cellulaire au cours de la différenciation de l'epiderme de la mouche. Nous nous attachons particulièrement à caractériser les propriétés mécaniques d'un clone de cellules qui prolifère différemment du tissu environnant.

MOTS CLÉS

morphogenèse, mécanique, tissus épithéliaux, mécanique statistique.

ABSTRACT

Epithelial tissues are ubiquitous in animal life, covering surfaces and separating body compartments in diverse organs and species. Epithelium is the first tissue to form, playing a key role in structuring the intricate steps of an organism's development. In such a complex system, the interplay between cell division, chemical signaling, and mechanical forces permits the emergence of different tissues with specific functions.

To uncover the mechanisms at play in epithelial tissue mechanics, a useful tool is provided by vertex models, in which cells are idealized as juxtaposed polygons. Numerical simulations of cell division in vertex models yield geometrically irregular cells, similar to empirical observations in epithelia, even when cell mechanical properties are homogeneous. Nevertheless, existing theoretical analyses are mostly confined to the mechanics of regular hexagonal lattices.

Here, we develop an analytical description of geometrically disordered vertex models. We first quantify, in numerical simulations, geometric and mechanical cell properties in the presence of diverse sources of disorder, including various division rules or relaxation in the presence of noise. We then develop a simple mean-field description able to account for these properties. This description is expanded to address the interaction of isolated and clustered cells with mechanical properties differing from the surrounding tissue relevant in a wide range of biological contexts. This allows us to bridge the gap between theory and experiments, quantitatively predicting how variation in forces may affect geometry and topology as well as fitting mechanistic model parameters to the observed geometry of cell membranes in a tissue.

Finally, in a collaborative work with the Payre's lab (U. de Toulouse), we apply our analysis to account for the statistics of cell geometry and division dynamics in experiments performed on epidermis differentiation in the fly. We particularly focus on characterizing the mechanical properties of clustered clonal cells with distinct proliferation rates from their environment.

KEYWORDS

morphogenesis, mechanics, epithelial tissues, statistical mechanics.